



University  
of Glasgow

Paterson, Rhys Leigh (2016) *The detection and characterisation of the solar UV network*. MSc(R) thesis.

<http://theses.gla.ac.uk/7260/>

Copyright and moral rights for this thesis are retained by the author

A copy can be downloaded for personal non-commercial research or study

This thesis cannot be reproduced or quoted extensively from without first obtaining permission in writing from the Author

The content must not be changed in any way or sold commercially in any format or medium without the formal permission of the Author

When referring to this work, full bibliographic details including the author, title, awarding institution and date of the thesis must be given

# The Detection and Characterisation of the Solar UV Network

Rhys Leigh Paterson, BSc (Hons)



Submitted in fulfilment of the requirements for the  
Degree of Masters of Science (By Research)

The University of Glasgow

2015

School of Physics and Astronomy

Kelvin Building

University of Glasgow

Glasgow, G12 8QQ

Scotland, U.K.

# Abstract

High resolution images of the Sun taken at UV wavelengths show the presence of a fine network like structure across the solar disc. This UV network contributes to the total power radiated by the Sun so it is clear that a study of it is of great interest. This thesis deals with the development of an automated method to quantify the covering percentage of this network in the hopes that this could lead to greater insights into the nature of said network.

Chapter 1 serves as an introduction to the Sun and the field of solar physics with a specific focus on the UV network and the processes leading to its existence. We also discuss the general motivations for solar research as whole and the particular interest in the UV network. Finally we describe the SDO satellite, and its instruments, used to gather the data used throughout this work.

Chapter 2 discusses the intricacies of the data itself and the various calibration and preparation processes it has undergone between the raw data itself and the Level 1 data made available for research. We then describe the preparation of three images to be used to test all our developed algorithms on.

Chapter 3 deals with the presence of solar limb darkening and the possible issues caused by its presence. We develop and evaluate several methods to counter the limb darkening, before determining the final algorithm to be used before any network detection takes place.

In Chapter 4 we describe the development of several methods to detect the UV network. We then attempt to determine which of these detection algorithms is the most suitable for use on large data sets.

Chapter 5 discusses the results observed when applying our selected detection algorithm to several years worth of data. From these results we discuss the behaviour of

the UV network and its correlation with other methods of solar variability.

In Chapter 6 we discuss whether, and to what extent, we have met the original targets of this thesis work. We then go on to explore the problems that were encountered throughout our research before finally outlining future work that could be done to further and improve upon our results.

# Contents

<b>Abstract</b>	<b>2</b>
<b>List of Tables</b>	<b>7</b>
<b>List of Figures</b>	<b>9</b>
<b>Acknowledgements</b>	<b>13</b>
<b>1 Introduction</b>	<b>15</b>
1.1 Solar Research Motivation . . . . .	16
1.2 Solar Structure . . . . .	17
1.3 Solar Limb Darkening . . . . .	20
1.4 The Solar UV Network . . . . .	21
1.5 The SDO Mission . . . . .	23
1.5.1 The Atmospheric Imaging Assembly . . . . .	25
<b>2 Image Examination and Preparation</b>	<b>26</b>
2.1 SDO Processing . . . . .	26
2.1.1 Overscan Removal and Dark Image Correction . . . . .	27
2.1.2 Bad Pixels and Spikes . . . . .	28
2.1.3 Flatfielding . . . . .	29
2.2 Image Properties . . . . .	32
2.3 Creation of Test Images . . . . .	37
<b>3 Limb Darkening Correction</b>	<b>43</b>
3.1 Limb Darkening in More Detail . . . . .	44

3.2	Correcting for the Background Intensity . . . . .	45
3.2.1	Markov Chain Monte Carlo Profile . . . . .	45
3.2.2	Fast Fourier Transform Filter . . . . .	50
3.2.3	Top-hat Transform . . . . .	54
3.2.4	Comparison of Methods . . . . .	57
<b>4</b>	<b>Network Detection</b>	<b>63</b>
4.1	Brightness Based Detection . . . . .	67
4.1.1	Basic Threshold . . . . .	67
4.1.2	Concentric Thresholds . . . . .	76
4.2	Morphology Based Detection . . . . .	86
4.2.1	Morphological Dilation . . . . .	88
4.2.2	Granulometry . . . . .	95
4.3	Comparison of Methods . . . . .	98
<b>5</b>	<b>Behaviour of the Network</b>	<b>100</b>
5.1	Temporal Behaviour . . . . .	100
5.1.1	Short Scale . . . . .	100
5.1.2	Long Scale . . . . .	103
5.2	Comparison with other measures of Solar Variability . . . . .	105
5.2.1	Brightness . . . . .	105
5.2.2	F10.7 Flux . . . . .	111
5.3	Behaviour of the Quiet Sun . . . . .	113
5.3.1	Removal of Active Regions . . . . .	113
5.3.2	Behaviour of ‘Quiet’ Areas . . . . .	120
<b>6</b>	<b>Discussion and Conclusions</b>	<b>122</b>
6.1	Accomplishment of the Initial Aim . . . . .	122
6.2	Problems Encountered . . . . .	123
6.3	Future Work and Improvements . . . . .	124
	<b>Bibliography</b>	<b>126</b>



# List of Tables

3.1	The time taken for each background correction method. . . . .	57
4.1	The fraction of pixels identified as network at a basic threshold of 0.45 for the three full disc test images. . . . .	75
4.2	The thresholds tested in the concentric sections for network detection. .	78
4.3	The fraction of pixels identified as network using the final concentric thresholds on the three test images. . . . .	83
4.4	The network detected using the final morphological detection on the three test images. . . . .	93
4.5	The time taken for each UV network detection method. . . . .	99



# List of Figures

1.1	An artificially coloured image of the sun in visible light showing limb darkening. . . . .	20
1.2	The solar network at 1600 Angstroms. . . . .	22
1.3	A zoomed in view of a section of UV network at the centre of the solar disc. . . . .	23
1.4	Sample images taken by the Atmospheric Imaging Assembly on board the Solar Dynamics Observatory satellite. . . . .	24
2.1	Sample flatfields taken at 1600 Angstroms. . . . .	31
2.2	A full disc image at 1600 Angstroms. . . . .	33
2.3	A histogram of a 1600 Angstrom solar image. . . . .	34
2.4	The average image brightness from January 2011 to January 2015. . . . .	35
2.5	The exposure time of one image a day from Jan 2011 to 2015. . . . .	36
2.6	A 1600 Angstrom image of the Sun with the lower pixel value set to 0 and the upper set at decreasing values. . . . .	38
2.7	The full disc quiet Sun test image. . . . .	40
2.8	The full disc medium activity Sun test image. . . . .	41
2.9	The full disc active Sun test image. . . . .	42
3.1	The mean brightness across the centre of the solar disc, illustrating limb darkening at 1600 Angstroms. . . . .	44
3.2	The successful fit to an average solar UV intensity created using the MCMC algorithm. . . . .	47
3.3	The background created from the MCMC fit. . . . .	48
3.4	Final background correction with the MCMC profile. . . . .	49

3.5	Intensity profile created by the FFT process. . . . .	51
3.6	Initial background application with the FFT method. . . . .	52
3.7	Final background correction with the FFT method . . . . .	53
3.8	The background using a top-hat transform and various filters. . . . .	55
3.9	Final background correction with the top-hat transform method. . . . .	56
3.10	Mean intensity across the centre of the Sun after the three different backgrounds have been applied. . . . .	58
3.11	The quiet Sun test image with the morphological opening background correction. . . . .	59
3.12	The medium activity Sun test image with the morphological opening background correction. . . . .	60
3.13	The active Sun test image with the morphological opening background correction. . . . .	61
3.14	A histogram of the quiet Sun test image with the top-hat background correction applied. . . . .	62
4.1	The two small zoomed in test images for detection method evaluation. . . . .	64
4.2	The two small zoomed in test images for detection method evaluation. . . . .	66
4.3	Three small test sections for the development of detection methods. . . . .	68
4.4	Quiet test section with increasing thresholds. . . . .	69
4.5	Medium activity test section with increasing thresholds. . . . .	70
4.6	Active test section with increasing thresholds. . . . .	71
4.7	The results of using a fine tuned increasing basic threshold on the active test section. . . . .	72
4.8	Test of the basic threshold's effectiveness at the centre of the active Sun test image. . . . .	73
4.9	Test of basic threshold's effectiveness at the limb of the active Sun test image. . . . .	74
4.10	The three sections used for the concentric thresholding technique. . . . .	77
4.11	The network covering percentage plotted against the threshold at which it was detected. . . . .	77

4.12	The two test sections used for the development of the concentric threshold detection method. . . . .	78
4.13	The results of using increasing threshold values for the test section within the middle concentric ring. . . . .	79
4.14	The results of using increasing threshold values for the test section within the outer concentric ring. . . . .	80
4.15	An example of unwanted banding using the concentric section thresholds.	81
4.16	Active Sun test image with final concentric thresholds applied. . . . .	82
4.17	A test of whether the concentric thresholds create a smooth overall detection. . . . .	83
4.18	Test of concentric threshold's effectiveness at the centre of the active test image. . . . .	84
4.19	Test of concentric threshold's effectiveness at the limb of the active test image. . . . .	85
4.20	Three different structuring elements with the foreground regions shown in black and the origin as a small white circle. . . . .	87
4.21	The marker images for each of the morphological test sections. . . . .	89
4.22	A comparison between the original test image and the results of the morphological processing. . . . .	90
4.23	The results of increasing iterations of the morphological network detection on three test sections. . . . .	91
4.24	Test of morphological opening's effectiveness at the centre of the active test image. . . . .	92
4.25	Test of morphological opening's effectiveness at the limb of the active test image. . . . .	94
4.26	The two preliminary plots from the use of granulometry. . . . .	96
4.27	The resultant features at two scales from a granulometry based network detection. . . . .	97
5.1	The covering percentage of the UV network throughout December 2014.	101
5.2	The covering percentage of the UV network throughout 2014. . . . .	102

5.3	The covering percentage of the UV network from January 2011 to January 2015. . . . .	104
5.4	The covering percentage of the UV network and the average brightness of each image from January 2011 to January 2015 . . . . .	106
5.5	The covering percentage of the UV network from January 2011 to January 2015 with a correction applied. . . . .	109
5.6	The corrected covering percentage of the UV network and the average image brightness from January 2011 to January 2015. . . . .	110
5.7	The corrected covering percentage of the UV network and the F10.7 flux from January 2011 to January 2015. . . . .	112
5.8	The test image used for active region removal with two quiet areas shown in red. . . . .	114
5.9	The resultant components from using SSA on the active Sun test image.	116
5.10	The resultant images from using a series of increasing gaussian filters to detect active regions. . . . .	119
5.11	The covering percentage of the network within the two active region free areas of the Sun from January 2011 to January 2015. . . . .	121

# Acknowledgements

I would first like to thank Prof. Lyndsay Fletcher, for both offering me this Masters project and her supervision throughout it. Without her enthusiasm and guidance this year I would not be here now. I must also thank Prof. Stephen Marshall at Strathclyde University for his exceedingly helpful consultations on all things image processing and also Dr. Jaime Zabalza for his programming assistance.

My final thanks go first to my office-mate Euan Bennet for his willingness to act as a sounding board for the last year and to Katherine Wallace for her support and understanding during this Masters.

---

This thesis is my own composition except where indicated in the text.  
No part of this thesis has been submitted elsewhere for any other degree  
or qualification.

**Copyright © 2015 by Rhys L. Paterson**

October 2015

---

# Chapter 1

## Introduction

Mankind has long been fascinated with the Sun, with records of simple solar phenomena such as eclipses dating back millennia [1]. Over time these records became more detailed, and important, with the Chinese recording observations of sunspots as early as circa 300BC [2]. Interest in the sun and its phenomena has not lessened over time, though its focus has become more scientific rather than religious or cultural.

With the advent of both satellite and advanced imaging technologies current solar observations have become incredibly detailed, leading to an abundance of high resolution images of the Sun at many wavelengths available to be analysed.

The work presented in this thesis uses images from one wavelength in particular, 1600 Angstroms. These wavelengths fall in the UV part of the spectrum and when viewed at this wavelength a complex network-like structure is visible on the solar disc. This work details the development of a method to quantify what percentage of the solar disc is covered by this ‘network’. Using images from the Solar Dynamics Observatory (SDO) satellite an algorithm is created to do just this over the lifetime of the SDO mission. This algorithm depends heavily on the use of image processing, a field that has become indispensable within solar physics research. To ensure the suitability of the algorithm several are applied to a series of test images and their effectiveness analysed quantitatively and qualitatively. Once a particular algorithm is settled upon we analyse the time related behaviour of the network before discussing the implications of the analysis and then moving on to a final conclusion.

This chapter serves as an introduction to the field of solar physics and a discussion

as to the nature of the UV network itself. We then move on to the motivations for solar research and specifically this study of the UV network before finishing with a summary of the SDO mission and the equipment on board that is responsible for the capture of all the data used.

## 1.1 Solar Research Motivation

It is not difficult to justify solar research and over recent years the many motivations for this research have multiplied. By virtue of being our nearest star the Sun offers us our best, if not only, opportunity to study stars in real depth. Conditions within the Sun and its atmosphere are not replicable within a laboratory and so offer a chance to study the behaviour of plasmas at extreme physical conditions. Furthermore, it allows us to advance our knowledge of stellar theory, stellar evolution and space weather. It is the latter of these, the nature and effects of space weather, that is of particular interest to this project.

The term ‘space weather’ is essentially a catch-all term referring to time varying conditions within the Solar System, with an emphasis on the space surrounding Earth. While the effects of space weather have been observed for centuries, the Aurora Borealis being a rather dramatic example, it is only relatively recently that we have begun to properly understand it and to certain extent, even care about it [3]. It was not until the proliferation of satellite technology that many military and commercial systems could conclusively be proven to be affected by space weather, prompting an increase in research into it [4].

Within the solar system the greatest source of space weather components is of course the Sun, and in particular the solar wind. The solar wind is a stream of plasma emitted from the outer layers of the Sun that fills the heliosphere - an area of space that extends out beyond the orbit of Pluto. As such, the solar wind may be the dominant factor affecting space weather and the Earth but there is another measure that is of interest. This other variable is known simply as the Solar Irradiance, which can be divided into the total solar irradiance (TSI) and the spectral solar irradiance (SSI).

The TSI is, as it sounds, simply a measure of the total power radiated by the Sun at

all electromagnetic wavelengths. While the TSI has steadily increased over the lifetime of our nearest star it is not without fluctuations. Studies show that the TSI varies by around 0.1% with its peak aligning with that of solar activity [5]. Though fluctuations on the scale of 0.1% would often be thought of as negligible in many fields here it is thought that this could have a direct effect on space weather and, through this, the atmosphere of the Earth. In particular, there exist various wavelength-dependant contributions to the TSI (described collectively as the SSI) that affect different regions of the atmosphere. Changes to the atmosphere could not only effect our climate but have a direct effect on the behaviour of satellites passing through it. With this in mind there are many trying to quantify the various contributions to the TSI and this is where we find the main motivation of this thesis. As the Solar UV Network is a strongly varying component of the Sun's structure it will contribute to the varying TSI and SSI. We attempt to characterise its behaviour in this thesis. To fully understand the network though it is first necessary to understand the general solar structure and what leads to the network's formation.

## 1.2 Solar Structure

The Sun, though of course special to us, is not so when compared to other stars. With a luminosity of  $3.844 \times 10^{26} \text{W}$ , a radius of  $6.95 \times 10^5 \text{km}$  and a mass of  $1.989 \times 10^{30} \text{kg}$  it is very average in both energy output and size. As such it falls on the main sequence and is classified as a star of spectral type G2V. The Sun has an average distance from the Earth of  $1.496 \times 10^8 \text{km}$  and formed about 4.5 billion years ago [6].

Understanding the structure of the Sun is hugely important to understanding the myriad of physical processes taking place within it. The mass of the Sun has two main components - hydrogen, helium and a small amount of metallic elements. Hydrogen is by far the most abundant of the solar constituents making up about 74% of the Sun's mass with helium accounting for another 24%. The final 2% is made up of heavier metallic elements, it been important to note that due to the abundance of hydrogen and helium in the Universe a 'metal' is rather loosely defined in astronomical terms as any other element [7]. The Sun can be split into different layers, each having distinctly

different characteristics and hosting different physical processes.

The core is the inner most section of the Sun, extending out from the centre to about 0.2 solar radii. This volume is the source of the Sun's energy and of the photons that will eventually reach us here on Earth. The temperature and density are so high in this region (up to 15MK and 150g/cm<sup>3</sup>) that nuclear fusion can take place, converting the hydrogen within the hot, dense plasma into helium through the proton-proton chain. At the edge of the core the temperature and density fall dramatically to around 7MK and 20g/cm<sup>3</sup> respectively.

Above the core, spanning the region from 0.2R<sub>⊙</sub> to 0.7R<sub>⊙</sub>, is the 'radiative zone', so characterised as radiation is the main form of energy transfer within this region. Over this zone the density of the plasma falls by a factor of 10 and the temperature drops to about 2MK. The motion of the plasma within this region is relatively calm but, due to the density of the particles, and their interaction with photons, light takes around a million years to escape this zone.

Between the radiative and convection zones we find a small but rather important section of the Sun known as the 'Interface Layer' or 'Tacholine'. This region forms the transition between the radiative energy transfer of the region below and the convection in the region above. It is now thought that the shear caused by the differing fluid flow velocities across this layer are the source of the Sun's magnetic field [8].

As intimated above the next region of the Sun is known as the 'convective zone'. This extends from the limits of the interface layer to the 'surface' of the Sun. At the surface the plasma density has again fallen, now by up to 6 orders of magnitude and the temperature is now a much more modest 5 to 6 thousand Kelvin. These steep gradients in temperature and density across the region means that motions within this region are convective, and significantly more turbulent than in the radiative zone below. The increased motion of the plasma is thought to twist and concentrate magnetic field lines such to drive solar activity on the surface. Further, thought of rather simply, a volume of high temperature plasma at the base of the convective zone moves upwards through the increasingly cooler material. As it moves upwards it expands and cools until it reaches the surface before falling back down for the process to begin again. This rising and falling of material leads to granulation and super granulation cells on the surface

[9].

Above the convective zone we find the solar atmosphere. Much like the atmosphere here on Earth the solar atmosphere can be split into multiple parts - the photosphere, chromosphere, transition region and finally the corona. The photosphere is a little strange in that it can be classified as part of the solar atmosphere but also serves as the ‘visible surface’ of the Sun, with an almost blackbody emission at a temperature of 5800K. Below this the interior of the Sun is opaque and this region marks the beginning of the transparent solar regions. The photosphere is the most familiar solar region to many people as it is also where we observe the most well known solar features, in visible light at least. Here we see sunspots (possibly the oldest recorded solar features) and more importantly to this work, the granulation and super-granulation cells caused by convection.

Above the photosphere we find the chromosphere, spanning 2000km and heating up to 20,000K at its upper limit. Unlike the photosphere, here the emissions are not in visible light and are instead spectral emissions lines in optical and UV wavelengths. Due to this the chromosphere is slightly red in colour, being dominated by  $H\alpha$ . This is also the region in which we find the UV network which this work attempts to detect and characterise.

The transition region is not a true region in and of itself but instead marks the transition between the cooler temperatures within the chromosphere and the much hotter corona. The mechanisms responsible for this huge increase in temperature are not yet understood and this remains one of the major mysteries in modern astronomy [10].

Finally we have the upper region of the solar atmosphere, the corona. This is by far the hottest region of the solar atmosphere, reaching temperatures of up to 2MK, and the most diffuse. The corona is visible in white light during eclipses as a faint haze extending far out into space. The corona itself is also home to many solar features and its shape changes over the activity cycle of the Sun. At times of solar minimum the corona is limited to the lower latitudes and we see coronal holes at the poles of the Sun. During periods of solar maximum, which align with the highest numbers of sunspots, the coronal holes are no longer restricted to the polar latitudes and the

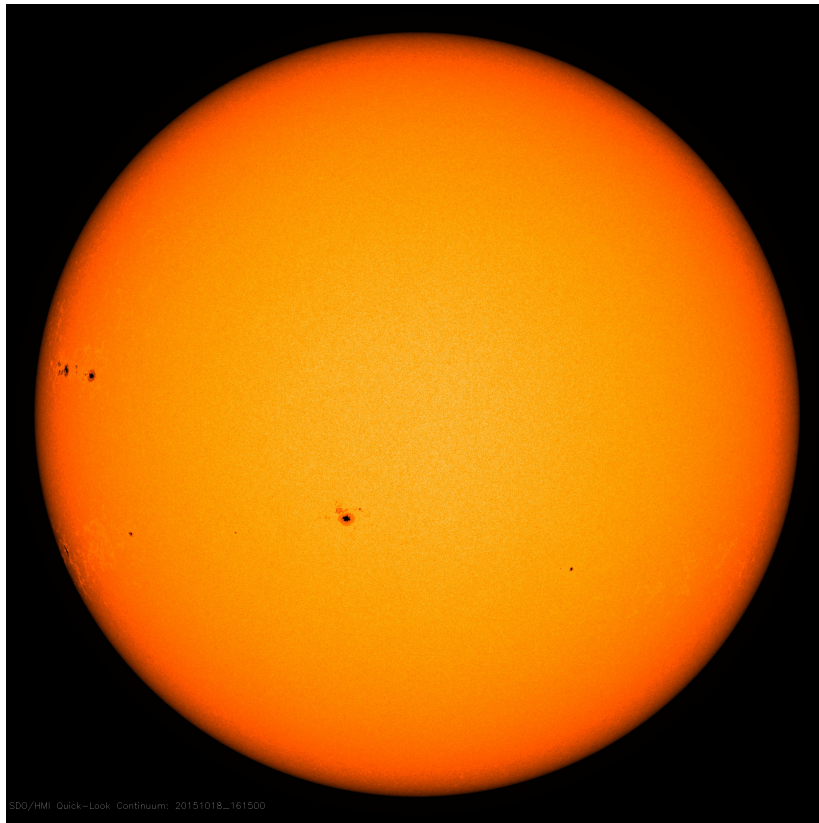


**Figure 1.1:** An artificially coloured image of the sun in visible light showing limb darkening [12].

corona in general becomes much more complex and varying in structure [11].

It is obvious from this section that Sun is an extremely variable celestial structure, one which is either responsible for, or effects, many facets of life on Earth. While there are many different regions and physical processes taking place it is those that lead to the formation, and behaviour, of the UV network that are of particular interest to this thesis.

### 1.3 Solar Limb Darkening

Limb darkening is a common optical phenomenon found in many stars and first observed in our Sun. It is, as the name may suggest, the observation that moving away from the centre and towards the limbs of the Sun the intensity starts to decline. This can very clearly be seen in Figure 1.1.

This phenomenon is well understood but needs to be discussed here as it has a direct

impact on almost all solar imaging projects, especially those that deal with full disc images.

Before an explanation into the nature of limb darkening can begin an understanding of the concept of optical depth is required.

Optical depth is an important concept in many scientific fields but within astrophysics it is related to the transparency of an object, such as a gas cloud or atmosphere. The optical depth describes the integrated absorption,  $\kappa_\nu$ , due to material of density along the line of sight [6]. A stars ‘surface’ is commonly defined as the position at which the optical depth is equal to 1.

With this definition of optical depth we can begin to understand limb darkening.

When we view the Sun we are looking through the transparent atmosphere down to the point at which the optical depth equals 1, which is where the photons we see are emitted. When we look at the centre of the solar disc we are seeing deeper into the Sun than when we look at the limb. Since below the chromosphere the temperature of the material falls as its distance from the centre of the Sun increases this means we are seeing hotter material when we look at the centre of the Sun than when we look at the limb. Hence, the limb appears darkened [6].

Obviously this can cause issues for imaging projects reliant on the brightness of the Sun and so corrections for it must often be made. These corrections though are commonly trivial as all that need be done is create a fit to the limb darkening profile, an act that can be accomplished through many techniques.

## 1.4 The Solar UV Network

The solar UV network, or photospheric network, is a fine web like structure visible on the surface of the Sun when viewed at UV wavelengths. The photospheric network is essentially the combination of photospheric magnetic flux concentrations, be they faculae around sunspots or the more diffuse network present over the quiet Sun. As such it is cospatial with the more understood chromospheric network but exists on a much finer scale [13].

As mentioned earlier the convection processes that lead to the formation of granulation

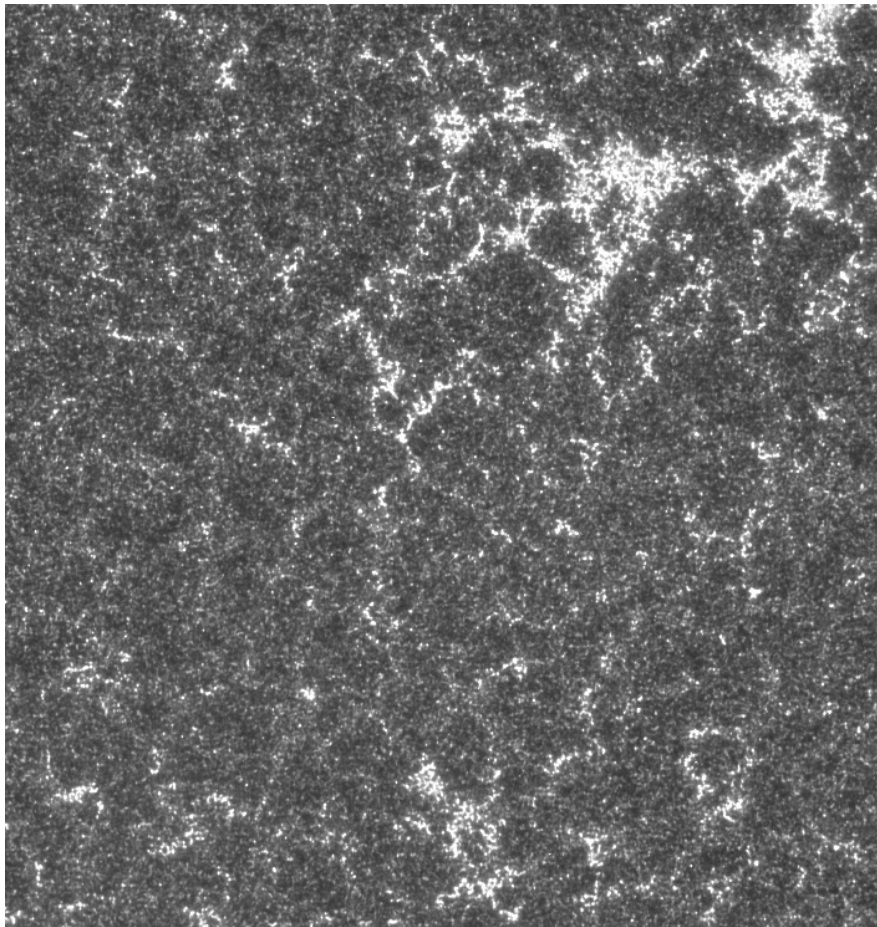


**Figure 1.2:** The solar network at 1600 Angstroms.

cells, or granules, are important to the creation and location of the network. As the hot material within the convection cell reaches the surface it cools and falls back down. The material towards the edge of the cells cools quicker however and so the granules are brighter in the centre and dim towards the edge. This convection blocks the magnetic field lines within the cells leading to a concentration of them within the boundaries of the cells. As the cells are only about 1500km in size and exist on timescales as short as 20 minutes the granular structure is extremely variable. This small granulation is organised into even larger scale patterns showing much weaker flow patterns. This larger pattern is called super-granulation and is on scales exceeding 20,000km. The brighter boundaries between the super-granulation cells are outlined by the quiet Sun UV network.

Given we find the network around sunspots too we see even more variance here in the network through the motions of these spots.

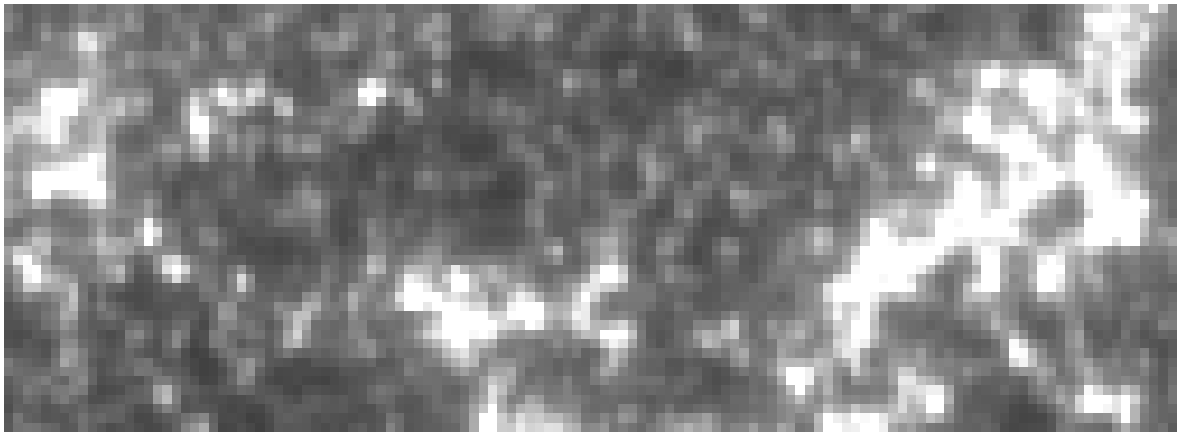


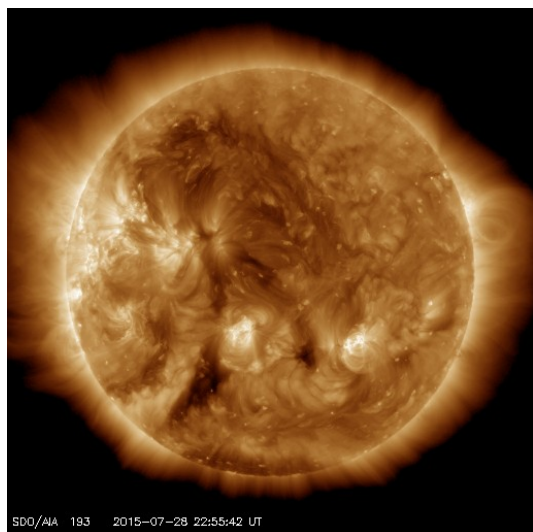
**Figure 1.3:** A zoomed in view of a section of UV network at the centre of the solar disc.

It is known that the emission from the photospheric network contributes to the TSI, especially the bright faculae areas around sunspots, but the extent to which it contributes is not well understood [14]. It is only relatively recently, with the launch of SDO, that such high resolution images have existed for the UV network allowing this project to take place.

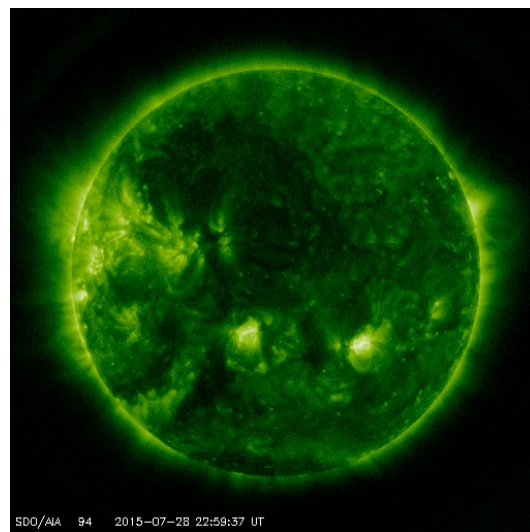
Though we know the general nature and appearance of the network it needs to be known what it appears like at these high resolutions, as that will of course form the basis of any detection method. When viewed up close (Figure 1.3) the network still maintains its web-like structure but it is obvious that defining the absolute extent of the network will be a subjective issue. The centremost regions of the network are often bright enough to saturate the data range and so are easy to differentiate from the quiet background Sun; the outer regions of the network are not however quite so easily distinguished. The brightness of the centremost pixels gradually bleeds out to the neighbouring pixels until it fades into the background Sun. Differentiating between the background Sun and outer network pixels will thus be a rather subjective task and how to incorporate it into a successful detection method will be discussed later.

## 1.5 The SDO Mission

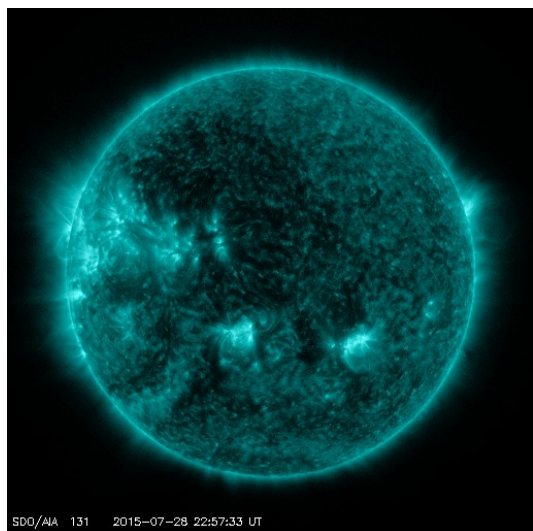
Within the last decade NASA has developed the Living With a Star program. This is a space weather based program with the goal of understanding the causes of solar



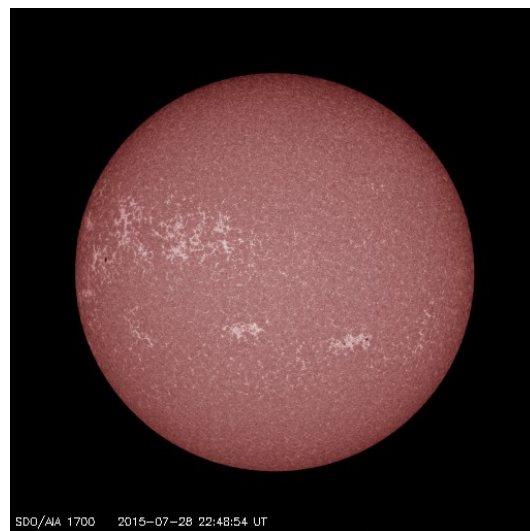
(a) The Sun at 513 Angstroms.



(b) The Sun at 94 Angstroms.



(c) The Sun at 121 Angstroms.



(d) The Sun at 1700 Angstroms.

**Figure 1.4:** Sample images taken by the Atmospheric Imaging Assembly on board the Solar Dynamics Observatory satellite.

variability and its impact on the Earth and society. With this in mind the Solar Dynamics Observatory (SDO) was the first of its satellites launched in February 2010 [15]. The SDO aims to help our understanding of solar variability by taking continuous data at many wavelengths simultaneously. The SDO Atmospheric Imaging Assembly (AIA) has a spatial resolution of  $1.2''$  ( $0.6''$  per pixel) and captures an image in each of 10 wavelengths approximately every 10 seconds [16].

This amount of high resolution data is unprecedented and is by some estimates as much as 50 times more science than any previous NASA mission.

On board the SDO there are three main scientific experiments responsible for the gathering of all this data. These are the EUV Variability Experiment, Helioseismic and Magnetic Imager and the Atmospheric Imaging Assembly. While all three of these collect incredibly detailed and useful data it is the data collected by the final of these, the Atmospheric Imaging Assembly, that is used throughout this research.

### 1.5.1 The Atmospheric Imaging Assembly

The Atmospheric Imaging Assembly is led by the Lockheed Martin Solar and Astrophysics Laboratory in California. Of the 10 wavelengths at which AIA captures data seven are extreme ultraviolet (EUV), two are ultraviolet (UV) and one is of visible light.

The AIA consists of four dual-channel telescopes, each of which with a field of view of 41 arc-minutes. Each of the EUV channels is serviced by a half-aperture of a telescope while the final half-aperture records 1600, 1700 and 4500 Angstrom measurements. These three wavelengths are recorded by cycling through a set of focal plane filters.

Each of the AIA telescopes has a 16 megapixel back-illuminated CCD. These CCDs are separated into four 2048 by 2048 pixel quadrants, all of which are read out separately and simultaneously.

# Chapter 2

## Image Examination and Preparation

When undertaking research it is usually preferable to acquire the data firsthand, this way any nuances within the equipment can be fully explored and accounted for. Of course, this is not often possible in astronomy. Instead we rely on data obtained by a variety of large telescopes and satellite imaging systems, as is the case here. To ensure the data is suitable to be worked on though and is not flawed in any way we need to understand both the acquisition process and any processing it undergoes before becoming available to us.

In this chapter we discuss the data post capture and investigate any procedures that may alter it from its raw state. Further, we then create a series of test images to be used throughout the rest of the investigation.

### 2.1 SDO Processing

The data used for this research is made available to the public in the form of Flexible Image Transport System (FITS) files. Within the field of astronomy this is the most commonly used file system as it was designed specifically for the storage of scientific data and as such has many benefits to the storage of astronomical images. Primary among these is the fact that metadata concerning the capture of the images can be stored in a header alongside the image data itself, such as the exposure time for the

image, the date of capture, the wavelength or any relevant spatial calibration information.

The data itself is then categorised based upon the level of processing it has undergone at the hands of the SDO science team. The ‘Level 0’ designation is for the raw data exactly as it is captured whereas the ‘Level 1’ data has been heavily processed. Unfortunately the raw Level 0 data is not generally made available to those outside the science team and so we instead use the already processed ‘Level 1’ data. We assume that the processing between the levels was done correctly but it is still necessary to investigate this given its importance to the data.

The processing in question is for the most part standard procedure common to all CCD-based imaging projects: dark image correction; removal of ‘overscan’ rows and columns; ‘bad’ pixel removal and spatial corrections to account for the movement of the imaged object. The movement of the imaged object here being the apparent movement of the Sun caused by the movement of the spacecraft, not the constant movement of material seen on the surface of the Sun.

As common as some of these processes are they are not trivial and so will be discussed in more detail. Further, some processes such as the removal of ‘spikes’ or the production of flatfields are either unique to astronomical imaging or more complicated than their earth based counterparts.

### 2.1.1 Overscan Removal and Dark Image Correction

The first step performed during the processing between Level 0 and Level 1 is the removal of any overscan rows and columns.

For each pixel to collect charge a small potential difference must be applied to the CCD and the simple act of doing this causes the chips to read a value - this is known as the bias level. The use of overscan is how this bias level is removed. The region of overscan rows and columns are not real pixels that form part of the CCD but are instead ‘pseudo-pixels’ created by sending additional clock cycles to the CCD output electronics [17]. The mean value within this overscan region is then determined and removed from all other pixels and the overscan region then ‘trimmed’ from the image. This technique is not normally necessary if flatfield and dark image correction is also

used (which it is here) but is used by the SDO team for engineering purposes.

After the removal of any overscan rows and columns a dark image correction is applied to account for CCD read noise, dark current and the digital offset. The dark current for the CCD onboard the AIA should be negligible as its temperature is generally less than  $-65^{\circ}\text{C}$  [16]. These factors combined however can have a similar affect to the bias level detailed above, causing the pixels to read a value that does not correspond to the imaged object. Here the correction is a little simpler though and all that need be done is capture an image with the shutter closed and then subtract this from each subsequent image captured.

### 2.1.2 Bad Pixels and Spikes

Bad pixels and spikes are issues at extremely small scales, affecting small groups of pixels and even lone individual ones. While spikes are more unique to astronomical imaging bad pixels are an issue found in all CCD imaging. These bad pixels are simply pixels that do not behave in the same way as the average pixel in the CCD does. These pixels make up a tiny amount of the actual CCD, no more than 0.1%. An algorithm is used to identify these and then to correct them. They are ‘corrected’ by simply replacing their value in each image with one that is an interpolation of the neighbouring pixels.

In images taken by space based systems it is also common to find many spikes in the image. That is, extremely bright points only a few pixels or less in size that are not bad pixels or a legitimate feature of the imaged object. These spikes are in fact evidence of cosmic rays interacting with the CCD. Cosmic rays are a frequent problem that must be accounted for in all equipment in orbit but obviously have a very noticeable effect on imaging systems.

The word ray is a historical misnomer in this regard as cosmic rays are actually high energy particles rather than electromagnetic radiation. While their origins are still somewhat mysterious it is known that they originate from outwith the solar system and are generally produced by exotic bodies such as black holes or supernovae. The majority of cosmic rays are high energy protons or atomic nuclei. When they strike a CCD they can deposit this energy directly into the CCD itself or, through interactions

with the structure of the CCD, give rise to photons which are then detected by the CCD [16].

While these spikes are extremely small they are generally very easily identified as they are not only significantly brighter than the surrounding pixels but they also only exist for one frame.

The SDO team use a well documented algorithm, adopted from the one used as part of the Transition Region and Coronal Explorer (TRACE) mission, to remove cosmic ray spikes from all images before publishing them. The algorithm detects these spikes by comparing each pixel with that of those surrounding it and if it is not statistically consistent with what one would expect from the point spread function of the imaging equipment then it is replaced by the mean pixel value of its neighbours. There is always the issue that this correction method could introduce undesirable artefacts when the features of interest to the project have similar properties to the spikes (such as the small, bright nature of compact flares) but here we assume that the network that is the focus of this work is large enough compared to such spikes as to be unaffected by their removal process.

### 2.1.3 Flatfielding

The production of, and the correction for, flatfields is a technique common to all scientific imaging projects. It is possible to find artefacts within an image that come from inconsistencies or deficiencies intrinsic to the detector itself. It is these systematic issues that flatfields aim to fix. The CCD in the AIA equipment, while cutting edge technology, is prone to several of these effects. There can be slight sensitivity differences between the pixels, vignetting and even shadows cast by the protective mesh on the focal plane of the detector [18]. Obtaining flatfields for this CCD though is not a trivial task.

To take a flatfield on Earth one would simply expose the detector to something of uniform intensity (the sky above or a sheet of white paper). Any major differences in the intensity observed in such an image thus come from differences in the pixels themselves or unavoidable shadows caused by the equipment etc. and can then be corrected for. It is not quite as easy as that in space - there is nothing in such a situation to expose

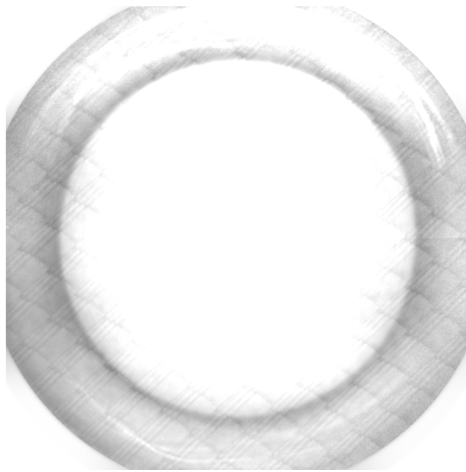
the detector to that is of uniform intensity and so a different approach must be taken. Some information relevant to the flatfielding process can be gained from the CCD before launch but the rest must be done in orbit.

The flatfields are created through the oft used in astronomy Kuhn, Lin and Loran algorithm [19]. This algorithm takes 14 out of focus images taken at different offsets and combines them into one flatfield. The range of motion of the secondary mirror however is limited by the PZT motions and for the larger offsets needed the pointing of the spacecraft itself must be adjusted. This of course is not a minor operation and so flatfields are taken at three month intervals [18]. Figure 2.1 shows four of the flatfields taken throughout the mission so far.

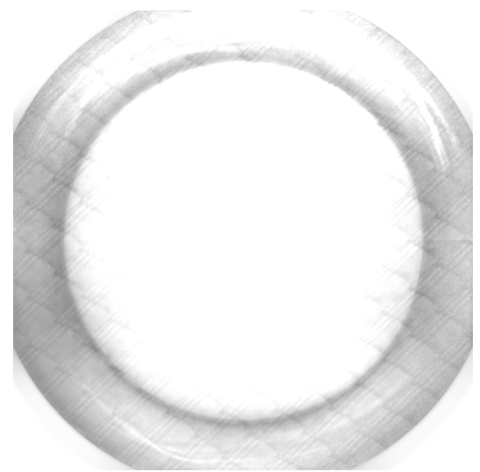
We can see in Figure 2.1 that the flatfields darken slightly over time, meaning that the CCD has degraded and become less sensitive as one would expect. Along with this darkening there are clear patterns present on the flatfields. Heavy vignetting can be seen around the edges and a regular grid like structure is visible. This most likely is the shadow of the protective mesh that covers the CCD.

Without then using this flatfield to correct the data received the values from each pixel would similarly decrease over time, and the patterns observed would also be present. This obviously needs to be accounted for so that captured images truly represent the imaged object and are free of artificial artefacts. The correction process for this is rather simple, each image need only be divided by the relevant flatfield and any systematic issues in the image are removed.

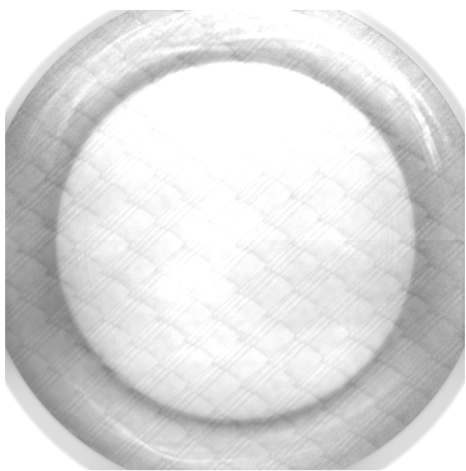
The flatfields at this wavelength were taken at regular three month intervals *apart* from the first eighteen month period from the beginning of the mission up until January 2012. This lack of flatfielding at the start of mission may cause problems later and is discussed further in Section 2.2.0.2. Such a lack of flatfielding is not ideal but is perhaps easily explained by the complexity of the flatfield acquisition procedure.



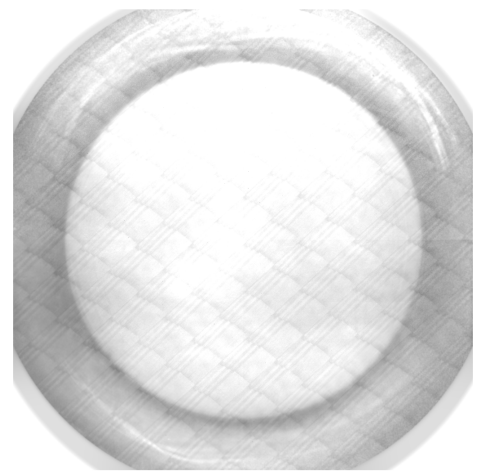
(a) Flatfield dated 01/01/2012.



(b) Flatfield dated 15/02/2013.



(c) Flatfield dated 01/03/2014.



(d) Flatfield dated 15/12/2014.

**Figure 2.1:** Sample flatfields taken at 1600 Angstroms.

## 2.2 Image Properties

We now know as much as we can about the acquisition of the data and the preparatory processes it has undergone. Now however we must examine the data in a little more detail before we begin to work with it to ensure there are no artefacts or flaws that will hinder our investigation.

Figure 2.2 shows one of the full disc images used throughout this investigation. The first obvious *flaw* with the image is that it is rather dark, now this is not an issue for detection methods but will make judgements of a detection methods effectiveness more difficult later on. This will be dealt with later in this chapter.

Before doing this however we conduct some simple tests on the images.

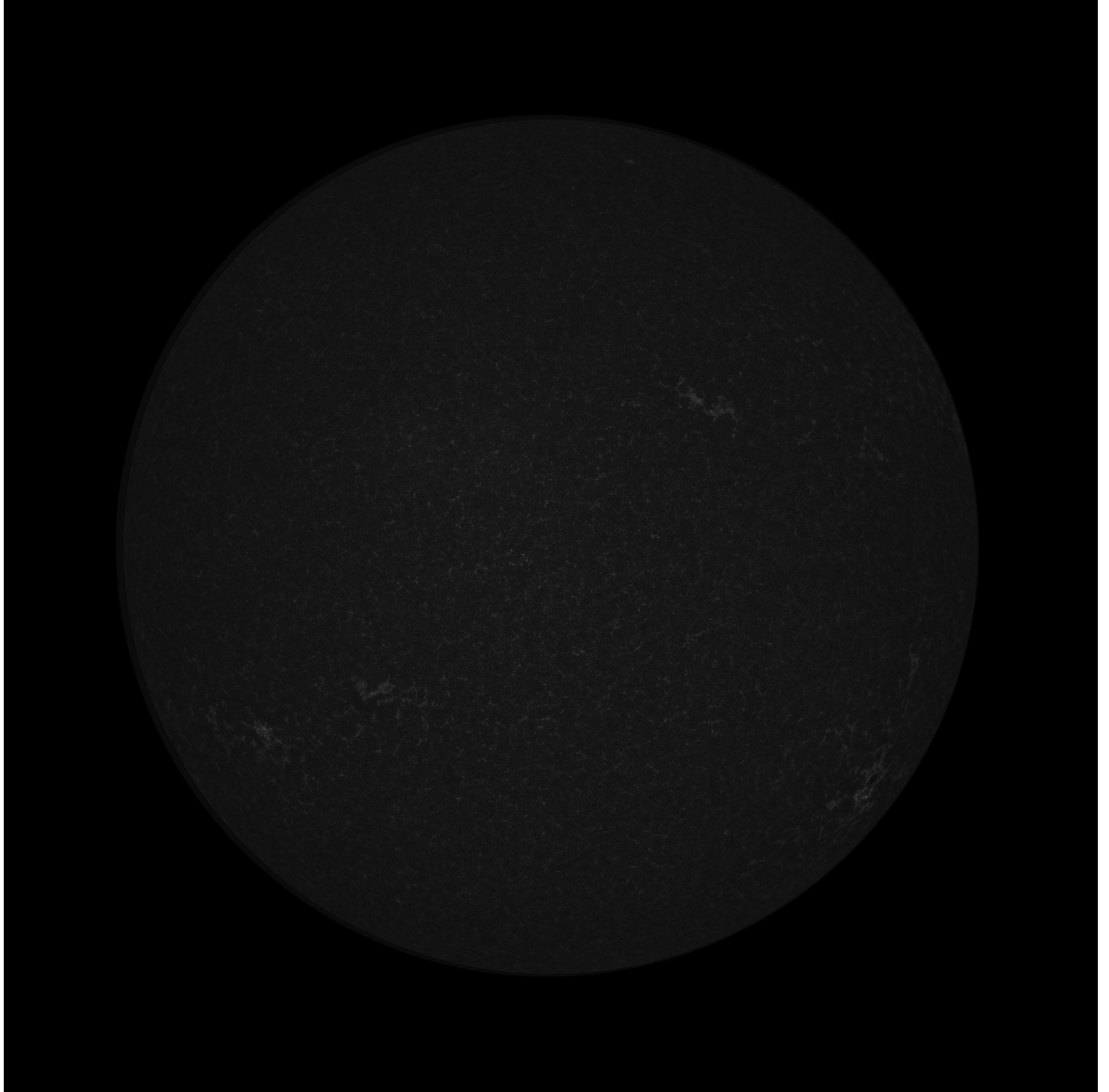


**Figure 2.2:** A full disc image at 1600 Angstroms.

### 2.2.0.1 Histogram

As is standard for many imaging projects we produced a histogram of the data counts in the image seen in Figure 2.2. A histogram of an image plots the number of pixels for each intensity value, with the intensity or pixel value along the x axis and the number of pixels with that value on the y axis. For the solar images used here we would expect to see the majority of data points on the left side of the plot indicating darker pixels with a minority on the right for the brighter active regions and network. Figure

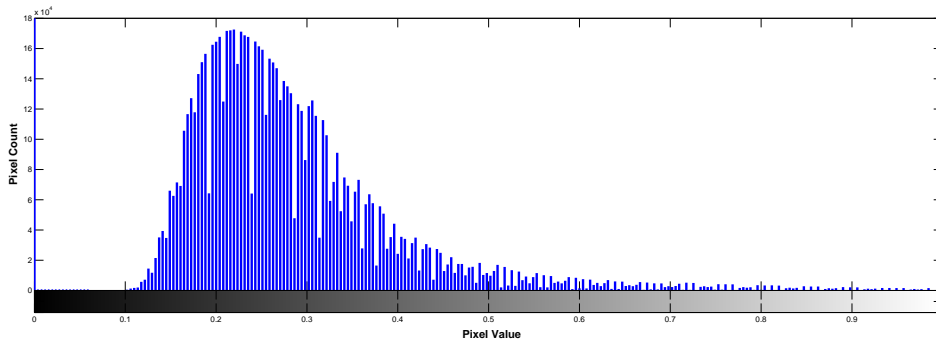


**Figure 2.3:** A histogram of a 1600 Angstrom solar image.

2.3 shows a histogram much as was expected for these images. It has a distribution centred around the darker pixels with a large spike on the 0 intensity value arising from the background area around the Sun. What however is not as expected is the ‘spiky’ outliers every second or third intensity value. There is nothing inherent in the solar features imaged to create this so it follows that this must be an artefact created through either the data acquisition process or the post processing the data undergoes. After contacting the SDO team they suggested that the odd crenellation-like pattern is more than likely a result of the rather heavy compression that images of this wavelength undergo. The pattern appears to repeat every 4 DN values with the majority of the values with a range of 4 going into one bin. Therefore the photometry is good to 4 parts in 100. Such a small corruption of the data should not have an adverse affect on any of the work we attempt throughout this investigation.

Aside from the pattern discussed above the distribution is fairly smooth. There is no distinguishing feature at the brighter end of the histogram that could be easily used

as a threshold to detect the network.

### 2.2.0.2 Brightness

As another test of the data an initial investigation into the brightness of the images was undertaken. We already know that individual images are rather dark but we don't yet know how the brightness of the images varies over the duration of the mission. It would be expected that the brightness would not vary largely over this duration but if it did so it would suggest the presence of flaws that would need to be dealt with. Calculating the mean brightness of one image a day for the period of data examined should serve this purpose (Figure 2.4).

It is abundantly clear from Figure 2.4 that for a large amount of the 4 year period examined the brightness is relatively consistent. However, there is a clear and significant drop in the brightness at the start of 2012. Obviously this needs to be addressed, or at least explained.

If we compare the date at which the large brightness drop occurs in Figure 2.4 with the dates of the flatfields we find a correlation. The taking of the first flatfield coincides exactly with this brightness drop. It was suspected earlier that the lack of flatfielding here would have implications and Figure 2.4 confirms this.

Later in this work when we come to the development of the network detection methods

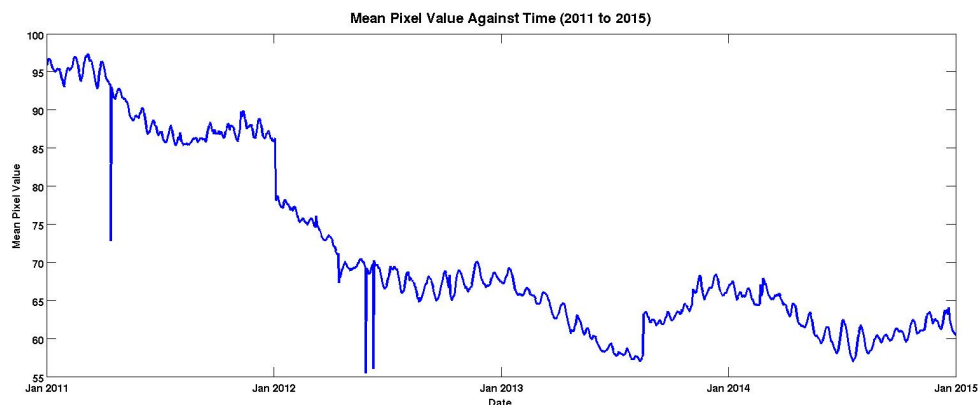


**Figure 2.4:** The average image brightness from January 2011 to January 2015.

this drop in brightness is likely to cause problems.

### 2.2.0.3 Exposure Time

One aspect of the data acquisition not corrected for in the Level 1 data is the exposure time of each image. We thus investigated any possible effects of the variations in exposure time over the course of the mission. The exposure time was investigated on two time scales. We looked at every image taken within a given day (27th January 2013) and one image a day from January 2011 to January 2015.

Our investigation found that the exposure time does indeed vary, on both these scales. This variation however is on the order of microseconds and is unlikely to have a noticeable or relevant affect on the data. The variance of the exposure time over the period spanning January 2011 to January 2015 can be seen in Figure 2.5. Further, when the

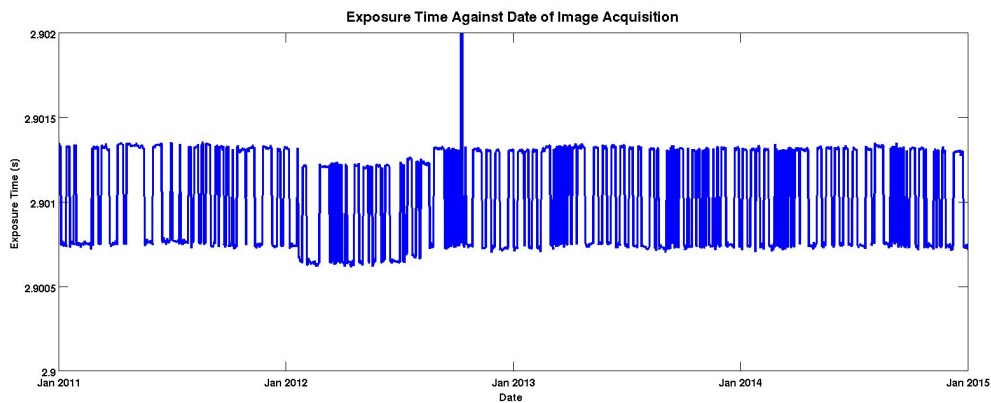


**Figure 2.5:** The exposure time of one image a day from Jan 2011 to 2015.

exposure time over the four year period is compared with the mean brightness over this same period the variations in exposure time do not correlate with those in brightness. This confirms that the lack of calibration for exposure time has no effect on the data, at least not at observable scales, and so the exposure time can be justifiably ignored.

## 2.3 Creation of Test Images

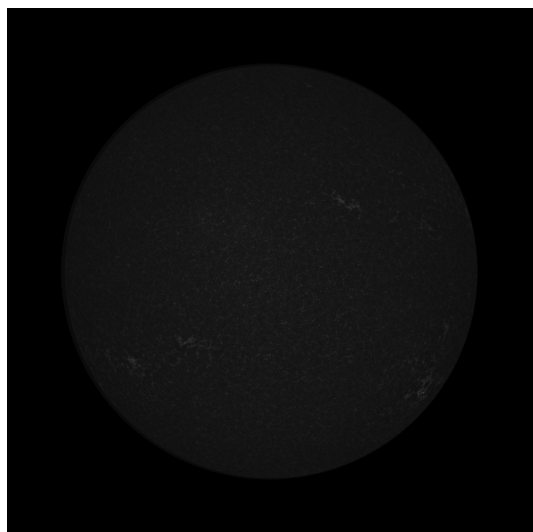
Before a detection method can be tested on a full data set it is much more efficient to test it on a small series of test images first, especially as the detection methods used later can take in excess of 24 hours per data set. To this end a set of test images were carefully chosen.

While all the calibrations and alterations done to the images before they are shared with the public are now understood the images still need a little refining before they are suitable for this project.

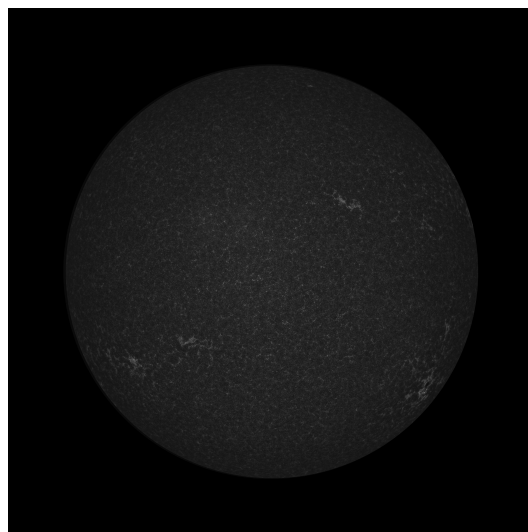
The first such task is to make the images a little clearer and easier to view. If the images are looked at from a purely visual angle, ignoring data values and such, they appear to be rather dark, as seen earlier in Figure 2.2. This is a result of the large data range for each pixel, the pixel values typically falling anywhere between -10 and 8000, and the imbalance of their distribution within this range. Throughout the data series it was not uncommon for less than 0.005% of the pixels in an image to have a value above 2000, a fact that heavily skews the apparent brightness of the images. This is not much of a hindrance for detection algorithms but given that at some level we need to physically look at the images to evaluate the effectiveness of a method it then becomes a problem.

Since such a small percentage of the pixels lie at the upper end of the data range the range can be reduced to improve the clarity of the image without compromising the detail. The technique to do this is extremely simple. Any pixel below a certain value is changed to a higher one and any above a certain threshold lowered. This must be done carefully though to ensure that no important information is lost. To this end several changes to the data range were tried to find the ideal compromise between an improved image and a loss of detail.

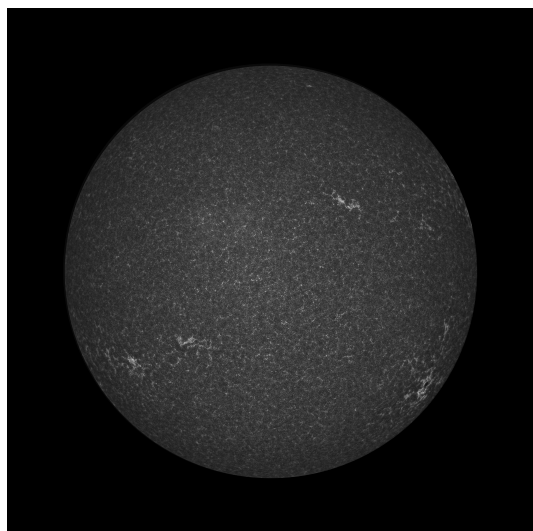
Figure 2.6 shows that lowering the data range makes the image definitively clearer but when reduced too much a significant amount of important information is lost. Through these tests it was found that to both preserve all the relevant information within the data and make the image more suitable for viewing the ideal data range was from pixel values of 0 to 700. This range allows the network to clearly stand out but no detail is lost in the quiet sun areas. This can be seen in Figures 2.7 through 2.9.



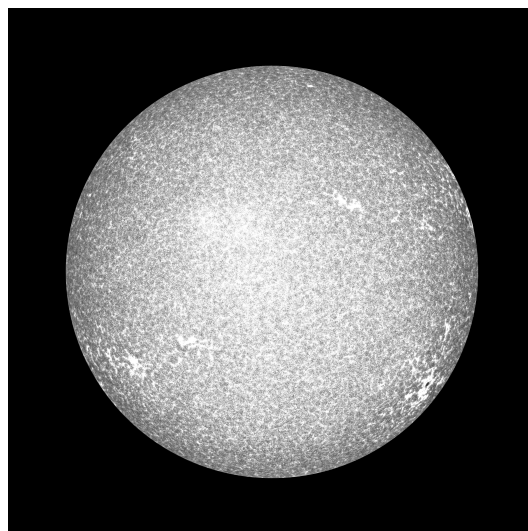
(a) Upper pixel unchanged from original.



(b) Upper pixel value of 2000.



(c) Upper pixel value of 1000.



(d) Upper pixel value of 250.

**Figure 2.6:** A 1600 Angstrom image of the Sun with the lower pixel value set to 0 and the upper set at decreasing values.

With this step finished all changes to the raw data were complete and a series of test images were ready to be chosen. To ensure that all subsequent image processing and analysis would be successful on all the images we need to investigate three test images were carefully chosen - one representing the quiet sun; one a busy, more active sun and one between the two. These images can be seen in Figures 2.7, 2.8 and 2.9 with the previously agreed upon reduction of the data range applied.

Finally it should be noted that all these processes detailed were applied to every image subsequently analysed throughout this research.

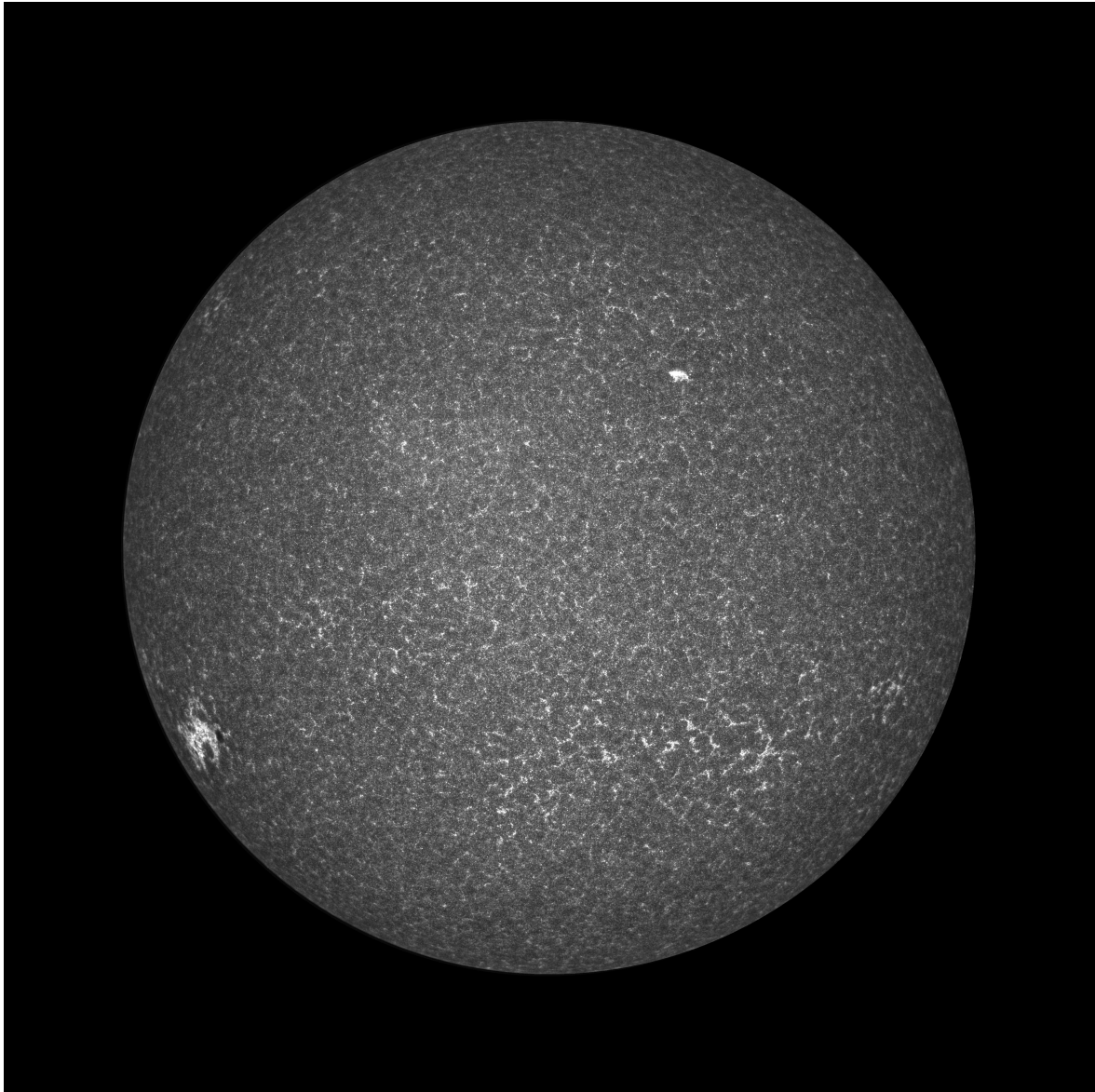


**Figure 2.7:** The full disc quiet Sun test image.

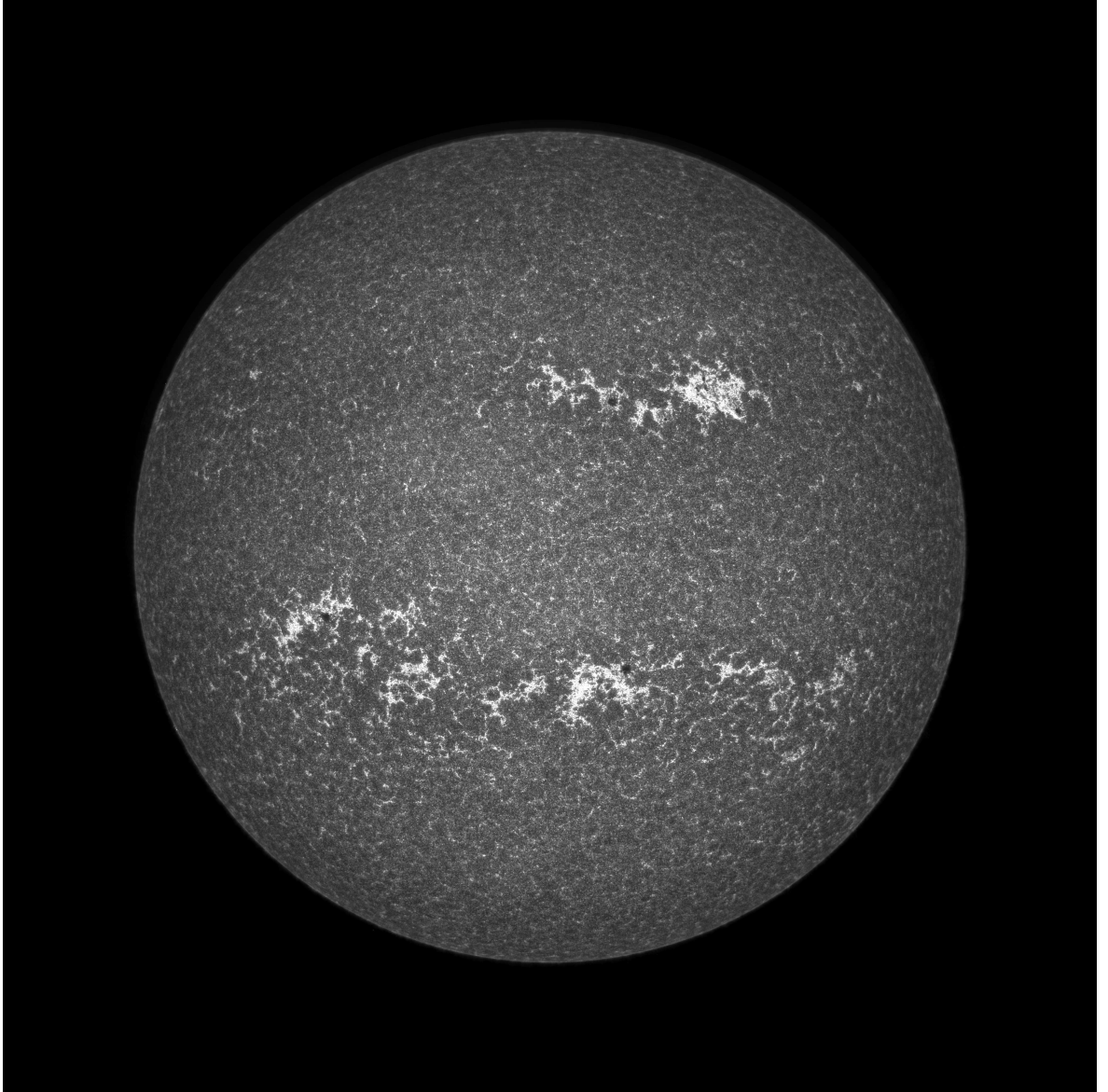


**Figure 2.8:** The full disc medium activity Sun test image.

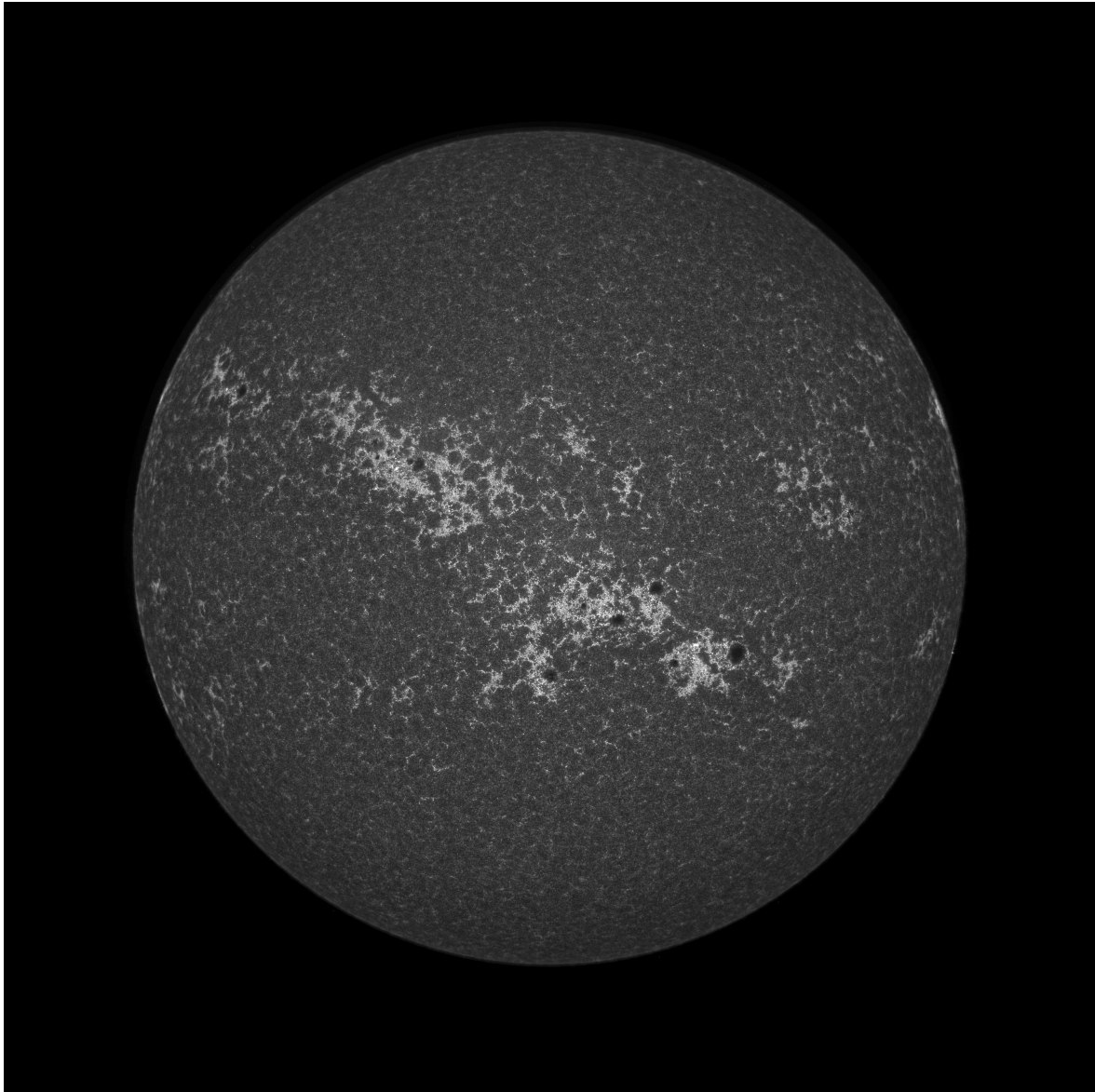


**Figure 2.9:** The full disc active Sun test image.

# Chapter 3

## Limb Darkening Correction

Earlier in this thesis the phenomenon encountered in stellar physics known as ‘limb darkening’ was very briefly discussed. There it was mentioned that limb darkening can cause problems in work that requires analysis of the Sun at visible wavelengths but it is also true that its effects are not negligible here at ultraviolet wavelengths.

Given that the limb darkening causes the brightness to diminish approaching the edge of the solar disc any detection method based solely upon the brightness of the network would need to account for this. That is, the reduction in brightness towards the limb means that a later detection method based on pixel brightness would need to account for this. Further, when viewing the images as they are in Figures 2.7, 2.8 and 2.9 the limb darkening makes it more difficult to view and detect the network at the limb.

Due to this it was decided that some form of correction should be applied to the ‘background intensity’ of each image before detection of the network was attempted. It was hoped that the background could be corrected in such a way as to reduce the large-scale variations in brightness across the disc and also give us an opportunity to investigate the limb darkening at a wavelength where it had not previously been much examined.

In this chapter we explore the limb darkening at ultraviolet wavelengths a little more thoroughly. We then describe the various methods used to correct the intensity profile of the images, after which the merits of each method are discussed and through a series of comparisons and evaluations the most appropriate process to apply to all future images is decided upon.

### 3.1 Limb Darkening in More Detail

Knowing that the limb darkening will effect all the work we try to do in this thesis it is necessary for us to examine it in more detail. Previously we had discussed the physics behind limb darkening but now we look at it more *specifically*, that is we examine the nature of limb darkening at 1600 Angstroms in particular.

In our earlier discussion of the general concept of limb darkening we plotted the intensity values of a single line across the centre of the Sun, here instead we take a larger section of the solar disc to examine the limb darkening in a little more detail. A section 100 pixels in height was taken, again across the centre of the Sun, and can be seen in Figure 3.1.

The mean value of each column in this section was then calculated and plotted against the position of said column, also in (Figure 3.1). The shape of the plot matches that

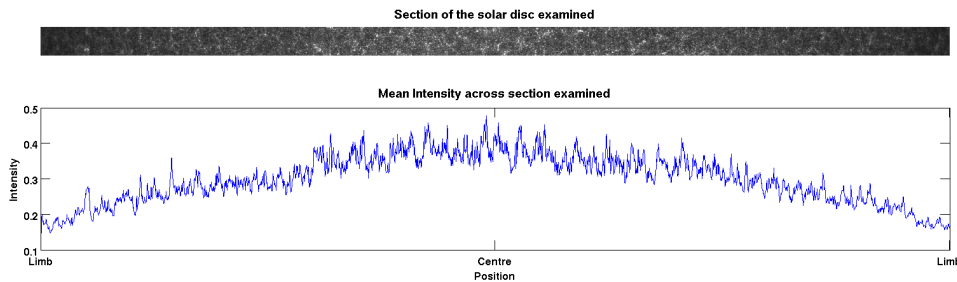


**Figure 3.1:** The mean brightness across the centre of the solar disc, illustrating limb darkening at 1600 Angstroms.

which was expected and the frequent small fluctuations seen likely originate from the presence of active regions and the network.

## 3.2 Correcting for the Background Intensity

It is clear that detection methods relying on pixel brightness need to account for limb darkening. The intended approach to account for the limb darkening is to create a full disc profile that reproduces the baseline intensity of the solar disc and then to divide the original image by this. This is much the same process used when flat fields are applied to images and should help to reduce the intensity variations. However, since the profiles we are dividing by will have lower values towards the limb, when dividing by this the fluctuations of the network at the limb compared to the background material will be amplified. This makes them more visible, but the noise that this may create at the limb is a compromise that must be made.

Considering the importance of this background correction we must be sure that it is done reliably, careful that minimal relevant information is lost in the process, but it must also be done relatively quickly. It would be preferable of course that a process be judged only on its effectiveness and not how long it takes but given that there is a finite time in which to complete this work and several thousand images will be analysed then it is an unfortunate fact that the length of each process is a considerable factor in weighing its suitability.

With that in mind several methods were tried, all of which are described below. It should also be noted that each method was tested on the quiet Sun test image seen in Figure 2.7

### 3.2.1 Markov Chain Monte Carlo Profile

The first method tried to create an intensity profile was the most mathematically intricate of all used as it was based on a statistical technique, the Markov Chain Monte Carlo method. Starting with such a method was not a dismissal of simpler, and perhaps more obvious, techniques but more an acknowledgement of its previous successes. A similar method was demonstrated successfully in 1999 by Denker and Johannesson et al. [20] and has been used many times since to remove the effects of limb darkening [21].

As such, it was of course thought that this method would be not only suitable, but

exceedingly effective.

Markov Chain Monte Carlo (MCMC) methods are a series of algorithms used in statistics to sample from a probability distribution. A large subclass of these algorithms are ‘random walk’ Monte Carlo methods and can be used to approximate a multi-dimensional integral, such as the parameters of a polynomial line profile to fit to the limb darkening. The particular MCMC method used here was the Metropolis-Hastings algorithm, a technique that works by generating a selection of sample variables which are then changed iteratively based on a set of conditions [22].

Given the shape we see for the limb darkening present (Figure 3.1) it should be possible to fit a polynomial to this that approximates the correct shape. It was decided that an equation of the form  $y = a + b \cos(x)$  would be sufficient, where  $x$  is the distance the point lies from the centre with the centre at 0 and the extreme limb at 1. The starting variables were set at values of 0.05 and 0.4 for  $a$  and  $b$  respectively.

These starting variables are then changed by a random value between -0.005 and 0.005 before being tested. If the new proposed variables pass this test they are kept and used as the starting variables for another iteration of the process, and if not then the current variables are used. The test used to decide whether the variables will be kept or discarded is known as a likelihood function,  $l$ . This likelihood function (Eq. 3.1) is calculated and if the result is greater than 1 then the variables are kept, otherwise the variables are discarded. It should be noted that  $\chi_{proposed}$  and  $\chi_{current}$  represent the chi squared test values of using the proposed and current  $a$  and  $b$  values in the  $y = a + b \cos(x)$  equation.

$$l = e^{-\chi_{proposed} + \chi_{current}} \quad (3.1)$$

After many iterations of this process we begin to home in on the variables that provide the best fit to the data [23]. After doing so a successful fit is created (Figure 3.2) with the equation  $y = -0.045 + 0.403 \cos(x)$ .

Of course this is simply a line profile and from this a full disc background is needed. Assuming that the limb darkening is radially symmetric then this profile can be revolved about its centre to create such a disc. This was accomplished by creating a matrix the same size as the original image in which the value of each element was equal to its distance from the centre of the matrix. Thus when this is multiplied by the equation for

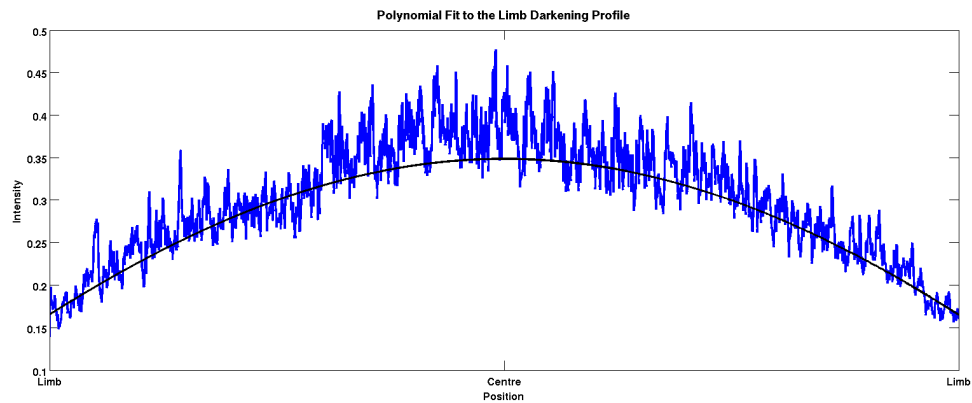


**Figure 3.2:** The successful fit to an average solar UV intensity created using the MCMC algorithm.

the fit to the limb darkening a good estimation to the background should be created. Figure 3.3 shows that this method did indeed successfully create a background and when the original image is divided by this background (shown in Figure 3.4 the large-scale intensity variations are all but removed and the image appears to be much more evenly bright (Figure 3.10).

What was not immediately apparent upon looking at Figure 3.4 (or the original images), but became obvious when the background shown in Figure 3.3 was subtracted from the original rather than divided into it was that the upper left area of the solar image appears subtly darker than the rest. Upon further examination of the other images to be analysed this feature was found in all of them. There is no solar reason that this should be the case and so it must be an issue with either the imaging equipment or the post processing. Knowing this issue is present an attempt should be made to counter it during this process and unfortunately a radially symmetric background cannot accomplish that. Therefore from this point on all the methods used to create a background will have to account for non-symmetric local variations.

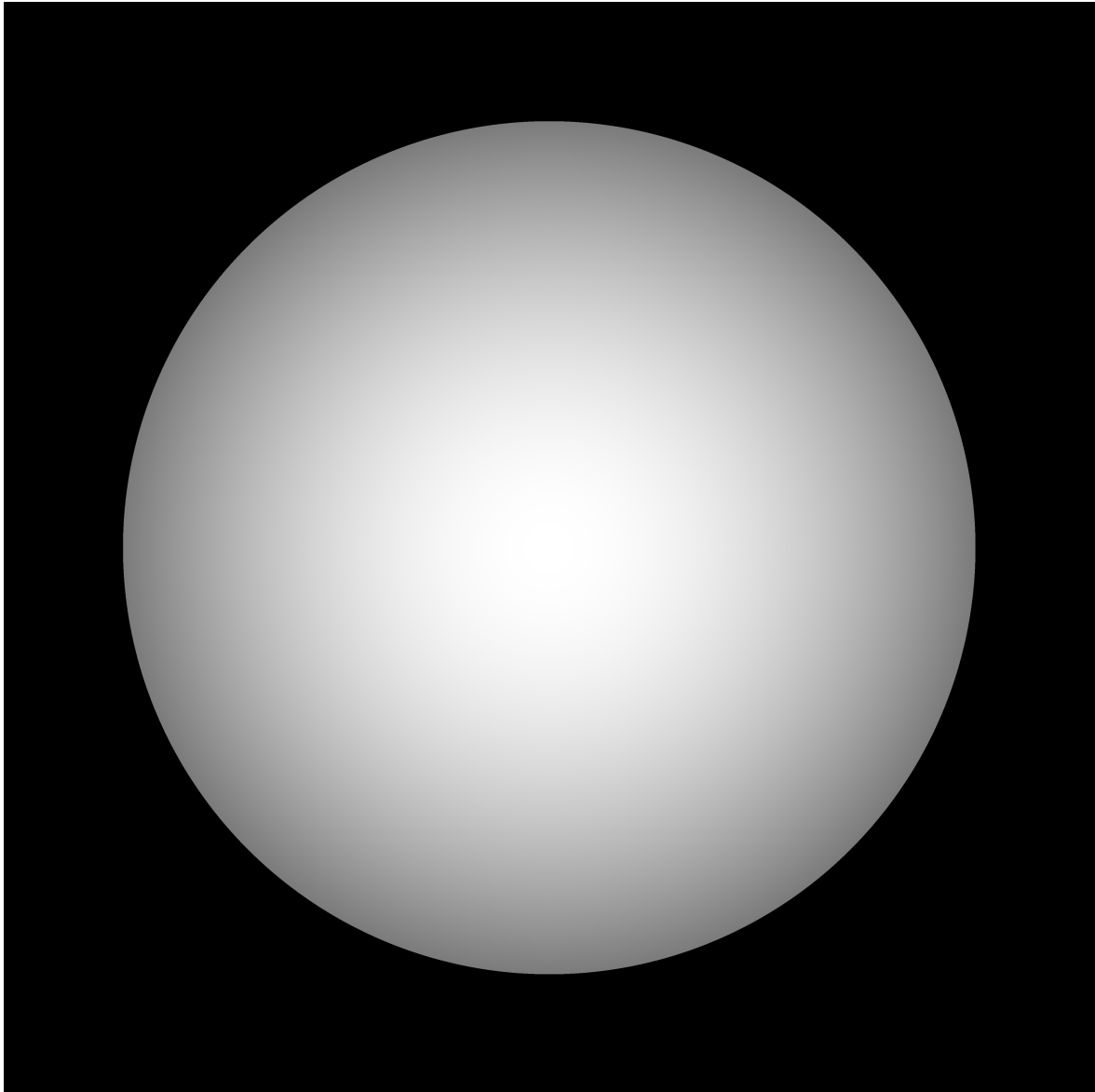


**Figure 3.3:** The background created from the MCMC fit.

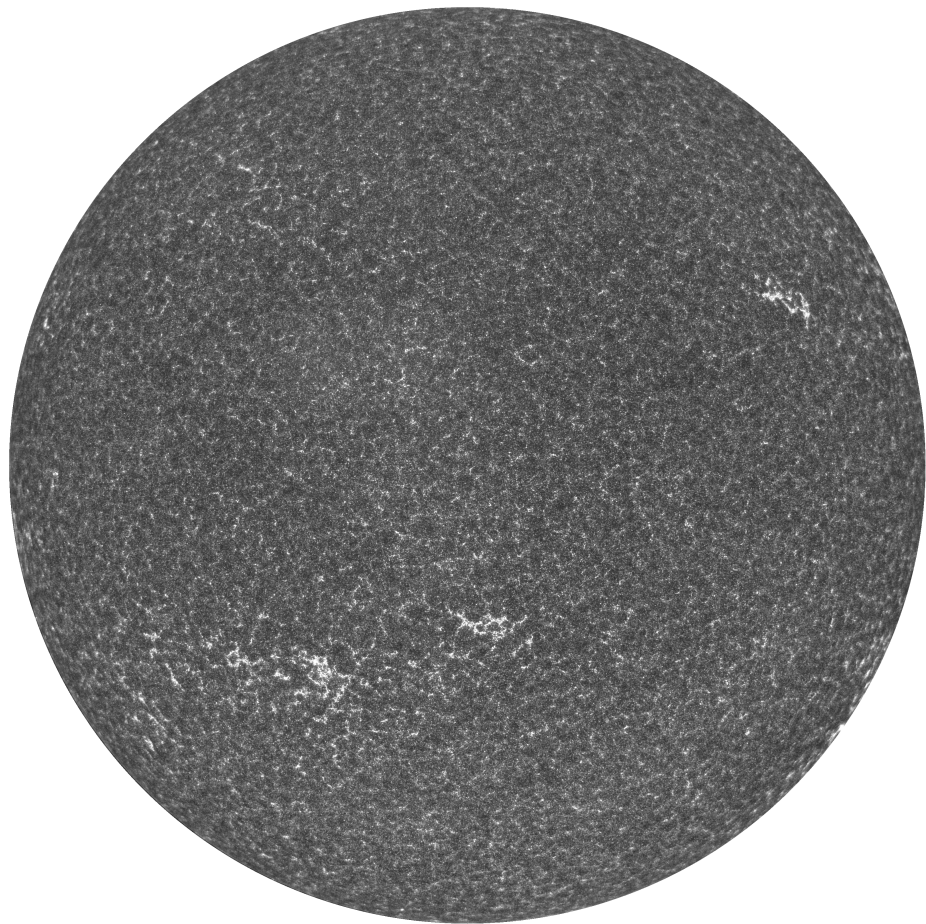


**Figure 3.4:** Final background correction with the MCMC profile.

### 3.2.2 Fast Fourier Transform Filter

Fast Fourier transforms (FFTs) are one of the simplest and most ubiquitous image processing techniques, having become almost universal throughout image processing [24], and so the use of one was the next logical step. Also, as the primary issue with the MCMC method outlined above was that it was unable to account for local variations then the fact that a Fourier transform would be able to do so is another reason to consider it as a suitable candidate. The main boon however of such a method is that the majority of the process takes place within the frequency domain. While the conversion between spatial and frequency domains (and back) takes time, the processes undertaken in the frequency domain are generally quicker than their counterparts in the spatial domain. The general procedure when using a Fourier transform is to convert the image first to the frequency domain, undertake whatever processing is needed and then reconstruct the original image from this processed frequency domain image.

To complete the first step in the process and convert the image to its frequency (or Fourier) counterpart the image must be Fourier transformed. This is calculated in MATLAB as first an FFT in one dimension followed by an FFT in the other. The formula for the 2D FFT of an image of size  $N \times N$  is given in Equation 3.2 while Equation 3.3 shows the inverse FFT used to convert back to the spatial domain.

$$F(x, y) = \sum_{a=0}^{N-1} \sum_{b=0}^{N-1} f(a, b) e^{-i2\pi(\frac{xa}{N} + \frac{yb}{N})} \quad (3.2)$$

$$f(a, b) = \frac{1}{N^2} \sum_{x=0}^{N-1} \sum_{y=0}^{N-1} F(x, y) e^{i2\pi(\frac{xa}{N} + yb/N)} \quad (3.3)$$

Here  $f(a, b)$  is the image in its original spatial domain and  $F(x, y)$  the corresponding points in Fourier space.

Given that the aim here is to create a background that gives a general idea of the image intensity we want to blur the original image. This is easily achieved within the Fourier domain by multiplying the transformed image by a smoothing filter. To ensure a smooth blurring without introducing any edge effects into the image a gaussian filter is used [25]. Once these two Fourier images are multiplied the resultant image is converted back to the spatial domain using the inverse fourier transform (Equation



**Figure 3.5:** Intensity profile created by the FFT process.

3.3). Figure 3.5 shows the results of doing this. As was done earlier, the original image can then be divided by this background to even out the brightness across the disc. An issue with this is immediately evident however; the background created has been shifted spatially compared to the original image and the output image which should show an evenly bright solar disc is clearly flawed (Figure 3.6).

This spatial offset is a peculiarity of the MATLAB implementation. It is directly related to the scale of the blurring filter used and so is easily corrected. Since we know what size blurring filter is used we need only shift the blurred image back by the

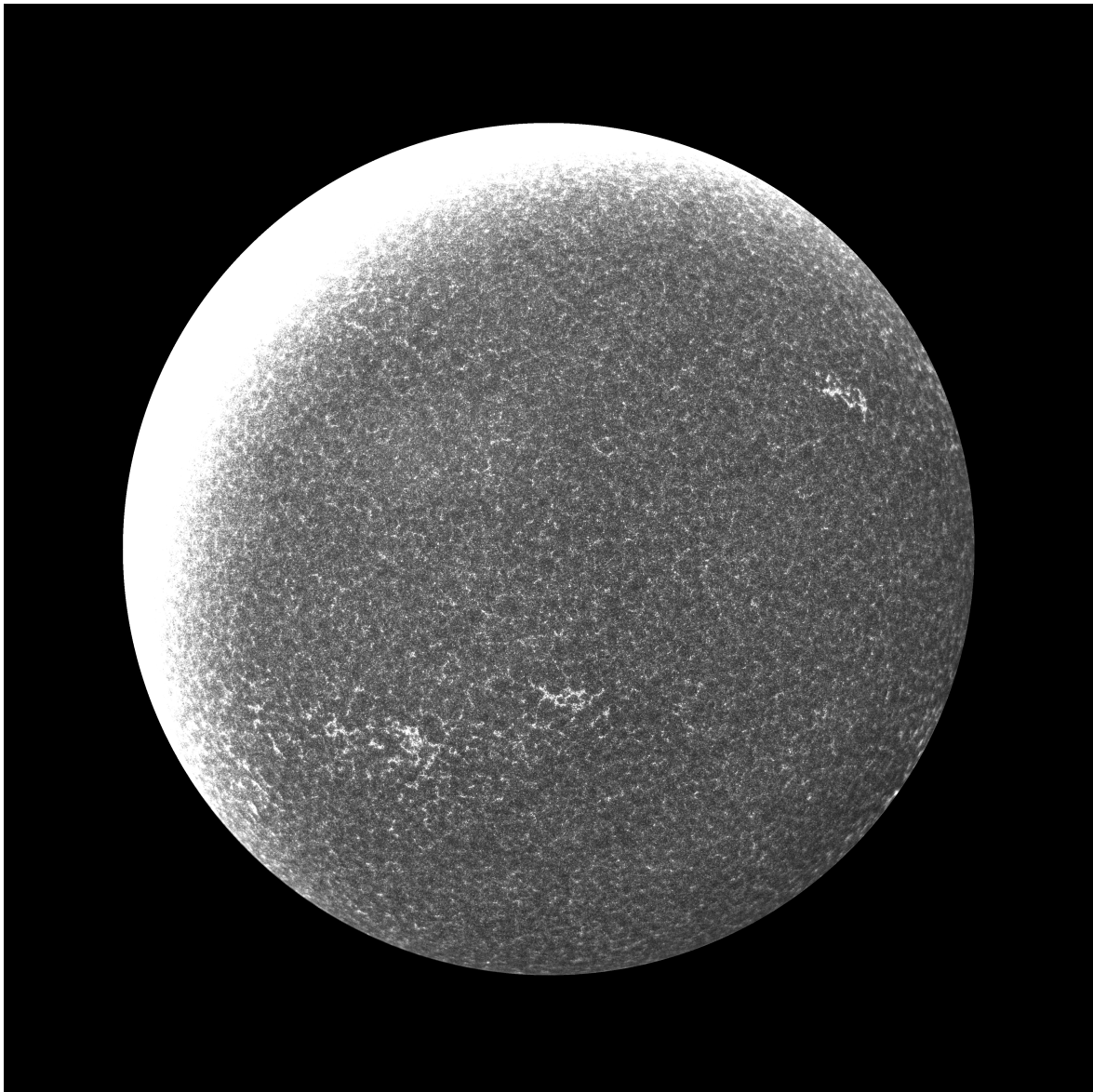


**Figure 3.6:** Initial background application with the FFT method.

appropriate amount before the division. Figure 3.7 shows the final image when the background is correctly shifted before the division.

Unfortunately this highlights another issue with this method, namely that the Fourier transformation process seems to shrink the image slightly meaning that when it is applied to the original image the limb appears brightened. Introducing limb brightening where we were trying to correct limb darkening is clearly undesirable and so suggests this background intensity correction method is also unsuitable.

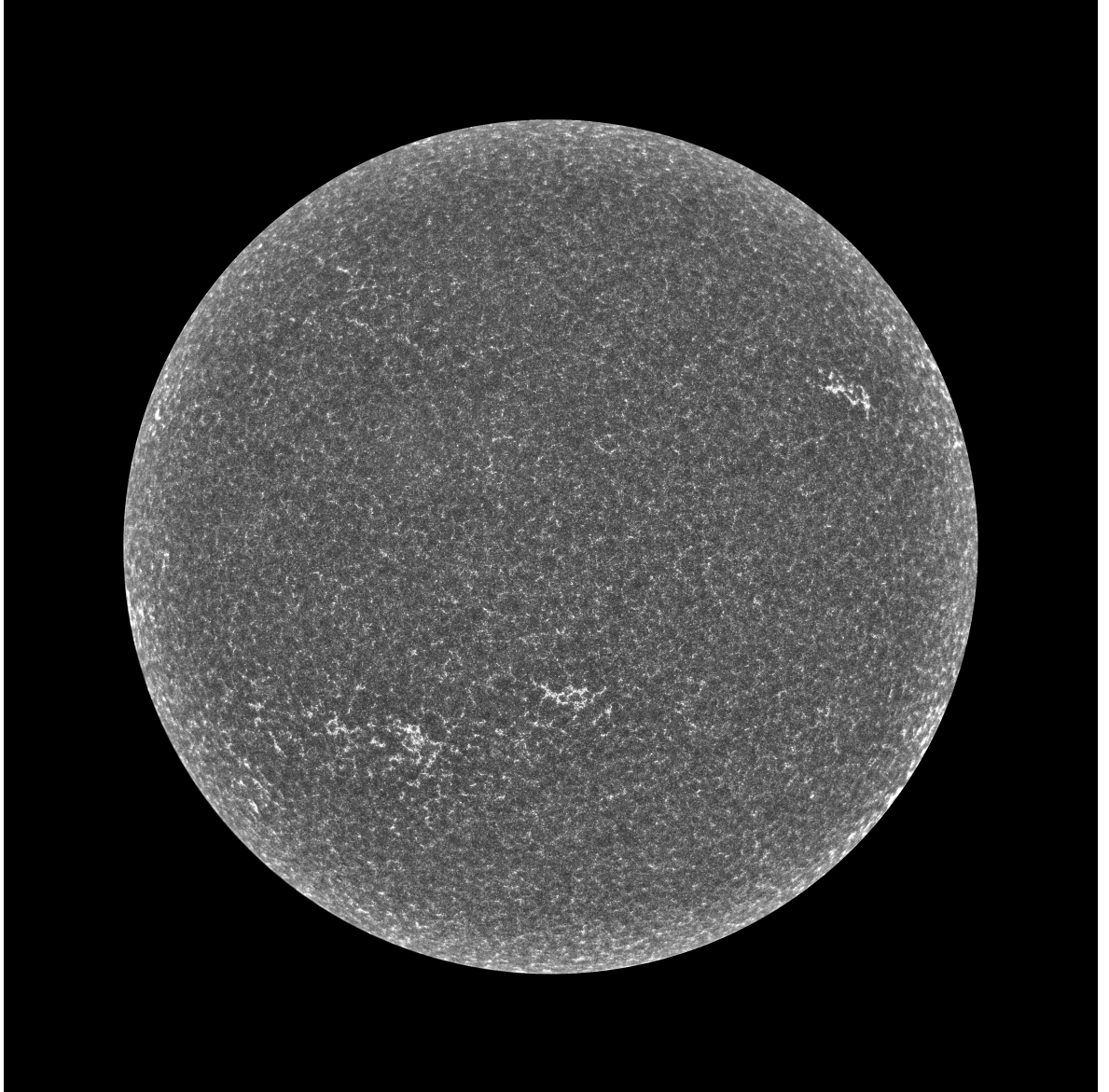


**Figure 3.7:** Final background correction with the FFT method

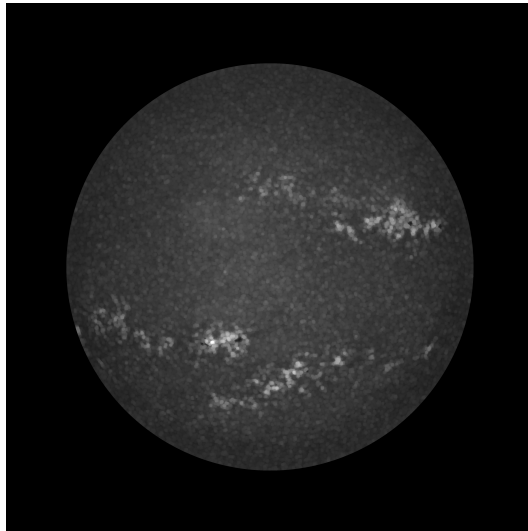
### 3.2.3 Top-hat Transform

A Top-hat transform is one of the most ubiquitous image processing techniques and a version of it is used here as the final method to create a background intensity. Technically a top-hat filter involves doing a morphological *opening* of an image and then removing this from the original image [26]. What the opening essentially does is blur the image on the scale of the top-hat filter used, creating a representation of the background intensity. The mathematical techniques involved in computing an opening are described thoroughly later in Section 4.2 where the fundamental techniques are used for feature detection.

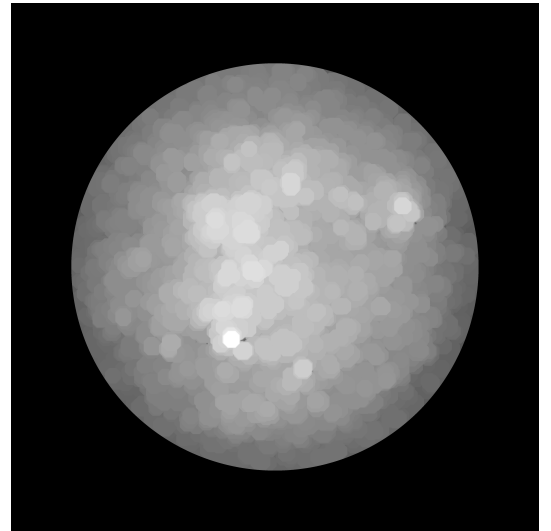
The top-hat filter as it is described serves to highlight bright features rather than equalise the image brightness across the disc. This is where we deviate from the traditional top-hat procedure since rather than subtracting the morphological opening from the original image we divide by it much as we did with the previously created backgrounds.

Given that we wish to create a relatively smooth background to divide into the original image, we use a disc shaped filter here so as not to create sharp corners or edges in the background. The size of filter we use determines to what extent the image is blurred. The effects of several variously sized filters can be seen in Figure 3.8.

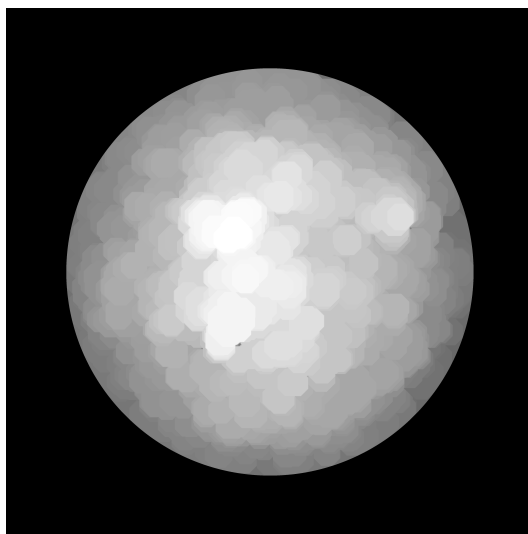
From this figure it is obvious that a large filter on the scale of several hundred to thousands of pixels is unsuitable as at that scale we begin to lose the local variations we need, and even the original shape of the image. A filter of diameter 120 pixels was used as this size of filter offers a good compromise between the time taken and the quality of background correction it offers. Figure 3.9 shows the effect of applying this correction to the quiet Sun test image.



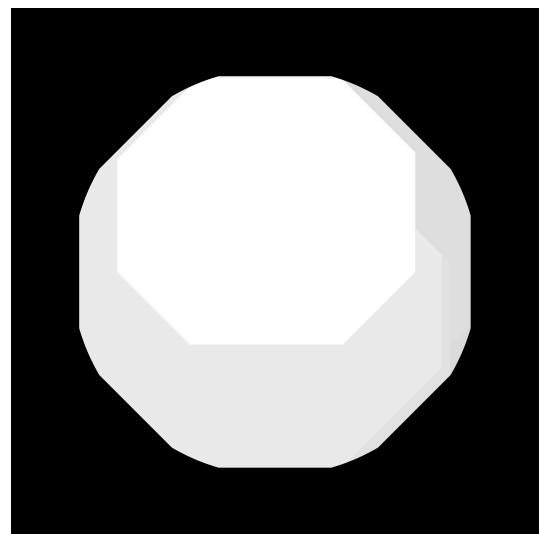
(a) Disc shaped filter of diameter 20 pixels.



(b) Disc shaped filter of diameter 120 pixels.



(c) Disc shaped filter of diameter 200 pixels.



(d) Disc shaped filter of diameter 2000 pixels.

**Figure 3.8:** The background using a top-hat transform and various filters.

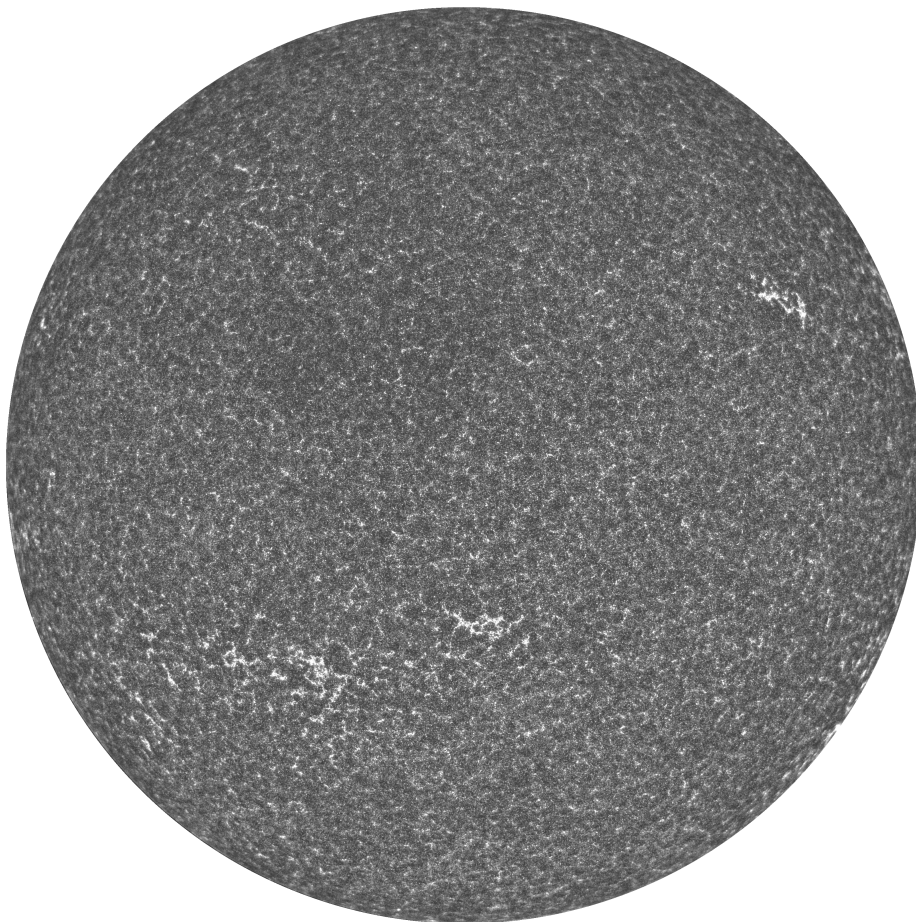


**Figure 3.9:** Final background correction with the top-hat transform method.

### 3.2.4 Comparison of Methods

Whichever method is chosen will be applied to every image subsequently analysed and so it is of great importance that not only does the chosen method sufficiently compensate for limb darkening but does not, in doing so, introduce other faults. Therefore, while at first glance there would seem to be some obvious issues with the three methods described above a more thorough comparison of them must be undertaken.

As stated earlier the time taken by each method must also be considered. Table 3.1 shows the time taken for analysing one image with each of the three. The FFT method

Method	Time (s)
MCMC	7.241
FFT	1.225
Opening	3.896

**Table 3.1:** The time taken for each background correction method.

was, as expected, the quickest of the three. The other two methods were several seconds longer, particularly the MCMC. The extra time for this method can be attributed to relatively lengthy process of determining the best fit to the limb darkening profile, whereas the longer time for the opening method is because the operation is applied to each individual pixel in the image one at a time.

Of course the time taken is not the only metric to judge the suitability of each method; the much more important factor is how well the background created represents the general brightness of the image. The most sensible way to judge this is by both simply looking at the image and by re-plotting the mean brightness across the centre of the images. If the created backgrounds are suitable the distinctive limb darkening shape we observed earlier would no longer be present and the baseline brightness across the centre would now be even.

Figure 3.10 shows that FFT method fails in this regard. This was already suspected from simply looking at the resultant image after this background was applied but the plot confirms that it does indeed brighten the limb significantly when compared to the

rest of the disc. This method was the quickest of the three (Table 3.1) but is clearly not suitable given its failing in this regard.

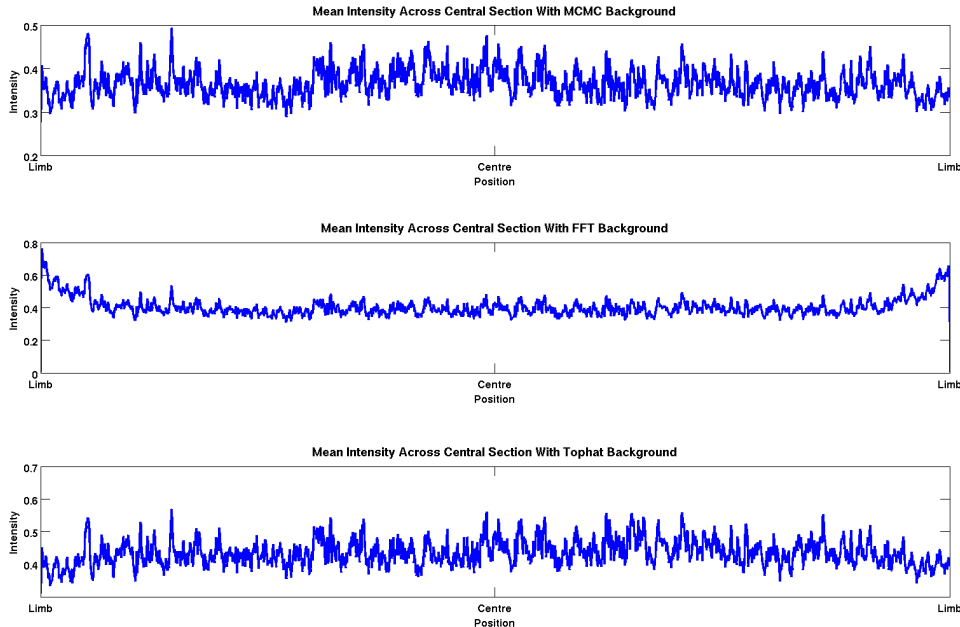


**Figure 3.10:** Mean intensity across the centre of the Sun after the three different backgrounds have been applied.

That leaves the MCMC and the Opening backgrounds. Though both of these create an even brightness profile, across the centre of the disc at least, the MCMC process takes almost double the time of the Opening. Furthermore, given the radial symmetry of this background it will be unable to account for any local variances in brightness, much as was seen earlier. These two factors combine to make the MCMC background a less suitable option and so that leaves the background created by the morphological opening.

The morphological opening clearly creates the most suitable background and while it was not the quickest process a duration of approximately 4 seconds per image is not prohibitive. The test images created earlier can be seen in Figures 3.11, 3.12 and 3.13 with the morphological background correction applied. All of them show an even brightness profile with no clearly observable faults introduced through the background correction process.

At this stage we also created another histogram of the active Sun test image to deter-

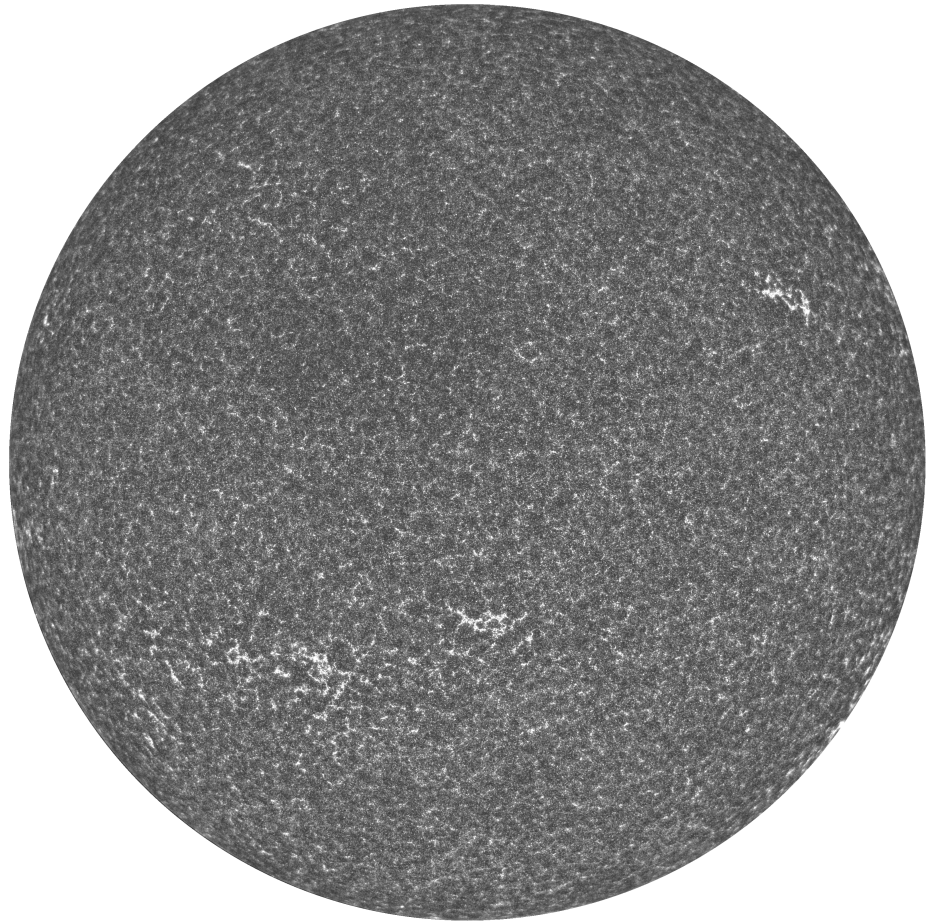


**Figure 3.11:** The quiet Sun test image with the morphological opening background correction.

mine how the chosen background correction affects the individual pixel values (Figure 3.14).

It is clear from this that the distribution of pixel values has shifted to the right, to higher values, as we would expect since we have brightened the darker regions of the image. The general shape of the distribution however remains the same as it was for the original image, confirming we have not drastically altered the image through our background corrections.

From this point on all images used throughout this work will have the morphological

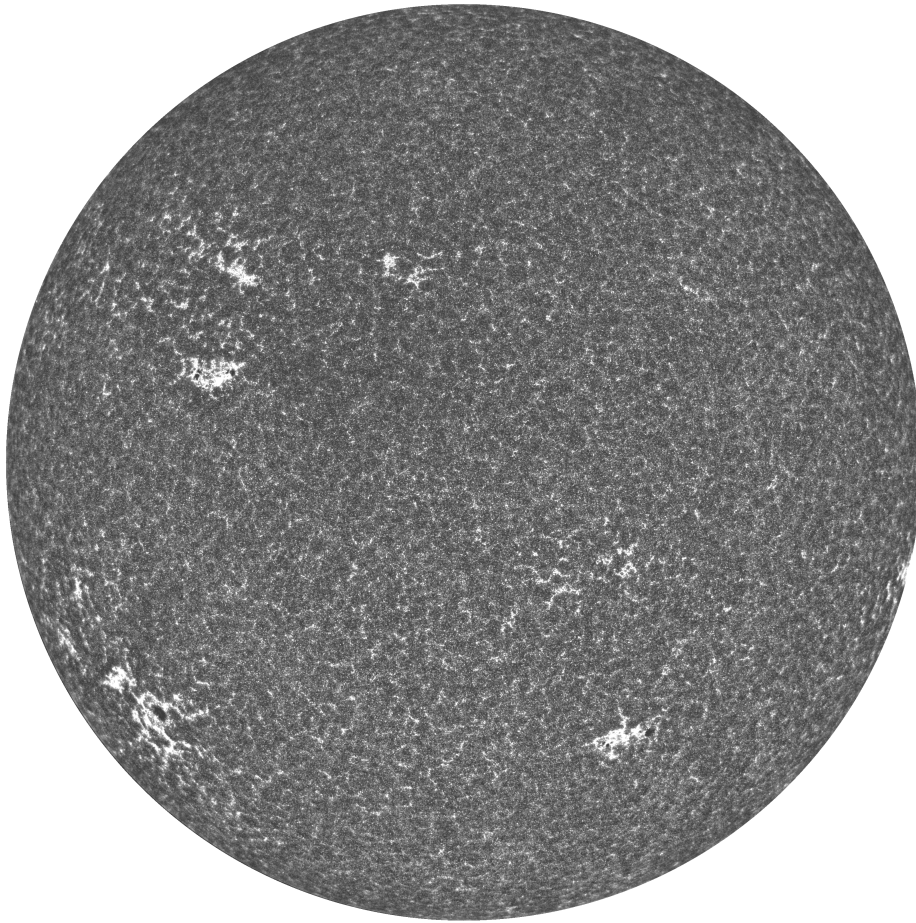


**Figure 3.12:** The medium activity Sun test image with the morphological opening background correction.

opening background correction applied to them.

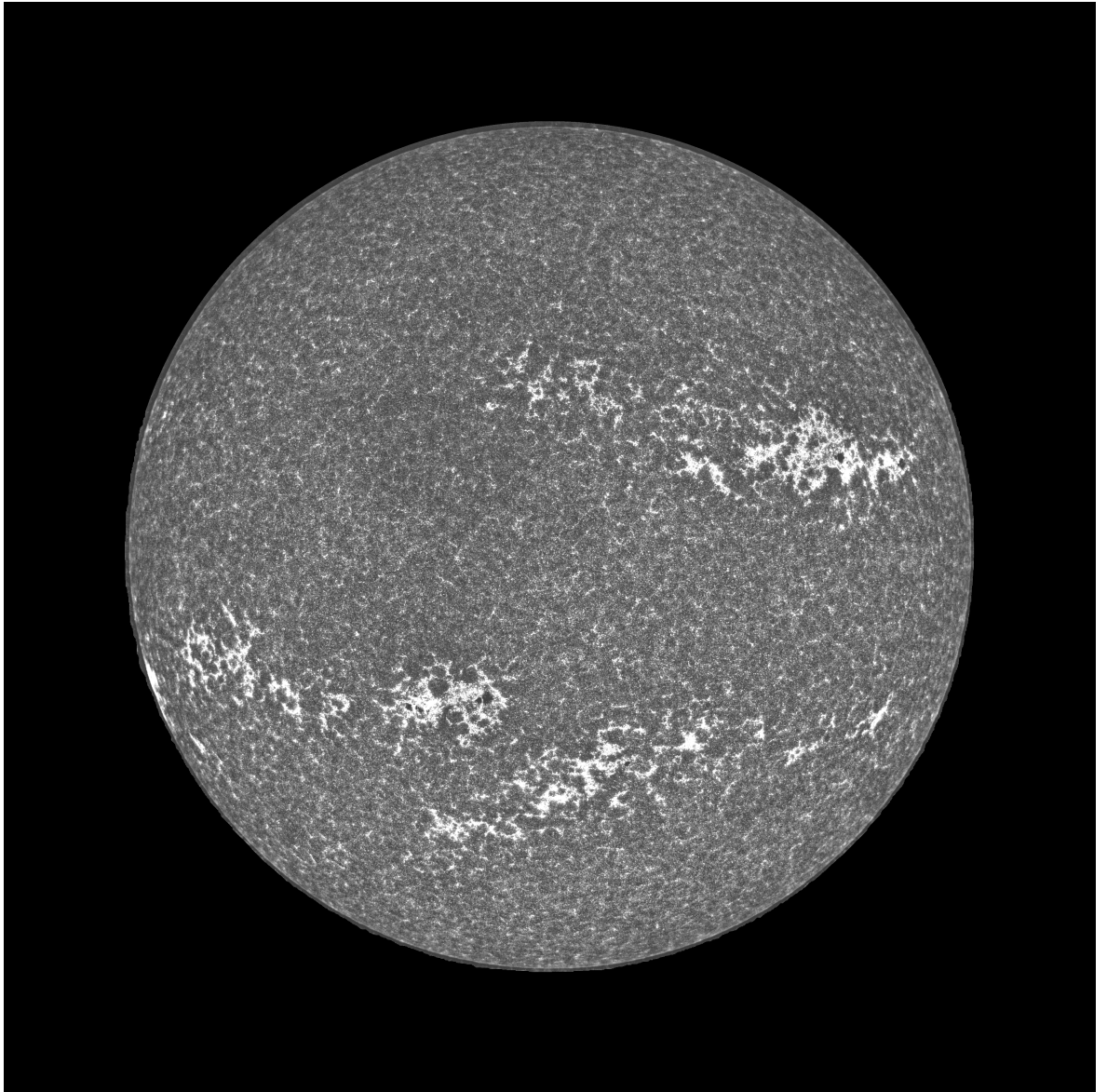


**Figure 3.13:** The active Sun test image with the morphological opening background correction.

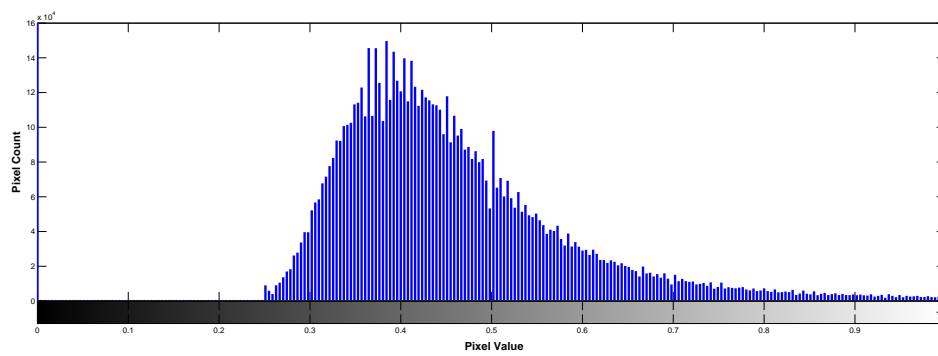


**Figure 3.14:** A histogram of the quiet Sun test image with the top-hat background correction applied.

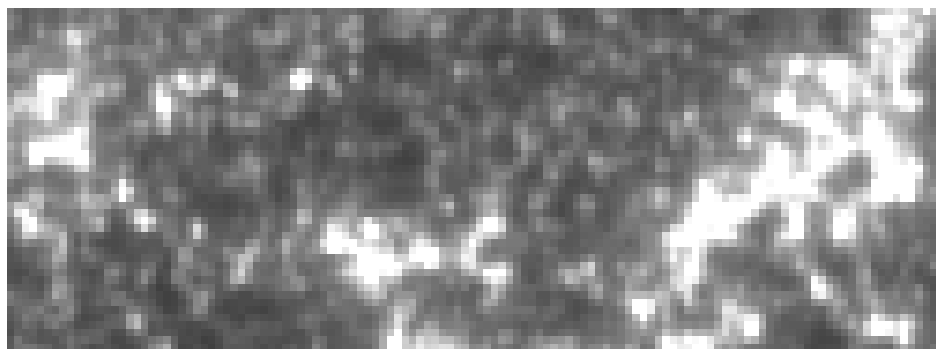
# Chapter 4

## Network Detection

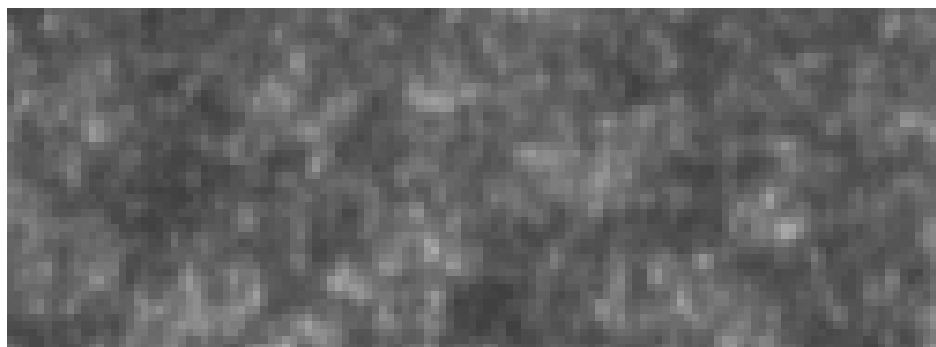
With the initial work on the calibration of the images and the improvement of the image quality completed we now begin to detail the main parts of the thesis. It is known that the network is visible over the entirety of the solar disc at UV wavelengths, and at many scales. It is also known that since the network is brighter than the background Sun it must contribute to the Total Solar Irradiance. It is hoped that by successfully detecting and quantifying the solar UV network further work could then be done to determine what percentage of the TSI is caused by said network.

The simplest way of thinking of the network is as a concentration of magnetic flux. These concentrations appear around areas where various solar processes are inhibiting magnetic field lines, namely sunspots and granulation cells, which are present over the entirety of the solar disc. As such the network is also present over the entire disc. The network found between granulation cells is however on a much finer scale than that formed around sunspots. Combined with this variety in scale the network also varies hugely in morphology.

It is clear that the detection is far from trivial, mainly due to the large variations in scale and morphology of the network. Also, while the network is consistently brighter than the background Sun the amount by which it is brighter is not equal across the disc, with the brightness ratio between network and background decreasing towards the limb. This combination of factors means it is not possible to detect the network by simply searching for a feature of standard size or shape. As such, many methods, ranging in complexity, need be tried.



(a) Small test section at the centre of the active Sun test image.



(b) Small test section at the limb of the active Sun test image.

**Figure 4.1:** The two small zoomed in test images for detection method evaluation.

The development of the various detection methods and an evaluation and comparison of their effectiveness constitutes the rest of this chapter.

Here we must also discuss how in fact we are to judge the effectiveness of a detection method. There is no known pattern to the network or disc covering percentage that we can use to quantitatively judge a detection and simply stating that a method seems to be correct is not substantive enough. To this end we take two small sections from the active test image shown in Figure 2.9 in which *we* can identify the network. These two regions are taken from an active area towards the centre of the Sun and a much quieter area at the limb and can be seen in Figure 4.1.

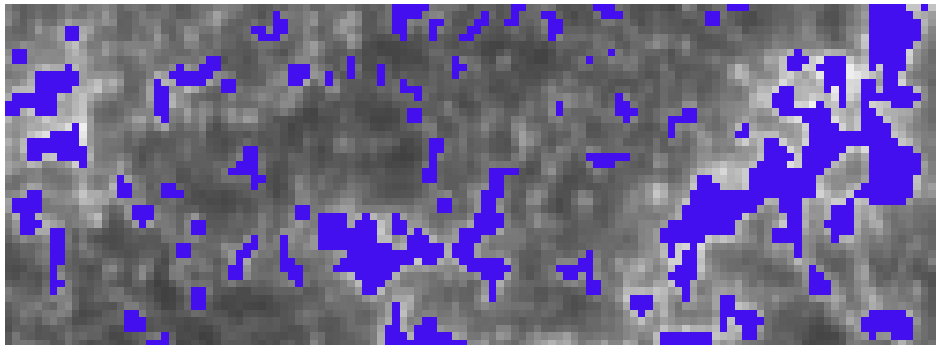
Both of these regions are very small, only 125 by 45 pixels, so that we can more easily determine whether individual pixels are network or not. On these images we mark pixels that we deem to be network in blue (Figure 4.2).

The characterisation of a pixel as network is of course subjective but here we use the condition that it is either close to the maximum brightness present in the image *or* if it forms part of a structure that is on average brighter than the darker background.

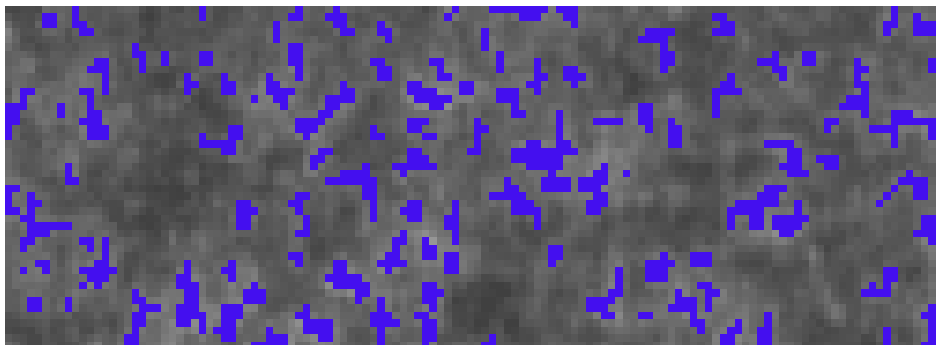
Note that we don't mark *all* the pixels that we deem to be network, just a selection of those within larger areas of both bright and dim network that a successful detection method must detect. Therefore we expect a successful detection algorithm to detect *all* the pixels shown in blue. We would also expect a successful detection method to mark other pixels as network, namely those that form part of a large bright structure or those that are significantly brighter than the background. If a detection method should mark *all* the pixels in the image as network it is clearly unsuccessful as it should also detect a minimum (ideally none) of the darker background pixels. It should be noted that when we refer to darker background pixels we mean those that are significantly darker than the brightest network and do not form the same web like structures exhibited by the network.

We then compare each detection method once it is fully developed to these smaller sections as a test of their effectiveness. This of course is not a definitive test, as whether one pixel can be designated network or not is still a somewhat subjective method and is dependant on a human observer, but using the criterion outlined above is perhaps the best we can do.

The methods used for network detection can be categorised as follows: brightness-based detection methods and morphological-based methods. There are benefits, and of course deficiencies, to both these methods, which will be examined and discussed in detail in this chapter.



(a) Small test section at the centre of the active Sun test image with a number of network pixels marked in blue.



(b) Small test section at the limb of the active Sun test image with a number of network pixels marked in blue.

**Figure 4.2:** The two small zoomed in test images for detection method evaluation.

## 4.1 Brightness Based Detection

The simplest of the detection methods, both in concept and computationally, are those based on the brightness of the network. These methods use simple thresholds to determine whether a pixel is determined to be network or not, and due to having this simplicity at their core they also run rather quickly. This is not an insignificant factor when judging the utility of a detection method.

### 4.1.1 Basic Threshold

The first detection method attempted was a very basic threshold on the pixel values. It has already been stated that a straightforward detection method, such as basing the network detection on a uniform brightness level, would be unlikely to work. Despite this, using a basic threshold is such a simple method that not much is lost in the attempt. Further, it serves as something to compare more complex methods against as well as possibly highlighting the areas that more complex methods need improve upon.

Given the scale of the network compared to that of the solar disc it would be difficult to fine tune a detection method when viewing the whole of the disc. Instead we look at three regions of the active Sun test image that share properties of the individual whole disc images, that is we look at a quiet, medium activity and heavily active section. Each of these smaller sections is 400 by 400 pixels and are shown in Figure 4.3. We fine tune our detection on these smaller sections and then apply it to the whole disc images.

Several different thresholds were tried. The data had already been normalised so the pixels values ranged from 0 to 1. First the thresholds were set at 0.1 value intervals between 0.2 and 1 (the histogram in Figure 3.14 shows that very few pixels have a value lower than 0.2). This was done to all three of the test sections to test the thresholds on all levels of solar activity.

Figures 4.4, 4.5 and 4.6 show the results of such thresholds with the pixels detected as network by the threshold shown in red.

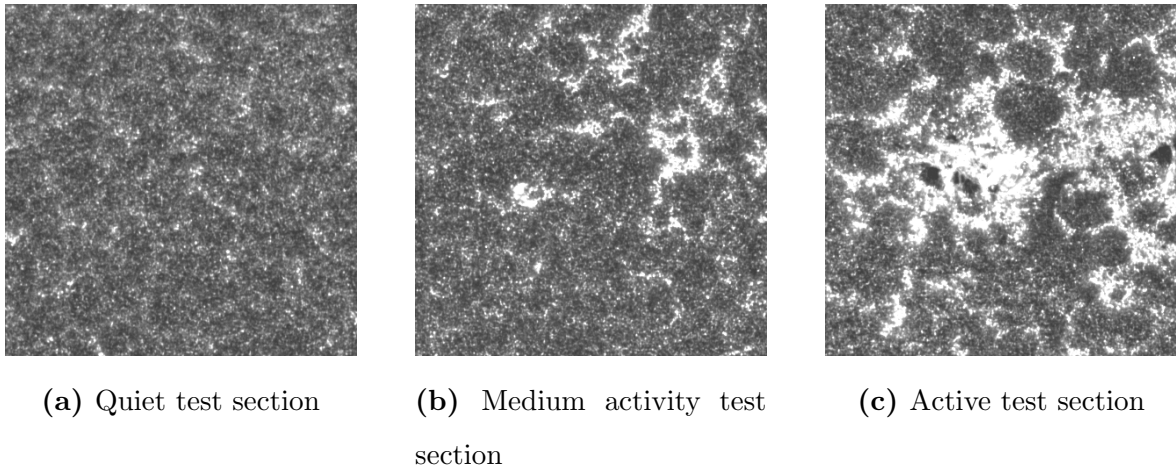


**Figure 4.3:** Three small test sections for the development of detection methods.

It is clear from these figures that a threshold which may detect well in active sections does less so in the quieter areas and vice versa. It seems that a constant-value threshold cannot detect equally well across the disc and so a certain level of activity must be given preference. Here we decide that the priority should be on the active section as it contains larger, more defined, features making it easier to judge whether the detected network meshes with the feature boundaries.

Doing so suggests that the most suitable threshold lies between 0.4 and 0.5 so we now test this range, at intervals of 0.01. Figure 4.7 shows the results of this with the detected network again shown in red.

From Figure 4.7 it would seem that the network detected by a threshold of value 0.45 gives a good representation of the network. This then is the most suitable basic threshold for the full disc solar images, though it may fail in the quieter dimmer areas of the Sun. Such a judgement however is very subjective. In an attempt to rectify this we turn to the extremely small sections in which *we* identified the network (Figure 4.1). First we look at that same area, showing the pixels detected as network by our threshold in red, and then overlay on that the pixels we defined as network in blue. When the two overlap, that is, when a pixel was detected as network by both us and the algorithm we highlight those in green. The hope is that a successful method will have detected *all* of those that we did and so there should be no blue pixels in the final image, just green and red. What we in fact see here though is that the basic threshold

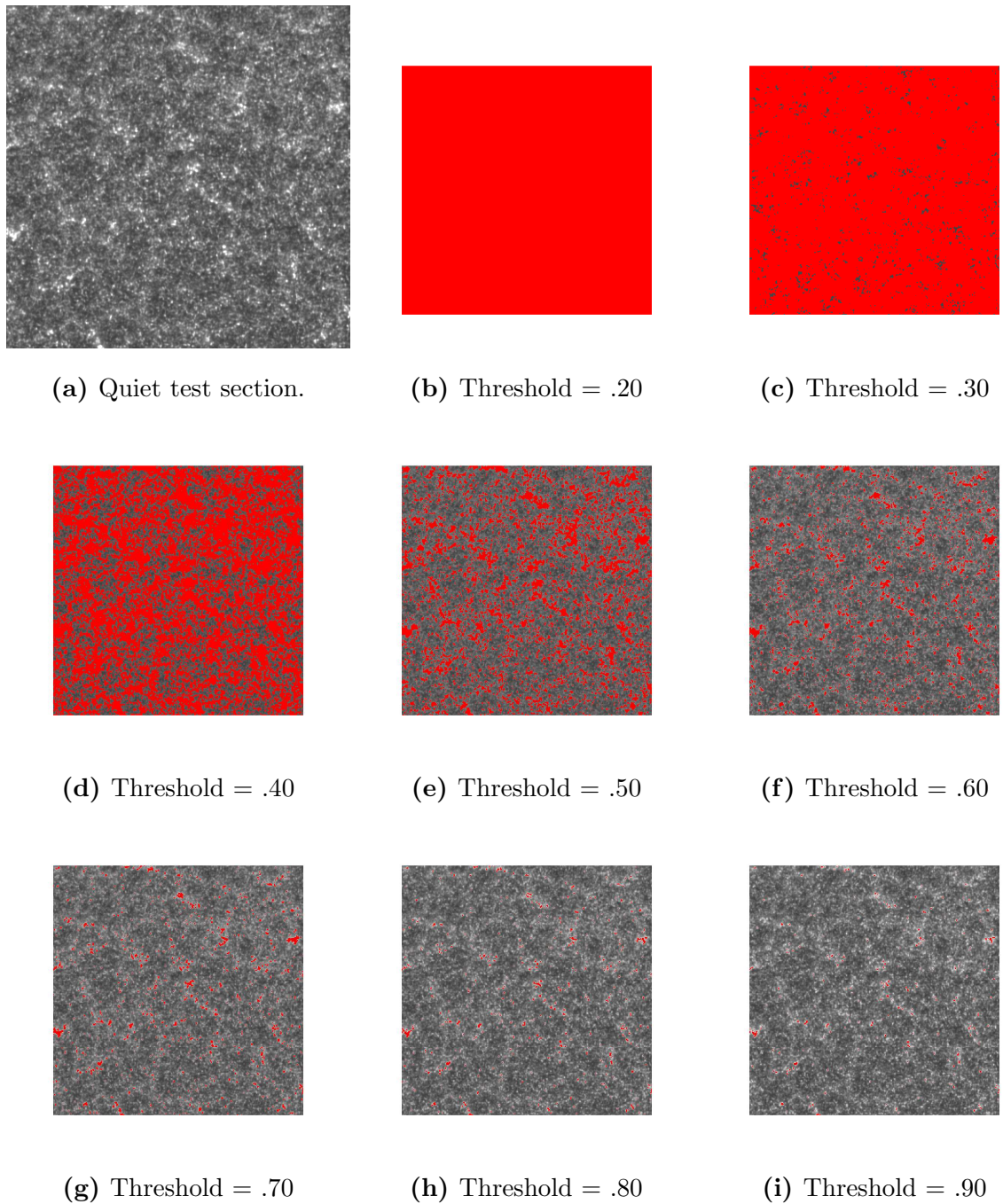


**Figure 4.4:** Quiet test section with increasing thresholds.

works well at the centre of the Sun, detecting almost all the pixels we designated (Figure 4.8) and the rest of the surrounding network but fails to detect many of the same pixels we did at the limb (Figure 4.9).

Though we know this method to be rather unsuccessful we use it on the full disc test images seen in Figures 3.11, 3.12 and 3.13. The network detected in these test

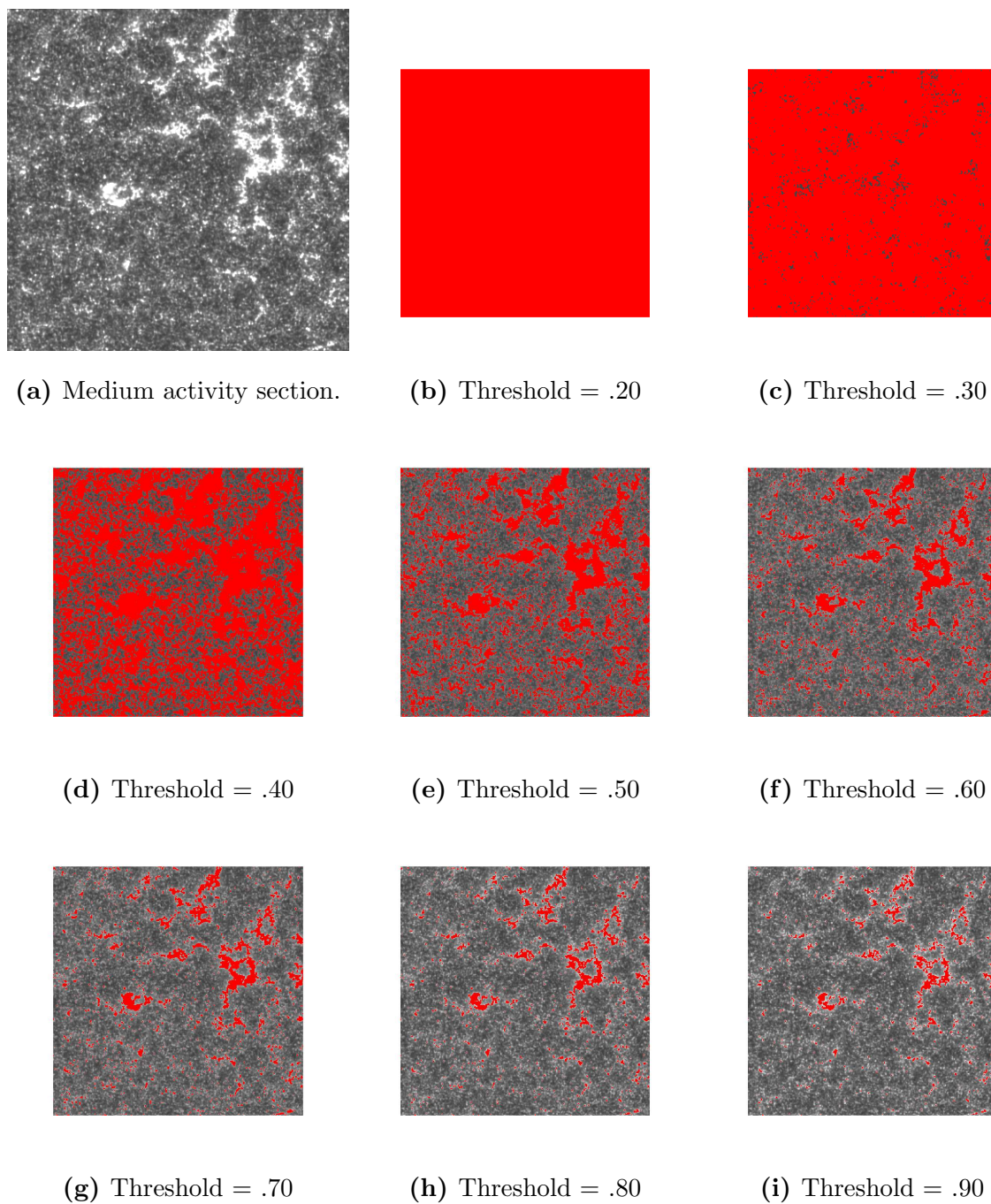
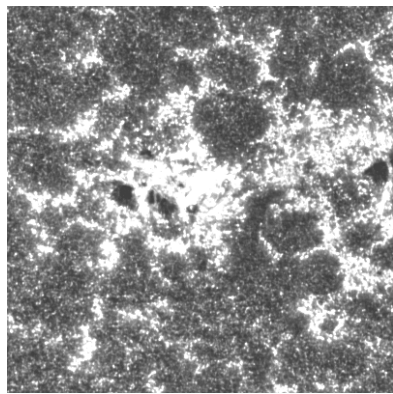


**Figure 4.5:** Medium activity test section with increasing thresholds.

images will not be an accurate representation of the actual network but it serves to compare later methods to. The fraction of the full solar disc detected as network with this method is given in Table 4.1.

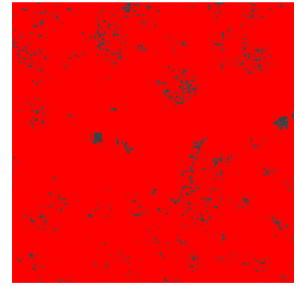
As expected we find that a greater network covering is found when the Sun is active, due to the presence of the large active regions. The fact that this detection method



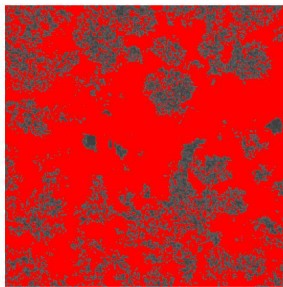
(a) Active test section.



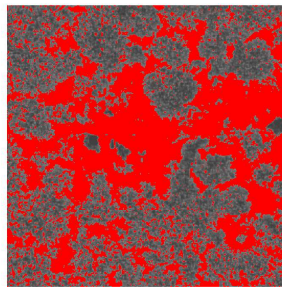
(b) Threshold = .20



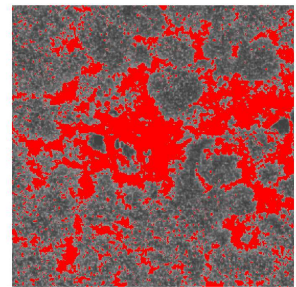
(c) Threshold = .30



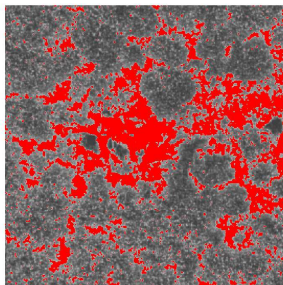
(d) Threshold = .40



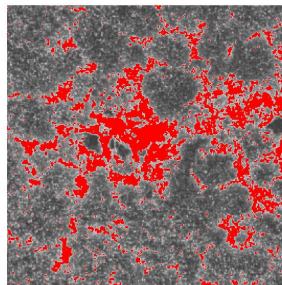
(e) Threshold = .50



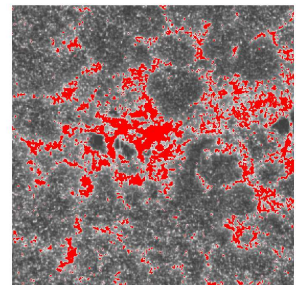
(f) Threshold = .60



(g) Threshold = .70



(h) Threshold = .80



(i) Threshold = .90

**Figure 4.6:** Active test section with increasing thresholds.

fails towards the limb though is interesting. It suggests that either the background correction we applied does not wholly counter the presence of limb darkening or that the network towards the limb is less bright relative to the surrounding material than the network at the centre of the Sun.

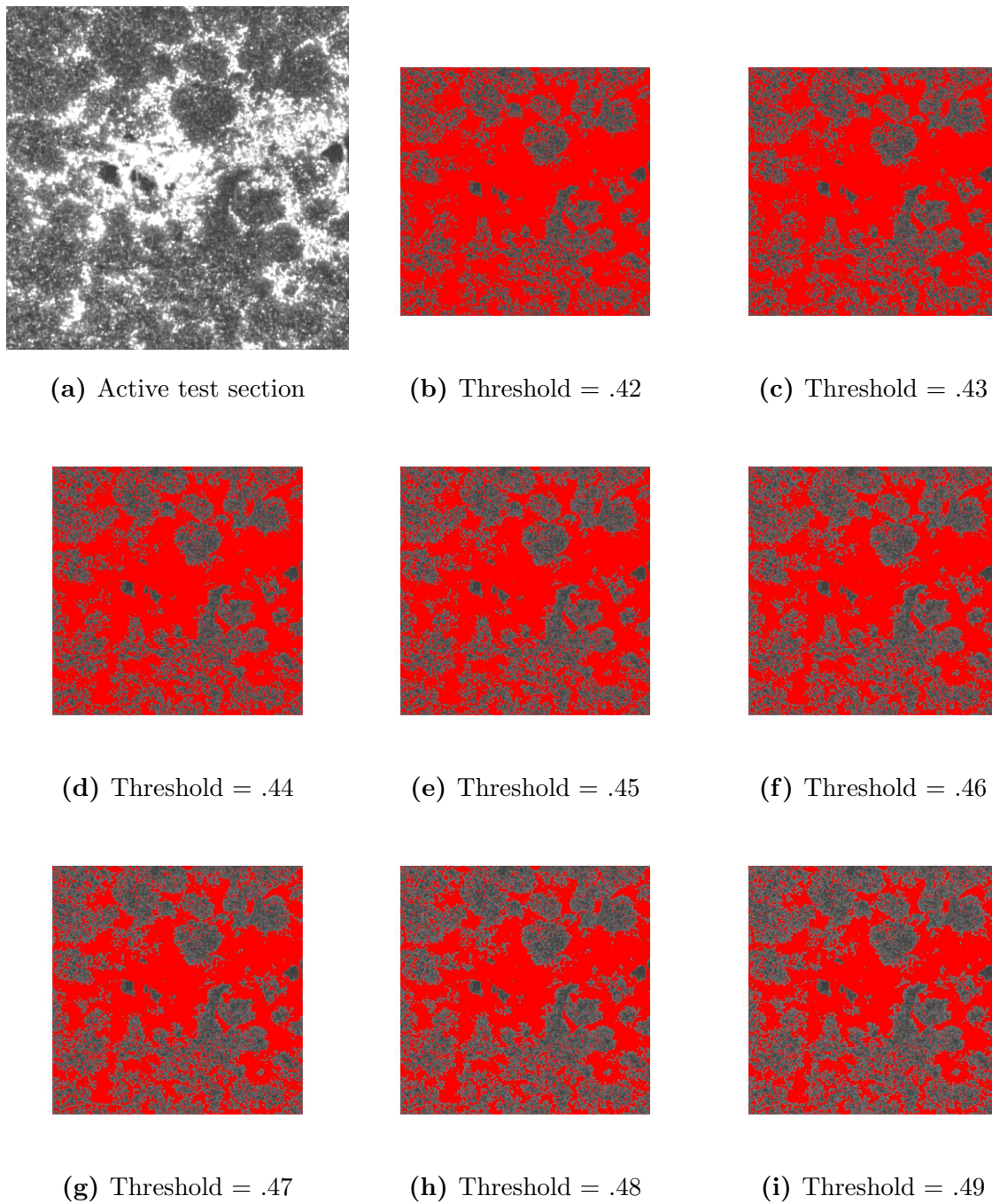
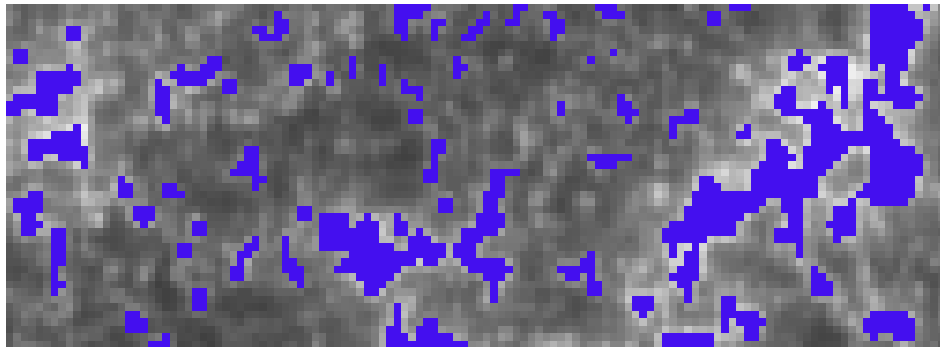
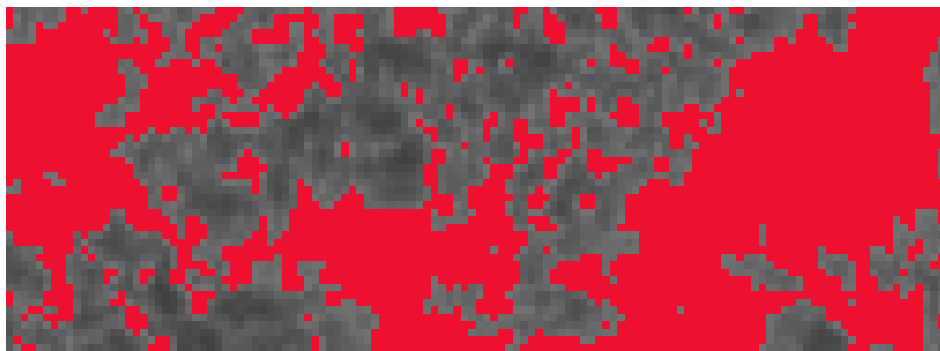


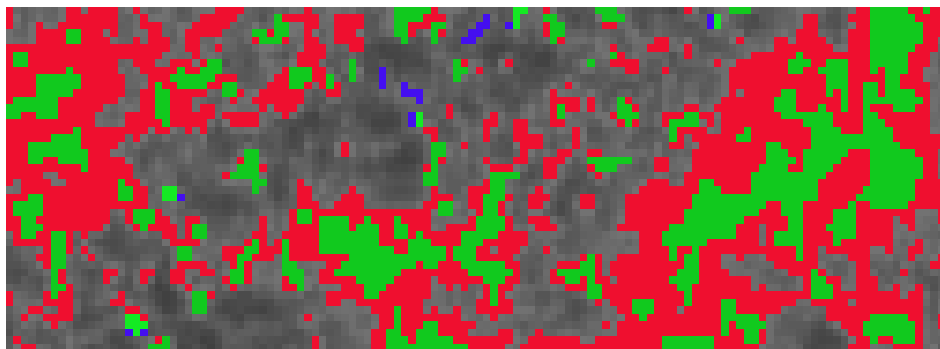
**Figure 4.7:** The results of using a fine tuned increasing basic threshold on the active test section.



(a) A number of network pixels determined by us.

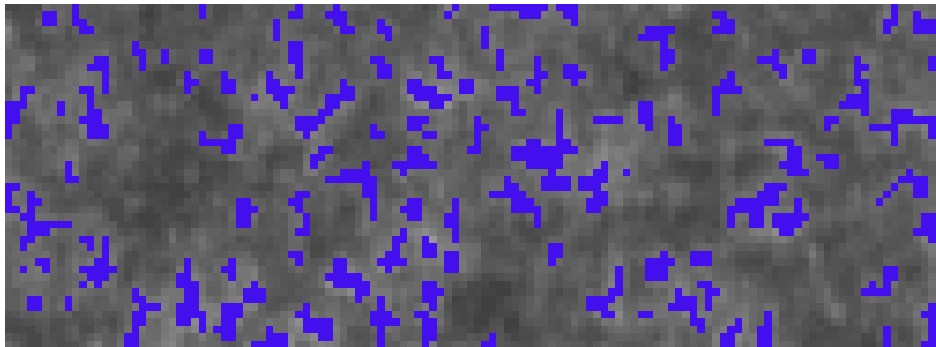


(b) Network detected by threshold of value 0.45

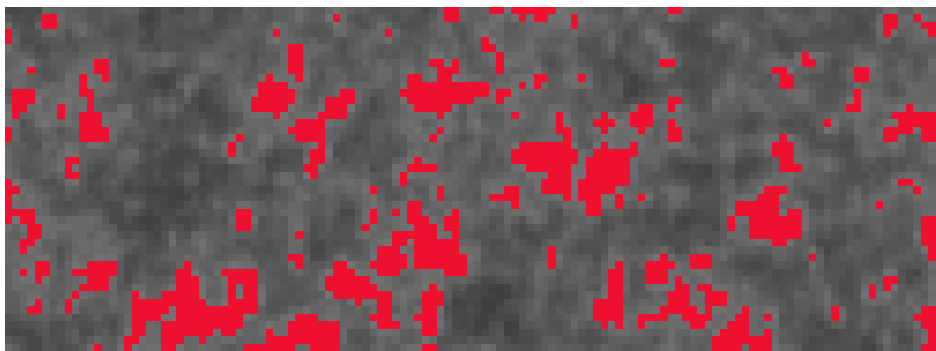


(c) Network detected by us and the algorithm, with the pixels where these overlap shown in green.

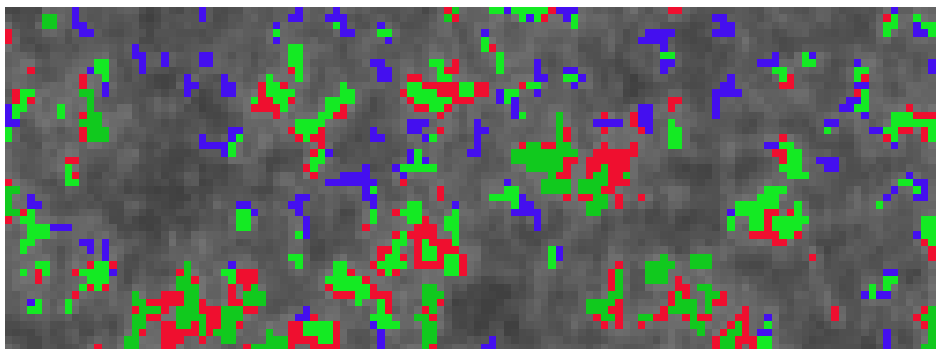
**Figure 4.8:** Test of the basic threshold's effectiveness at the centre of the active Sun test image.



(a) A number of network pixels determined by us.



(b) Network detected by threshold of value 0.45



(c) Network detected by us and the algorithm, with the pixels where these overlap shown in green.

**Figure 4.9:** Test of basic threshold's effectiveness at the limb of the active Sun test image.

Test Image	Detected Network
Quiet Sun	29.74%
Medium Activity Sun	31.06%
Active Sun	41.89%

**Table 4.1:** The fraction of pixels identified as network at a basic threshold of 0.45 for the three full disc test images.

### 4.1.2 Concentric Thresholds

This is also a thresholding method but is a little more complex than the one used previously. We have already stated that the largest problem with the simple threshold was its uneven detection of the network over the solar disc. To address this we attempt to use a different threshold in different areas of the disc. Given the problem seems to be one of radial differences in the network intensity a solution presents itself - split the disc into a series of concentric sections, using an appropriately sensitive threshold within each.

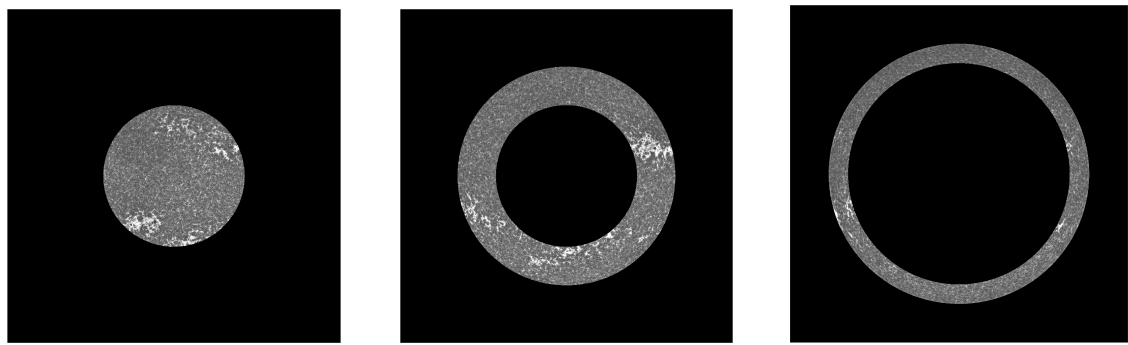
The number of concentric sections used must first be decided upon. If we choose too few we run the risk of not gaining anything from it compared to the basic threshold, whereas if we choose too many sections the time taken for the procedure will increase to the point of being prohibitive.

The previous section suggests that a threshold normalised intensity value of about 0.45 is reasonable so that will serve as the starting point for all thresholds tested here. Further, we know that the threshold value need not be changed in the centre of the disk, but that it should be set a little lower towards the limb. It was decided that separating the disk into three concentric sections would be enough, as this allows us to account for both the over-detection at the centre of the disk and the under-detection towards the limb, without increasing the length of the processing time by too large an amount.

The boundaries of the three sections were set so that the inner section spans from the center of the Sun out to 0.55 solar radii, the middle section from here to 0.85 solar radii and the outer section from here to the limb. These boundaries applied to the active Sun test image can be seen in Figure 4.10.

In attempt to identify possible thresholds to use, rather than just basing them on the previous method we use the previous basic threshold detection method and calculate the covering percentage for a large range of values. The hope here is that when the covering percentage is plotted against the threshold, steep gradients in the trend will identify important thresholds to be investigated. The thresholds used spanned pixel values from 0 to 1 at 0.01 intervals and the resulting plot is shown in Figure 4.11.

However, this figure shows a very smooth trend between the covering percentage and



(a) Inner Section

(b) Middle Section

(c) Outer Section

**Figure 4.10:** The three sections used for the concentric thresholding technique.

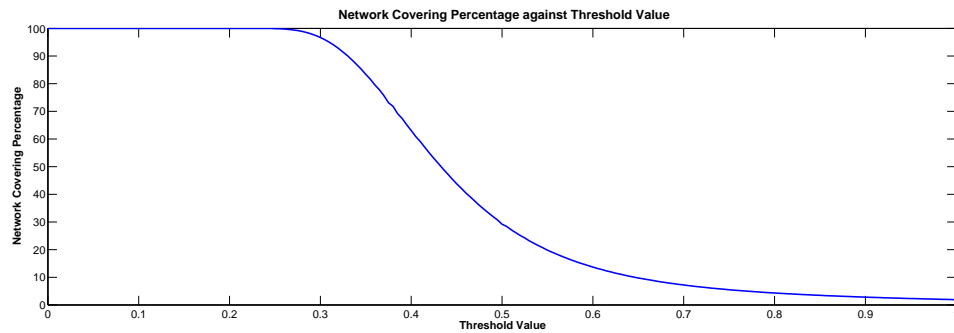


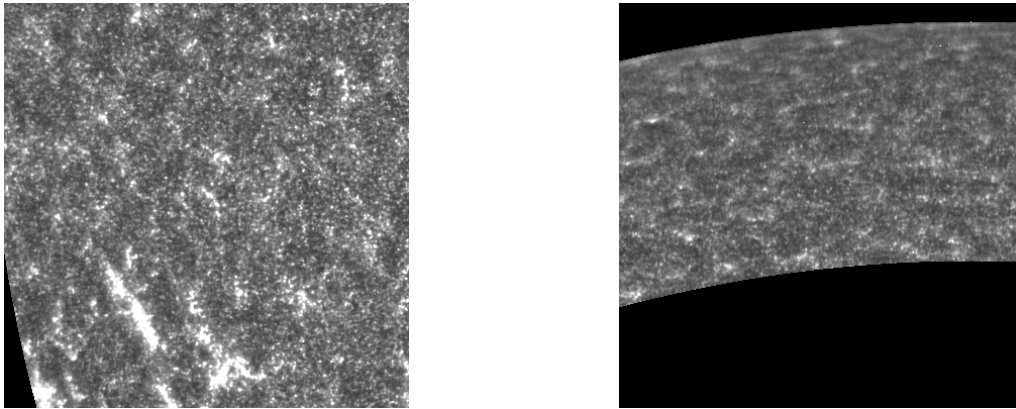
**Figure 4.11:** The network covering percentage plotted against the threshold at which it was detected.

threshold, with no clear indication of threshold values of particular interest.

Thus, much as we did when testing the basic threshold in the previous section we test the threshold again on smaller 400 by 400 pixel sections. Unlike earlier where we chose the sections based on the activity of the Sun here we take a section from each of the concentric sections shown in Figure 4.10. These sections can be seen in Figure 4.22. We do not, however, test thresholds within the inner section as although the previous detection method failed overall, it at least showed that a threshold value of 0.45 is appropriate for this inner section.

Given that the regions clearly need different thresholds, the range of threshold values tried in each section differs slightly and can be seen in Table 4.2.

The effectiveness of each method was once again judged by how well it fit to the most



(a) Test section from the middle concentric ring.

(b) Test section from the outer concentric ring.

**Figure 4.12:** The two test sections used for the development of the concentric threshold detection method.

Section	Thresholds Used							
Middle	0.430	0.435	0.440	0.445	0.450	0.455	0.460	0.465
Outer	0.380	0.385	0.390	0.395	0.400	0.405	0.410	0.415

**Table 4.2:** The thresholds tested in the concentric sections for network detection.

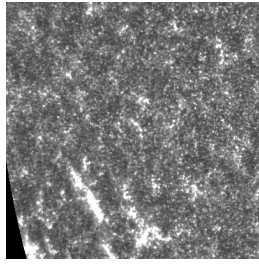
distinctive of the features present in each section while later the detection over the entire disc will be tested using the zoomed-in images used earlier (Figure 4.1, where individual pixels are visible).

First we start by determining a suitable threshold for the middle section using the values given in Table 4.2. The results of this are shown in Figure 4.13.

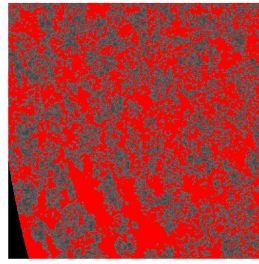
Figure 4.13 suggests that a threshold value of 0.435 would be most suitable here as this threshold detects the most network without going beyond the original feature boundaries.

This process is repeated for the outer section, shown in Figure 4.14, and using the same criteria a threshold of value 0.405 is chosen here.

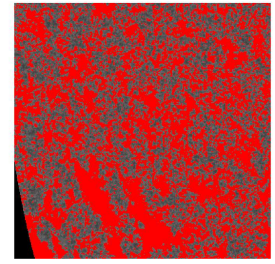
While using a different threshold in each area may detect the network in each area



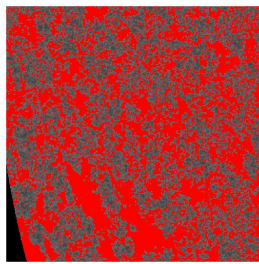
(a) Test section within middle concentric ring



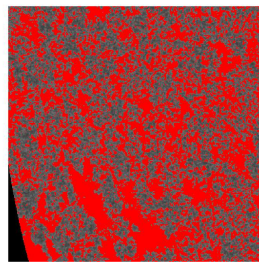
(b) Threshold = 0.430



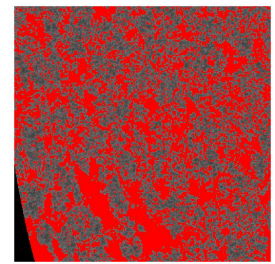
(c) Threshold = 0.435



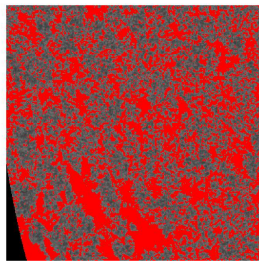
(d) Threshold = 0.440



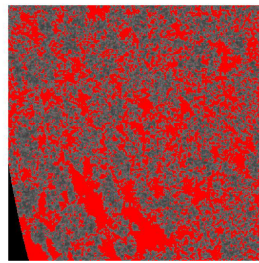
(e) Threshold = 0.445



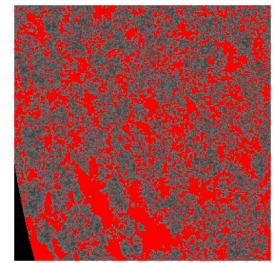
(f) Threshold = 0.450



(g) Threshold = 0.455



(h) Threshold = 0.460

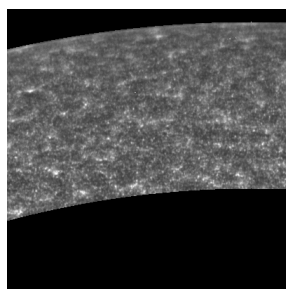


(i) Threshold = 0.465

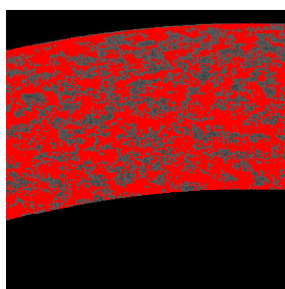
**Figure 4.13:** The results of using increasing threshold values for the test section within the middle concentric ring.

very well we run the risk of when these individual rings are combined back together there is a clear difference in the network detected in each, resulting in very visible band like structures in the final image. Figure 4.15 shows just this.

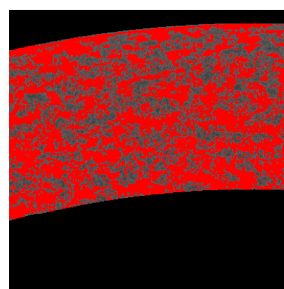
To ensure that this does not happen we combine the individual rings to estimate the network coverage for the whole disc. This is shown in Figure 4.16.



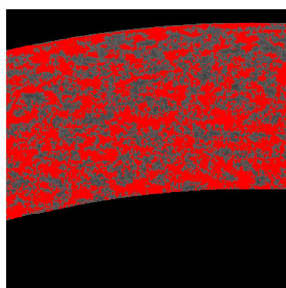
(a) Test section within outer concentric ring.



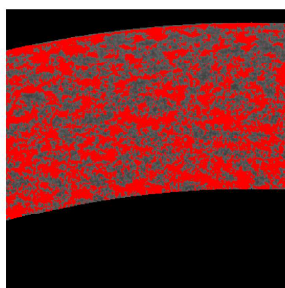
(b) Threshold = 0.380



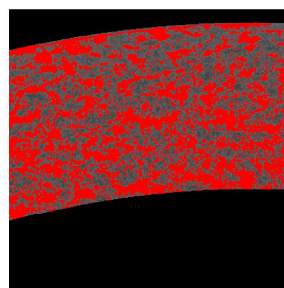
(c) Threshold = 0.385



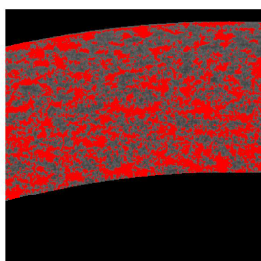
(d) Threshold = 0.390



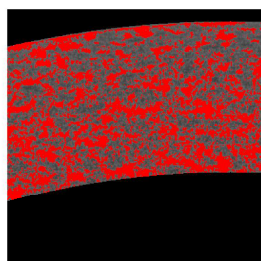
(e) Threshold = 0.395



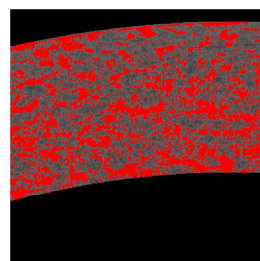
(f) Threshold = 0.400



(g) Threshold = 0.405



(h) Threshold = 0.410



(i) Threshold = 0.415

**Figure 4.14:** The results of using increasing threshold values for the test section within the outer concentric ring.

Looking at Figure 4.16 it appears that there is no major banding created by the separate rings but we examine it in more detail to make sure of this. We first take two small sections of the image, each at a region where the bands meet. We then increase the size of the inner section so that it overlaps the middle, and increase the size of that

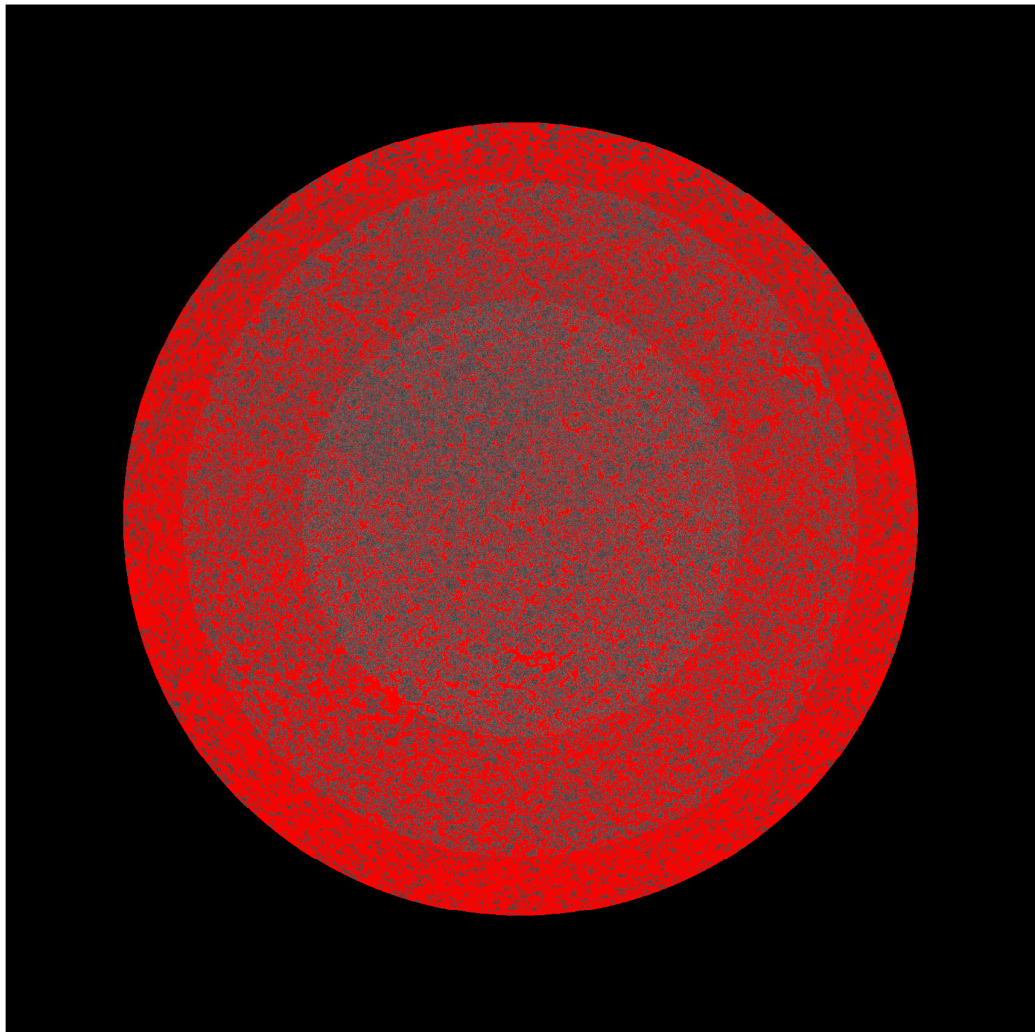


**Figure 4.15:** An example of unwanted banding using the concentric section thresholds.

so it overlaps the outer.

In this overlap section we then mark only the pixels that are detected by *both* thresholds. If this aligns with what is detected by the individual thresholds then it suggests that the transition from one ring to the other is appropriately smooth. Figure 4.17 shows this for the middle and outer overlap sections with the pixels that are detected by both thresholds shown in green. This figure shows that the pixels detected by both thresholds within the overlap section align very well with each separate threshold, suggesting a smooth detection transition between the regions and so requiring no fine tuning of the currently used thresholds.

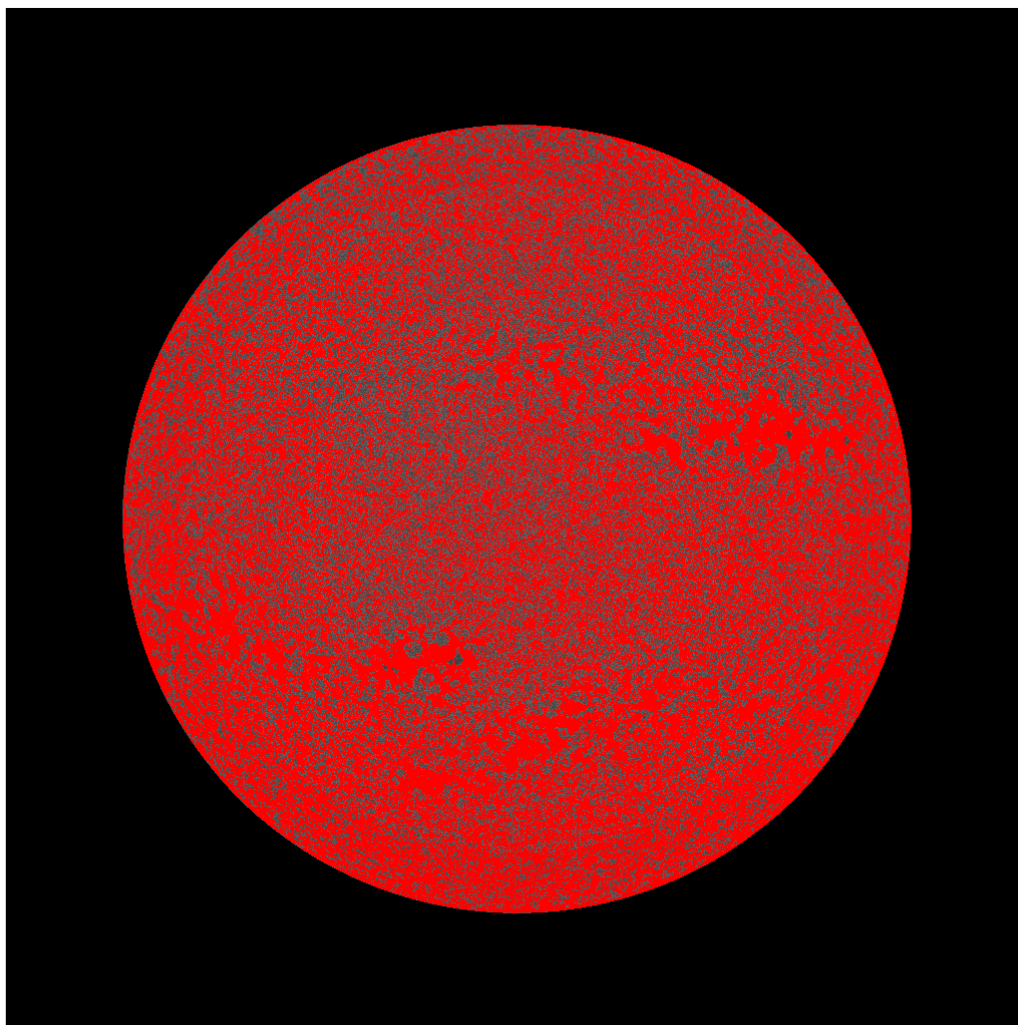
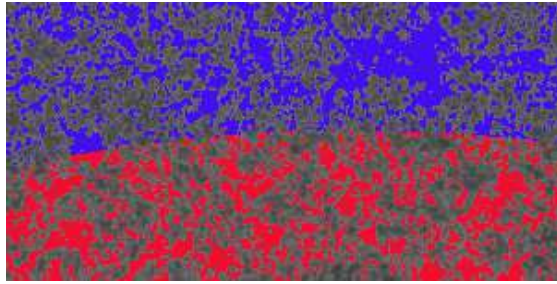


**Figure 4.16:** Active Sun test image with final concentric thresholds applied.

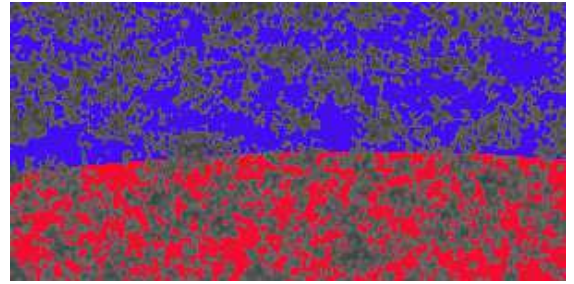
Once again to lend some level of qualitative judgement on the methods effectiveness we look at the very small 125 by 45 pixel sections where we have marked network pixels (Figures 4.18 and 4.19).

From this we can see that the use of concentric thresholds detects the network very well at the centre as it detects almost all the ones we designated here. Further, the pixels detected as network at the limb align with those we designated network much more than with the use of the basic threshold.

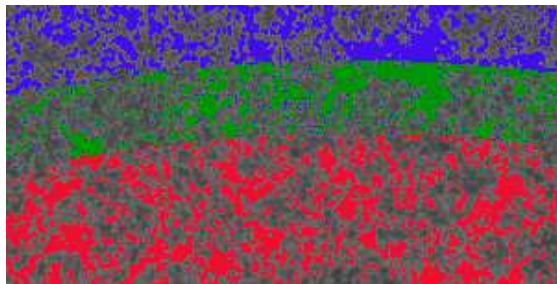
While obviously the percentage of network detected here is larger than was seen using a basic threshold the relationship between network covering and solar activity



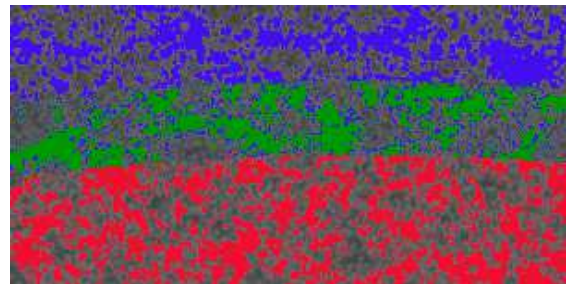
(a) The original threshold boundaries where the inner and middle rings meet.



(b) The original threshold boundaries where the middle and outer rings meet.



(c) The overlap section between the inner and middle sections with the pixels detected by both thresholds shown in green.



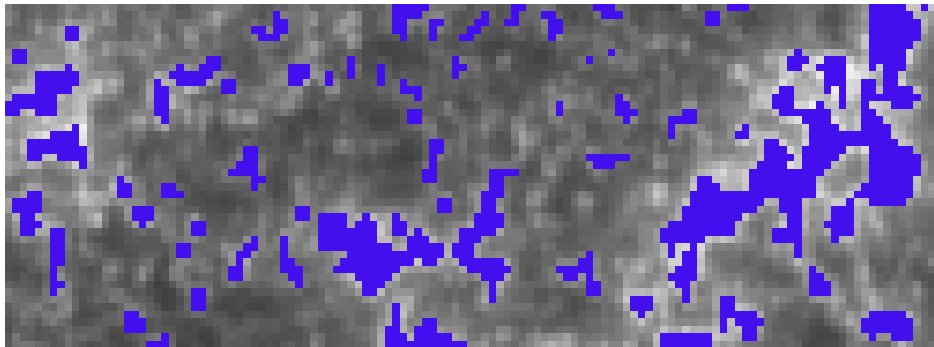
(d) The overlap section between the middle and outer sections with the pixels detected by both thresholds shown in green.

**Figure 4.17:** A test of whether the concentric thresholds create a smooth overall detection.

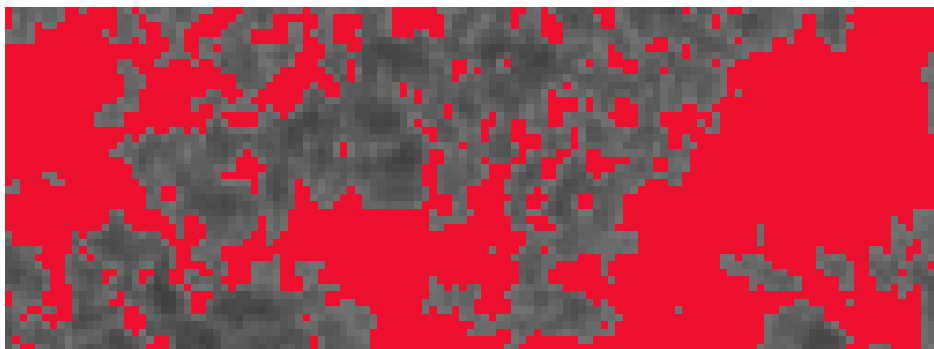
Test Image	Detected Network (%)
Quiet Sun	32.29
Medium Activity Sun	35.59
Active Sun	44.73

**Table 4.3:** The fraction of pixels identified as network using the final concentric thresholds on the three test images.

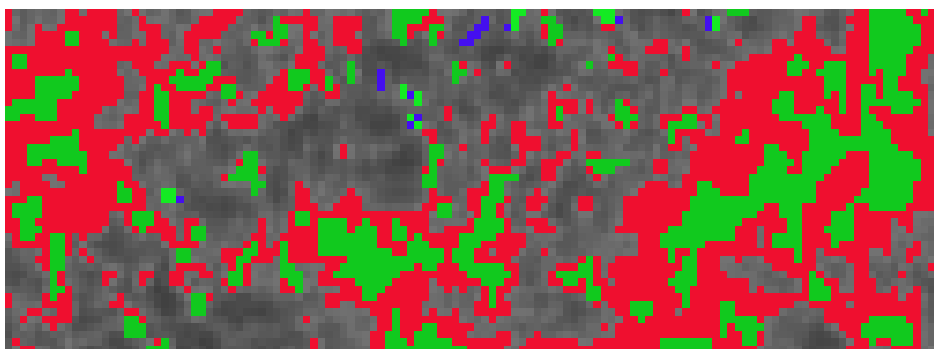
remains the same (Table 4.3).



(a) A number of network pixels determined by us.

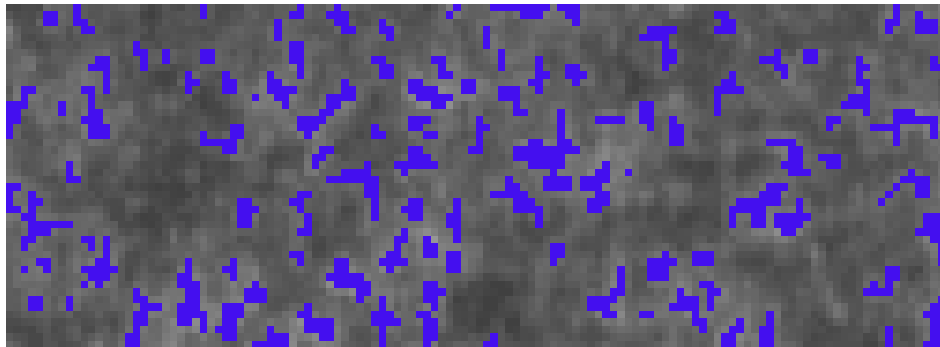


(b) Network detected by the final concentric thresholds.

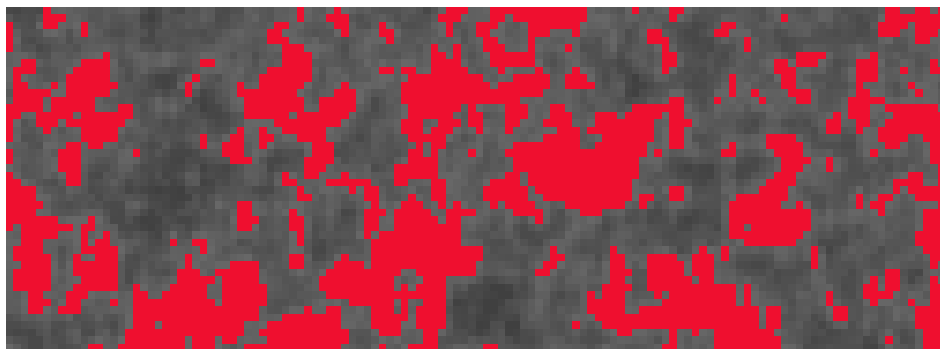


(c) Network detected by us and the algorithm, with the pixels where these overlap shown in green.

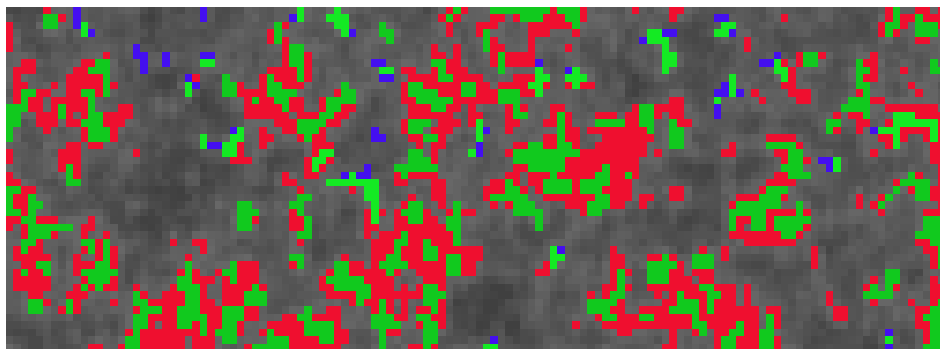
**Figure 4.18:** Test of concentric threshold's effectiveness at the centre of the active test image.



(a) A number of network pixels determined by us.



(b) Network detected by the final concentric thresholds.



(c) Network detected by us and the algorithm, with the pixels where these overlap shown in green.

**Figure 4.19:** Test of concentric threshold's effectiveness at the limb of the active test image.

## 4.2 Morphology Based Detection

Feature detection methods based on the feature morphology have become more commonplace within the sciences as the methods have improved. While they were originally developed for use on binary images they have been extended to grayscale images and even 2D full colour images [27]. While these methods may have become almost ubiquitous they are still rather computationally intensive and very time consuming. They should, however, be immune to many of the issues that the previous methods had when dealing with a varying brightness, as they work solely on the shape of a feature rather than its absolute or relative brightness. To understand the detection algorithms developed in this section there are several mathematical morphology concepts and definitions that must be explained.

In grayscale, 2D morphology images are viewed as functions mapping Euclidean space into  $\mathbb{R} \cup \{\infty, -\infty\}$  with  $\mathbb{R}$  being a real number between  $\infty$  and  $-\infty$ . and the basic morphological operations are *dilation* and *erosion*.

Integral to both of these operations are objects called *structuring elements*. These objects are what the images are dilated or eroded with and so share the same number of dimensions and are also represented by a function. If the structuring element is represented by the function  $b(x)$  then it is defined by Equation 4.1 where  $B$  is a subset of  $E$ .

$$b(x) = \begin{cases} 0, & x \in B, \\ -\infty, & \text{otherwise,} \end{cases} \quad (4.1)$$

With the structuring element thus defined and the image defined as the function  $a(x)$  then the dilation of  $a$  with the structuring element  $b$ ,  $(a \oplus b)$ , is given by Equation 4.2 [28].

$$(a \oplus b)(x) = \sup_{y \in E} [a(y) + b(x - y)] \quad (4.2)$$

This is perhaps more intuitively explained through a visual representation of the process. The structuring element can be viewed as an arbitrary array of 1s and 0s that can take any shape or size. The 1s are defined as *foreground* and the 0s as *background* with the central element known as the *origin*. Figure 4.20 shows three examples of such structuring elements.

The dilation process superimposes one of these structuring elements over every pixel

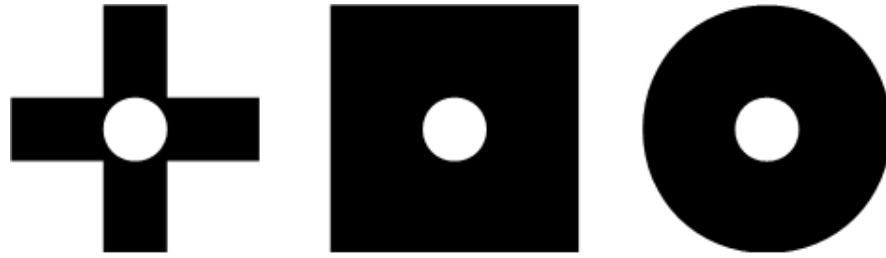


**Figure 4.20:** Three different structuring elements with the foreground regions shown in black and the origin as a small white circle.

in the image to be dilated. The value of the pixel falling within the origin of the structuring element is then changed to the highest found throughout the foreground of the structuring element. What this serves to do is extend the boundaries of any pixels brighter than their neighbourhood, essentially causing any bright features found to grow [27].

Erosion is simply the dual operator to dilation and so causes bright features to shrink rather than grow. If using the same image and structuring element as before then the erosion of  $a(x)$  with  $b(x)$ ,  $(a \ominus b)$ , is given by Equation 4.3.

$$(a \ominus b)(x) = \inf_{y \in B} [a(x + y) - b(y)] \quad (4.3)$$

Along with dilation and erosion the two other fundamental morphological operations are *opening* and *closing*. These are much more simply defined than the previous two operations, as an opening is simply the dilation of an erosion and a closing the erosion of a dilation. Using the same definitions as in Equations 4.2 and 4.3 an opening is denoted as  $(a \circ b)$  and a closing as  $(a \bullet b)$  [29].

Openings are generally used for the removal of noise from an image as they cause small bright features to disappear. A closing on the other hand removes small holes from an image, that is small features darker than their surroundings.

### 4.2.1 Morphological Dilation

A basic morphological technique (top-hat filtering) has already been used in this work (Section 3.2.3) to create a background intensity. A similar technique is used here as part of a more complex algorithm to detect the UV network.

It is already known that a morphological dilation of an image causes bright features to grow out beyond their original boundaries. Of course growing out the bright features in our images would make the network unidentifiable if they are grown too far. There is however a way to use dilation to emphasise the network compared to the background rather than blurring it beyond recognition. The things required for this are a *mask* image containing the original boundaries of the features and a *marker* image that contains the locations of all the features. The mask image is the simplest to obtain, we need an image that contains the original boundaries of the features we wish to detect and of course the original image itself fulfils this. The marker image is not much more difficult to create. As the marker image need only contain some of the pixels from within each feature, as the dilation process will grow these pixels out, we simply subtract a constant value from every pixel in the image and use this as the initial marker image.

The first step of this process is to dilate the marker image and then compare it to the image containing the feature boundary information. A new image is then created in which each pixel has the *minimum* value of those in the two compared images. This means that the brightness from the pixels at the centre of features can spread to adjacent pixels over the many iterations of the dilations *but* it cannot extend beyond the original bounds of the feature due to the minimum taking step. This new image then becomes the marker image and is then dilated and the process repeats until no changes are observed. At this point all the brighter features should have become uniform in intensity, as should all the background pixels, allowing for easy identification of the features.

Like the other detection algorithms there are variations on this algorithm that must be tested and compared to find the most effective. Here we use the same small test sections seen in Figure 4.3 to judge the effectiveness of the method as we develop it.

To begin the detection process we now need the images with feature boundary and

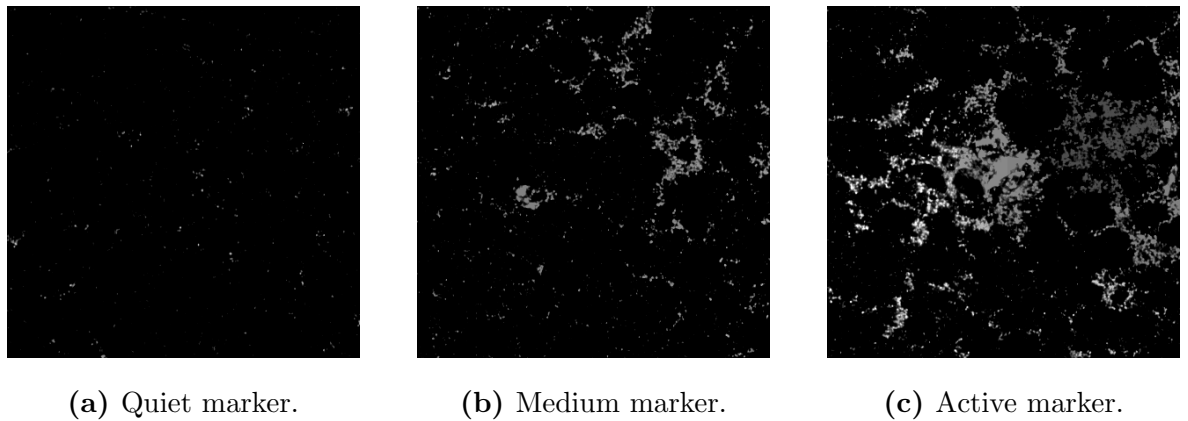
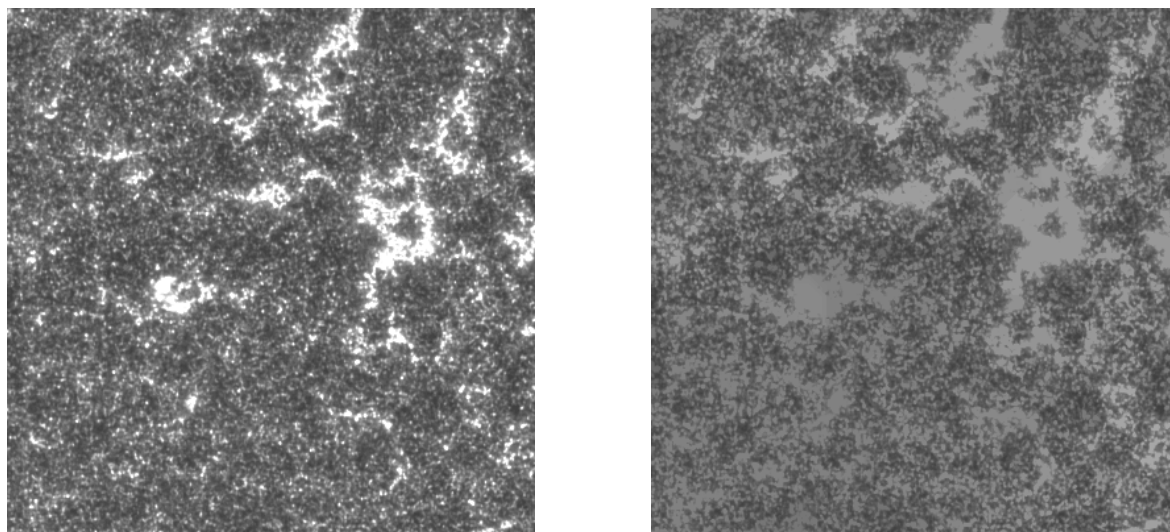


**Figure 4.21:** The marker images for each of the morphological test sections.

position data. The test sections seen in Figure 4.3 are used as the mask images as they obviously include the original boundaries of the features. For the marker image we subtract a constant from the mask. The value of the constant subtracted here was 1.5. We now have the images to be dilated (Figure 4.21).

Given that the dilation requires a structuring element (that can be of any arbitrary shape and size) to function there are many options that need to be explored. We can quickly narrow down an appropriate shape for the structuring element however. It is generally the case that structuring elements that contain straight edges and defined corners are better suited when trying to detect features that have similar properties. Smooth features of an arbitrary shape are best detected using a circular structuring element. The UV network definitely falls into the latter of these categories and so we will use circular structuring elements in our detection algorithms. Further, the structuring element must be similar in size to the features we are attempting to detect. Since the long-term goal is to use this algorithm on 1000s of images without user interference we cannot pick and choose a size of structuring element to best suit each individual image so a compromise must be made. We thus choose a circular structuring element of diameter 30 pixels as this is similar in scale to the majority of the network while not being too small compared to the less common larger active regions.

While the process has already been thoroughly described qualitatively a visual representation aids in understanding the steps. Figure 4.23 shows the marker images for each test section with subsequent images showing the results of dilating with the



(a) The medium activity test section.

(b) The same section after 20 iterations.

**Figure 4.22:** A comparison between the original test image and the results of the morphological processing.

circular structuring element of diameter 30 pixels and then taking the minimum of the two images an increasing number of times.

If we compare the results of this process with the original it was used on (Figure 4.22) it is obvious that the network becomes much clearer. That is, the network starts to become even in colour and all pixels that are not network become black. When this process is complete we will then hopefully be left with a binary image where the entirety of the network is represented by one colour of pixel.

After demonstrating that a structuring element of that size and shape could be used successfully to detect the network the algorithm was then used on the full disc active test image until completion.

Again we need look at the detections by this method in more detail by comparing it to the network defined by us at a pixel level. Figures 4.24 and 4.25 show this comparison.

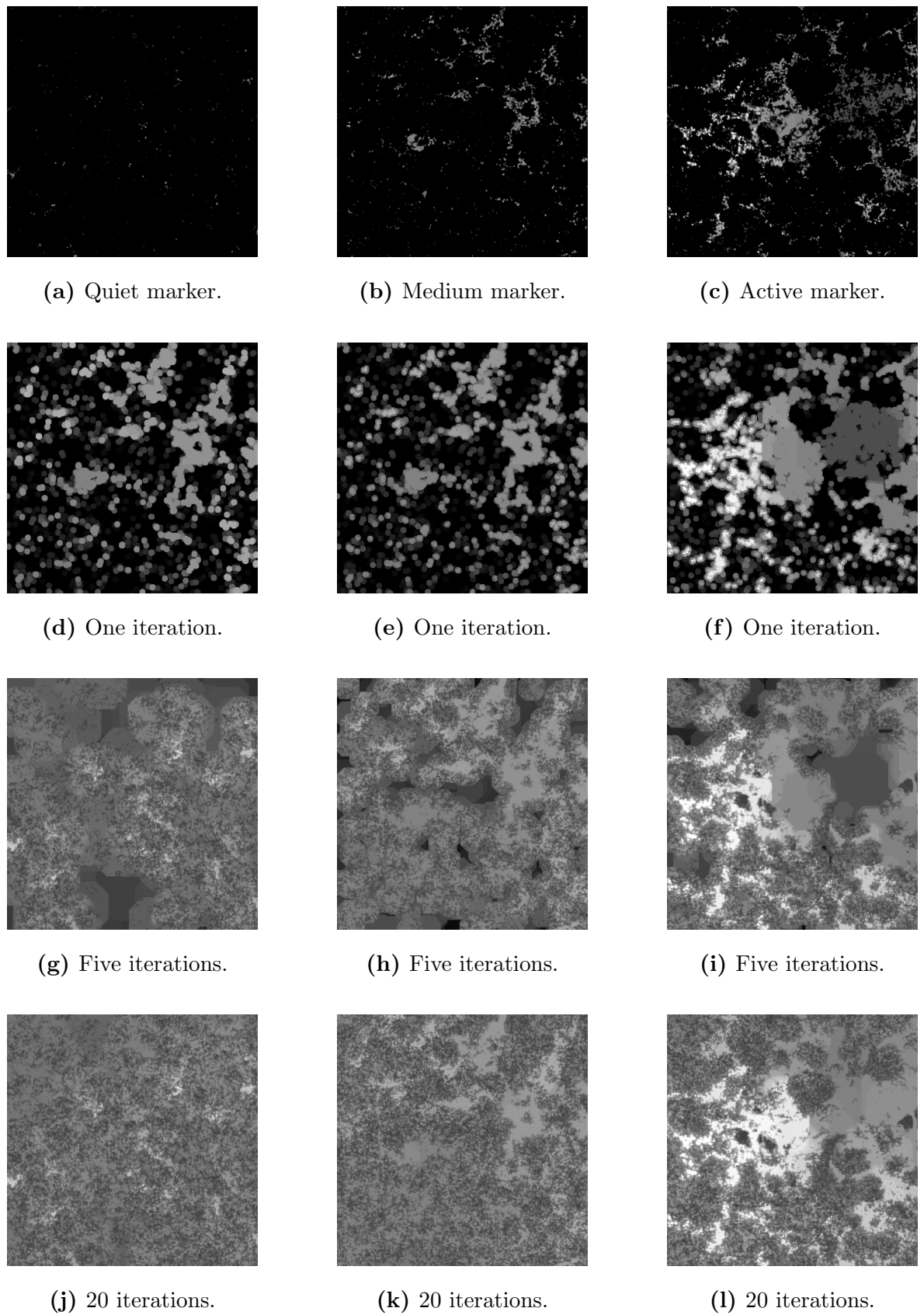
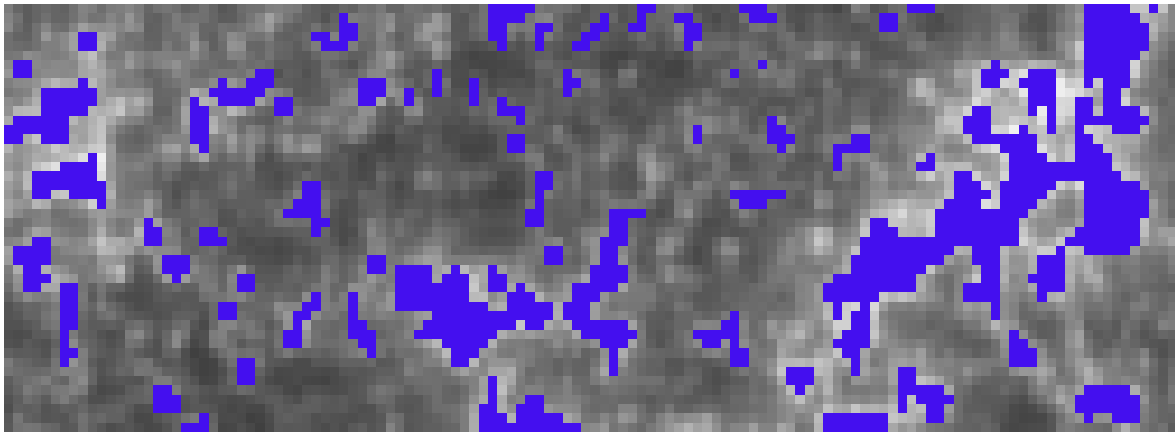
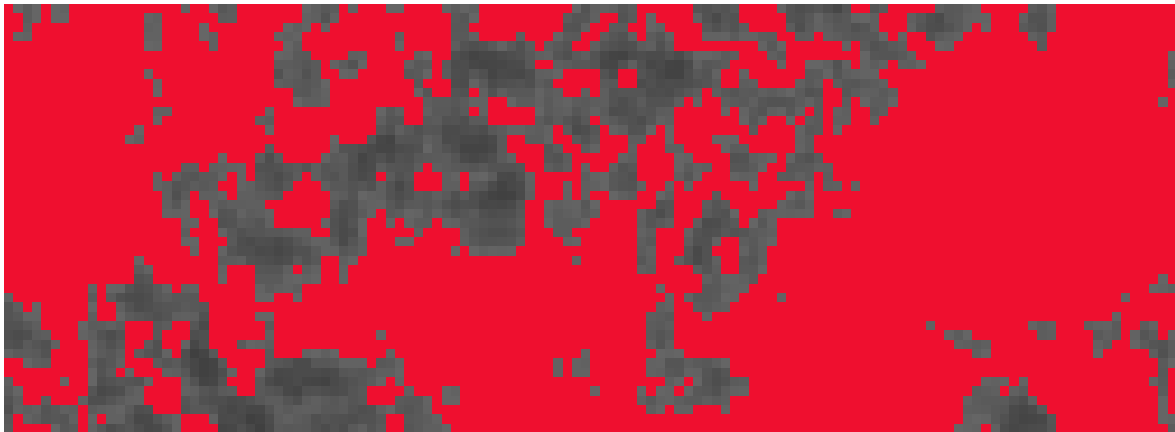


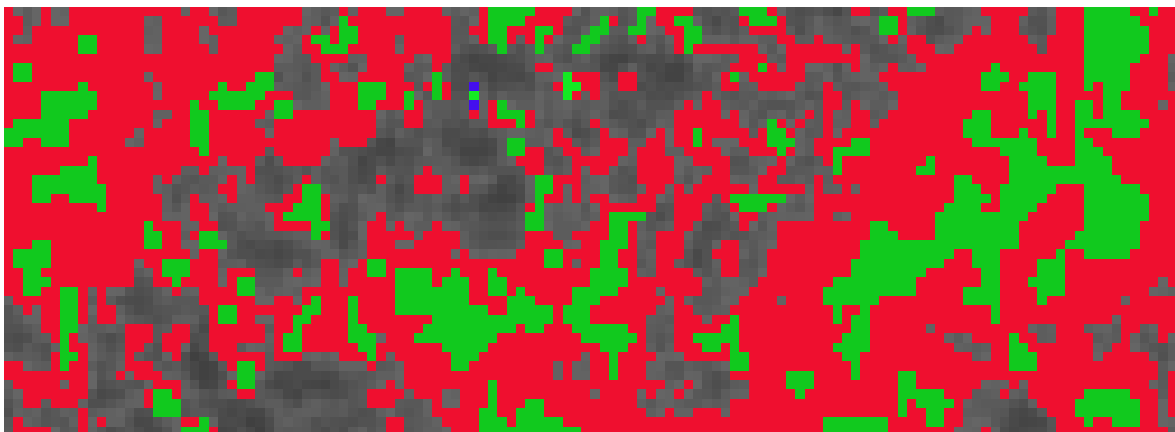
**Figure 4.23:** The results of increasing iterations of the morphological network detection on three test sections.



(a) A number of network pixels determined by us.



(b) Network detected by the final morphological dilation.



(c) Network detected by us and the algorithm, with the pixels where these overlap shown in green.

**Figure 4.24:** Test of morphological opening's effectiveness at the centre of the active test image.

Test Image	Detected Network (%)
Quiet Sun	42.26
Medium Activity Sun	46.58
Active Sun	58.06

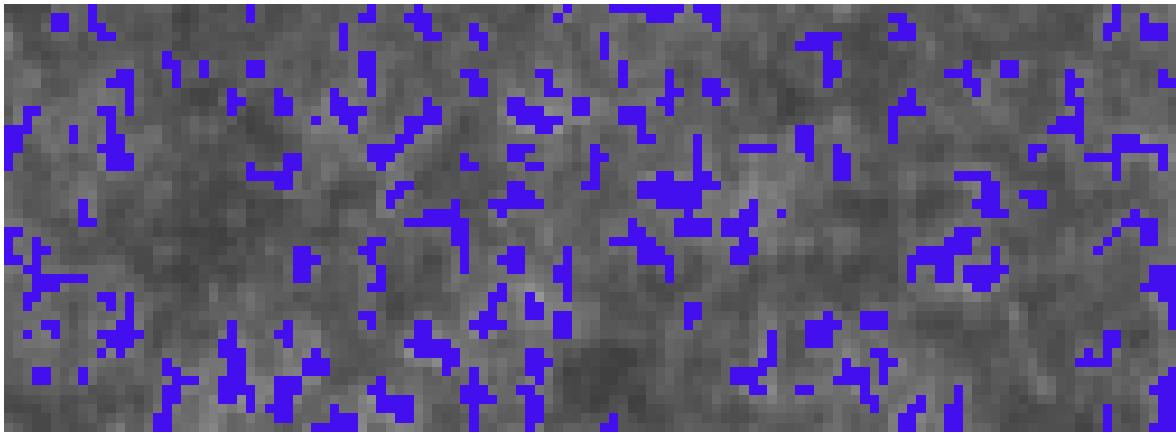
**Table 4.4:** The network detected using the final morphological detection on the three test images.

These figures show that like the previous two methods the morphological opening detects well at the centre and just as the concentric threshold method did it also detects well at the limb.

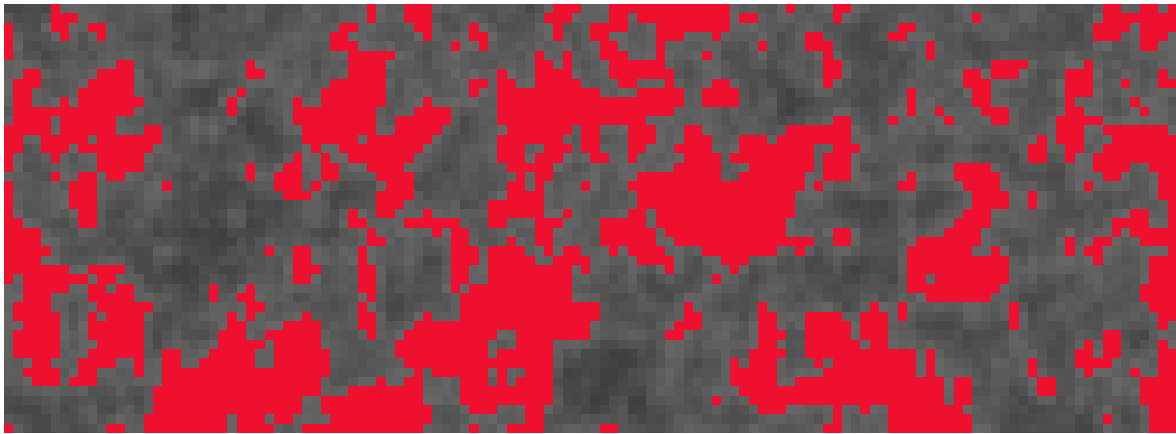
However, it is clear from these two figures that this method detects significantly more than the concentric thresholds did. The detected sections are also much more conjoined than we have previously seen with fewer small individual sections. This is a direct result of this method being based on shape and not brightness.

When this method is applied to the three full disc test images the fraction of the disc found to be network is noticeably higher than previously (Table 4.4).

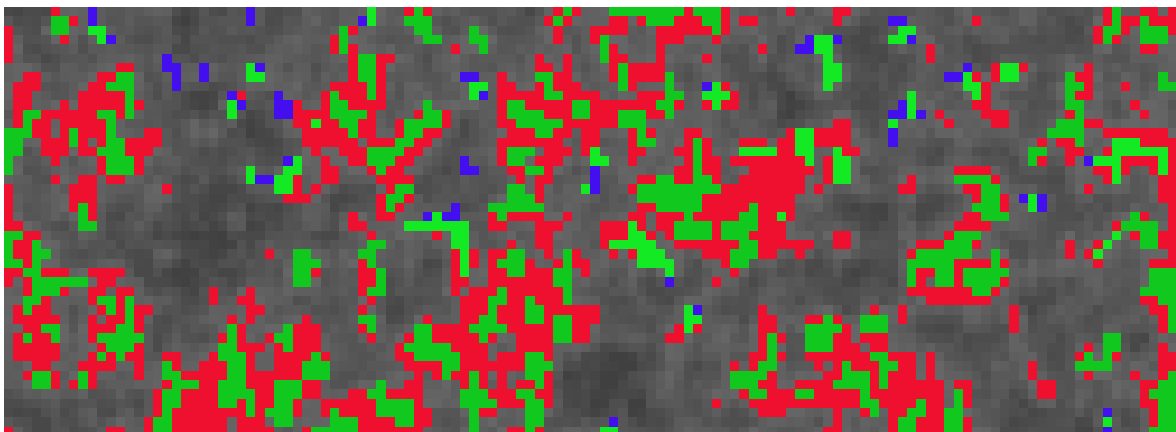
This higher percentage is likely due to the fact that the network does not have sharp and clear boundaries and often seems to blur into the surrounding material. Since this detection method is based on the shape of the network rather than its brightness it likely over detects at these blurred regions.



(a) A number of network pixels determined by us.



(b) Network detected by the final morphological dilation.



(c) Network detected by us and the algorithm, with the pixels where these overlap shown in green.

**Figure 4.25:** Test of morphological opening's effectiveness at the limb of the active test image.

### 4.2.2 Granulometry

The last of the methods used to detect the UV network was another form of morphological analysis, called Granulometry. Here, rather than using a dilation we use a series of openings. Earlier we defined the opening of an image  $a(x)$  with a structuring element  $b(x)$  as  $(a \circ b)$ , that is as the dilation of an erosion. This of course means that this method will also be very time consuming when compared to the brightness based detection methods.

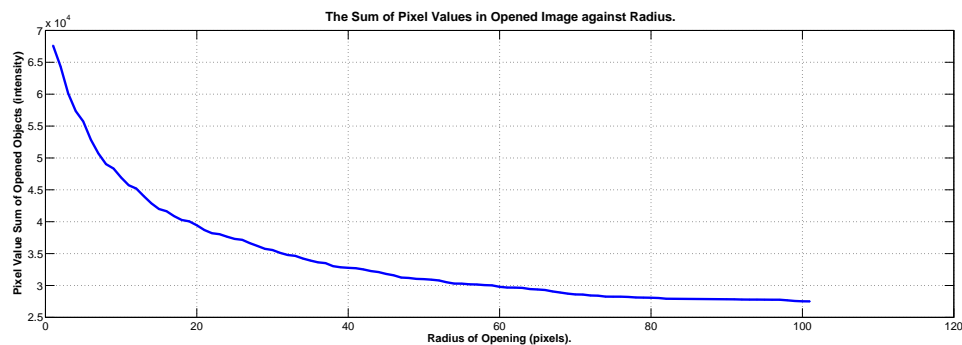
Granulometry determines the size distribution of objects within an image and then detects those objects. It accomplishes this by performing a series of openings of increasing size so that after each opening objects of different sizes are left. This is a rather robust process that has been used previously for feature detection and has frequently shown success [30].

The first step required to use this algorithm for feature detection is the determination of the scales at which objects appear. This is done by performing a series of openings of increasing size and calculating the remaining intensity surface area, that is the sum of the remaining pixel values in the image.

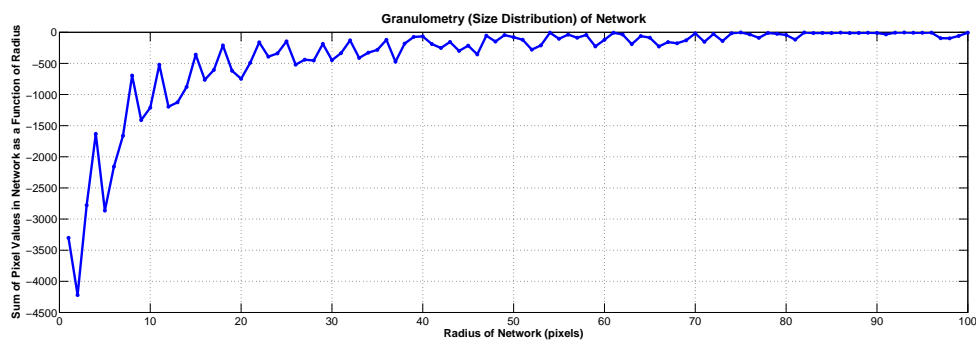
When this sum of intensity values is plotted against the opening at which it was calculated a decreasing trend should be observed. If there is a sharp increase in the gradient of this trend between any two openings then that is a suggestion there are objects present of that size. To more easily identify these sharp drops one need only take the derivative of the intensity area and identify the minima of the resulting plot.

As this is another morphological technique we use the smaller test sections created earlier (Figure 4.3) to limit the computing time during preliminary tests. Using the quiet section test image we perform the series of openings required and the subsequent differentiation to identify possible scales for features. These plots are shown in Figure 4.26.

There are a large number of minima present in Figure 4.26 suggesting that there are objects existing on many scales. The two most prominent minima occur at openings of radius 2 and 5 pixels. If we examine the objects relating to these openings we find the detected ‘features’. These are shown in Figure 4.27. It is clear from this that this method does not work at all as well as was hoped. It certainly detects *something*



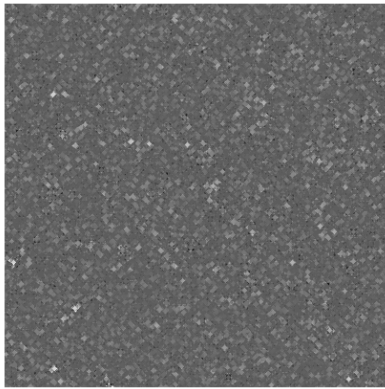
(a) The sum of the remaining intensity values after a series of openings against the radius of said openings.



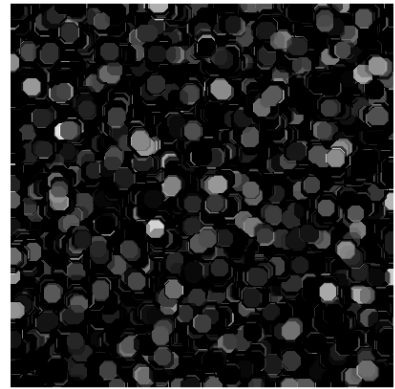
(b) The differential of the surface intensity values against the radius of the openings.

**Figure 4.26:** The two preliminary plots from the use of granulometry.

and the location of the brighter objects within the images shown in Figure 4.27 does vaguely align with the location of the UV network in the test image. It seems that this method would possibly work well at detecting objects that were all of a similar size and shape but struggles when the features vary as much as the UV network does. All this means is that this morphological granulometry algorithm is not a feasible candidate for the detection of the UV network.



(a) Opening features at a radius of 2 pixels.



(b) Opening features at a radius of 9 pixels.

**Figure 4.27:** The resultant features at two scales from a granulometry based network detection.

### 4.3 Comparison of Methods

The network detection algorithm chosen will be applied to several thousand images. These images will all be of roughly the same average brightness but the network and presence of large active regions will vary over the dataset. Thus the selected method needs to be capable of detecting the network equally well across all levels of solar activity. Also, just as we had to consider it for the background correction, the time taken for each method is an important factor.

The behaviour of the network, or at least how its position and covering percentage evolves over time, is not well understood. This means there are no known definitive qualities we would expect to see that we can compare to our findings and thus judge them, though some similar work has been done by others in this area (admittedly not at the wavelength we have examined here). This leaves us with the method that has been used so far throughout this work, a combination of whether the detection appears correct and on much smaller scales how it compares to pixels we have designated to be network.

Clearly we can rule out the use of granulometry as a detection method. Further, the use of a basic threshold must also be ruled out. While it was capable of detecting the network well, at points a static-valued threshold was just incapable of dealing with even small variations in pixel value across the disc, as was seen by its failure to detect network at the solar limb. However given its simplicity this method was also the quickest of the three candidates left (Table 4.5).

This leaves the concentric thresholds and the morphological dilation as candidates for the most suitable detection methods. Both of these adequately counter the issues with the basic threshold, being able to detect the network in darker parts of the image. It could be argued that the dilation detection method is more reliable than the concentric thresholds as it based *solely* on the shape of the network. However, we must consider the length of time each method takes to run. Again looking at Table 4.5 we can see that the time taken for the morphological dilation detection is two whole orders of magnitude greater than that of the concentric thresholds.

Such a large time for the completion of the dilation detection algorithm is prohibitive, and so the use of concentric thresholds is deemed the most suitable. Further, it can

Method	Average Time Taken (s)
Basic Threshold	0.65
Concentric Threshold	1.42
Morphology	296.57

**Table 4.5:** The time taken for each UV network detection method.

easily be argued that while the morphological detection works equally well across the whole disc it slightly over-detects across the whole disc too. Thus concentric thresholds will be used on the thousands of images analysed in the upcoming chapter to investigate the behaviour of the solar UV network.

We have successfully developed a method to detect the network over several years worth of UV observations, though it is possible the network detected is systematically over or under estimated due to the somewhat subjective nature of our detection method. Such an error being systematic across all detections however means that we can investigate the *behaviour* of the UV network over the life time of the mission.

# Chapter 5

## Behaviour of the Network

As detailed thoroughly in the previous chapter a method to detect the UV network was successfully developed. There are obvious issues with the evaluation of such a method and thus its ability to confidently estimate the absolute network covering percentage for an individual image. However, given that the same method can be applied to multiple images over the lifetime of the SDO mission it can be used to systematically examine the relative behaviour of the network. Further, we can also compare the relative variability of the UV network to other measures of solar variability.

### 5.1 Temporal Behaviour

The first and most obvious examination of the network's behaviour is to examine its variation, if indeed there is any, over time. Due to the high cadence of the AIA imaging system the behaviour of the UV network can be examined in great detail over short time periods but the lifetime of the mission makes any long term analysis difficult as the data only goes back five years.

#### 5.1.1 Short Scale

With the frequently sampled SDO observations, we can examine the short time-scale behaviour of the network at a relatively high cadence.

December 2014 was chosen as the month to be examined, we analysed 12 images a day every 2 hours beginning at 1AM on the 1st of December up until 11PM on the 31st.

This amounts to 372 images analysed, a process that took 2492 seconds to complete. Figure 5.1 shows the results of this analysis.

What is immediately obvious from Figure 5.1 is that the percentage covering of

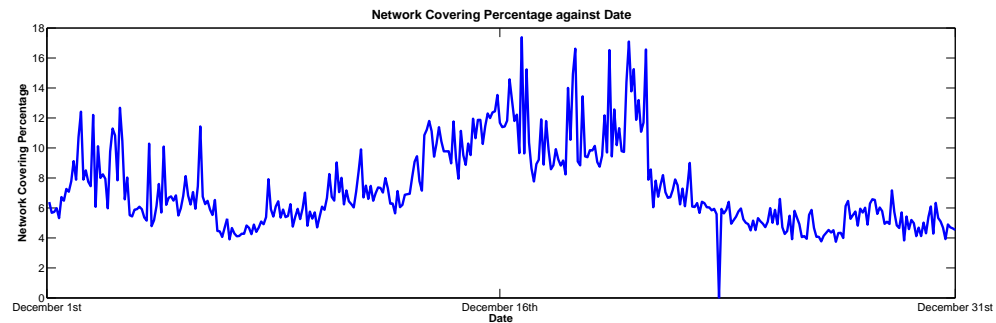


**Figure 5.1:** The covering percentage of the UV network throughout December 2014.

the network detected here is significantly less than was detected in the test images earlier (4.3. There we were seeing a covering percentage of 30-45% where as here the percentage fluctuates over the range of 5-20%. Aside from this very large disparity in the covering percentage range (which is discussed briefly in the following section and detailed thoroughly in Section 5.2.1) the covering percentages detected here frequently fluctuate by a factor of two with a clear and pronounced increase by a factor of 3 around the middle of the month. One month alone is not enough to begin to draw conclusions from the data and the so the range investigated is extended. We repeat the previous examination for the entirety of 2014.

For the investigation over the course of 2014 we reduce the cadence at which we sample to save both time and storage. We now sample three images per day; at midnight, 8AM and 4PM. Though a reduced cadence this is still a comprehensive sampling over the course of a year. Figure 5.2 shows that the mid monthly increase in covering percentage of the network observed for December is not an isolated phenomenon but observable for every month of 2014.

This almost monthly feature is easily explained if we consider it to be related to the rotation of the Sun. The equatorial regions of the Sun rotate at a period of about 26 days with this increasing to 36 at the poles [31]. As the Sun rotates so to do the large

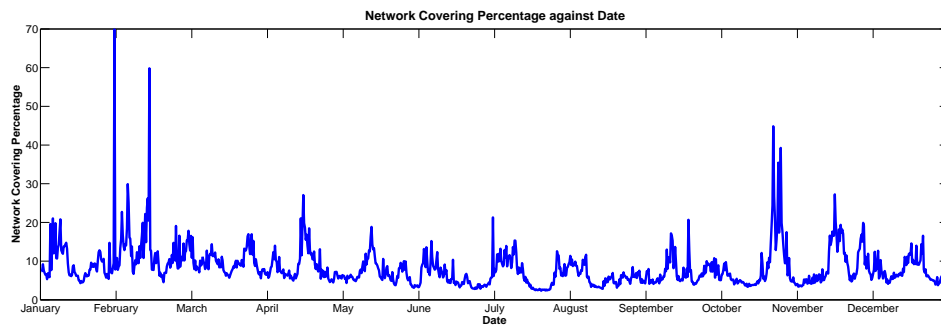


**Figure 5.2:** The covering percentage of the UV network throughout 2014.

active regions and sunspots on solar surface. These large regions are detected as part of our network detection algorithm and thus as these appear on one limb of the Sun and rotate off the other we can expect our detected network to similarly increase and fall off.

### 5.1.2 Long Scale

The longest scale on which we can examine the behaviour of the UV network is from the current date back to the launch of the SDO mission in 2010. In astronomical terms this is far from enough to make any significant long term analysis but analysis on such a scale is far from meaningless as it is still a significant portion of a solar cycle - during which we expect to see the contributions of active regions changing. Image data at these wavelengths does exist from before the launch of SDO but either the resolution of these older images is not sufficient for this work or the data is not ‘full-Sun’. We thus restrict ourselves to the data available from SDO.

To examine the behaviour of the network at this time-scale we simply repeat what was done earlier for a month and a years worth of data. The frequency at which we sample the images must be reduced yet again to make our analysis feasible. We choose to investigate the period spanning from January 2011 up until Dec 2014 - taking one image a day, at 1AM, giving us a total of 1440 images.

We can see in Figure 5.3 the results of this examination. First, it is encouraging to see that the apparently monthly variations in the covering percentage that were observed earlier are still present here, from 2012 onwards at least.

We also here gain some insight into the low network covering observed earlier. It can be seen that the covering fraction post January 2012 is consistently around 10% but much larger for the period preceding this. Before this the detected network is much more in line with the percentages found using the test images. All of the test images were taken from this time period (all coming from the first half of 2011), meaning of course that perhaps the problem is with these images and not the images post January 2012. However, we had come to the conclusion that the percentages detected using the test images were reasonable, suggesting that the issue is in fact with the majority of images tested. This of course is not a reassuring conclusion, though it does have a plausible explanation (5.2.1).

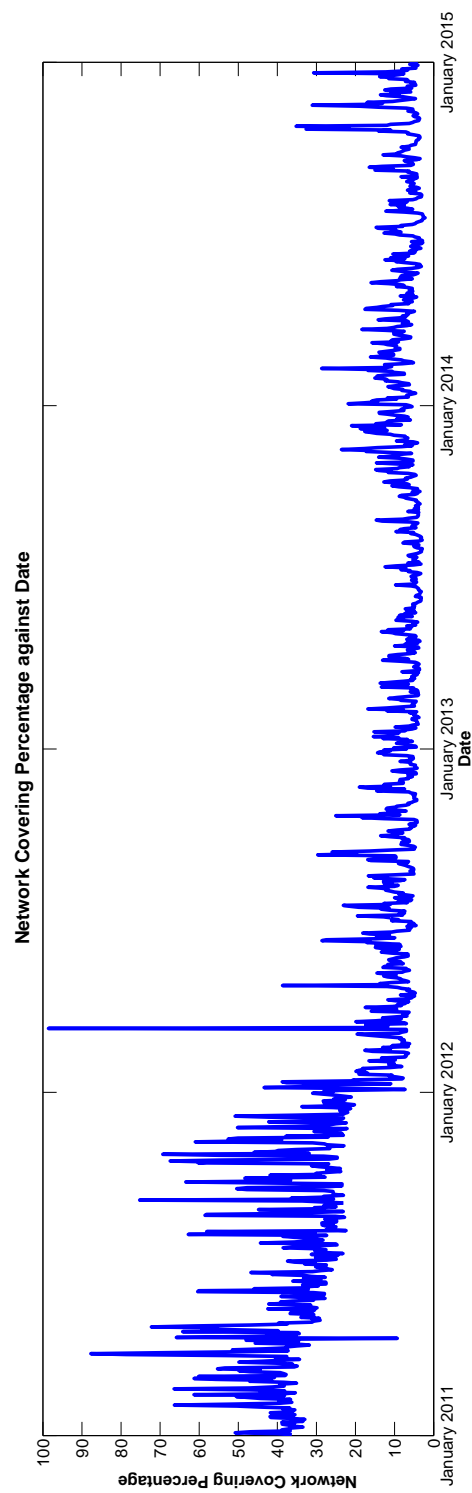


**Figure 5.3:** The covering percentage of the UV network from January 2011 to January 2015.

## 5.2 Comparison with other measures of Solar Variability

We now know how the solar UV network varies over short timescales but there is still the rather large unsolved issue of its sudden, and severe, drop in covering percentage in January 2012. Examining the relationship between the covering percentage and other measures of solar variability will perhaps offer insight as to the cause of this disparity. Further, such examinations could also serve as a check on the effectiveness of our detection algorithm and even offer new information as to the nature of the network.

### 5.2.1 Brightness

#### 5.2.1.1 Comparison with Brightness

Earlier, in Section 2.2.0.2, we plotted the average brightness of each image examined over the last four years of the SDO mission. Here we plot that average brightness together with the network covering percentage for the same time period. It is already known that the presence of the network increases the Total Solar Irradiance, and hence the brightness, of the Sun and so it should follow that there would be a correlation present between the average brightness and the network coverage.

If we momentarily ignore the large drop observed at the start of 2012 that we earlier concluded could be attributed to infrequent flatfielding then we can see that a correlation is indeed present (Figure 5.4). Throughout the data post 2012 we know that there should be nothing affecting the average image brightness that is not physical (the exposure time is relatively constant throughout the mission and flatfields were taken at appropriate intervals after 2012). Thus when we observe that small fluctuations in the brightness coincide with spikes in the covering percentage we can conclude that it is the network covering percentage causing these fluctuations.

Returning to the large drop present at the start of 2012 it makes sense that if there was a drop in the brightness of every image there would be a drop in the network covering percentage given that the detection algorithm that was settled upon is dependent on the brightness of the pixels. Since the algorithm was perfected using test images from the period before the drop in brightness it severely under-detects the network in the

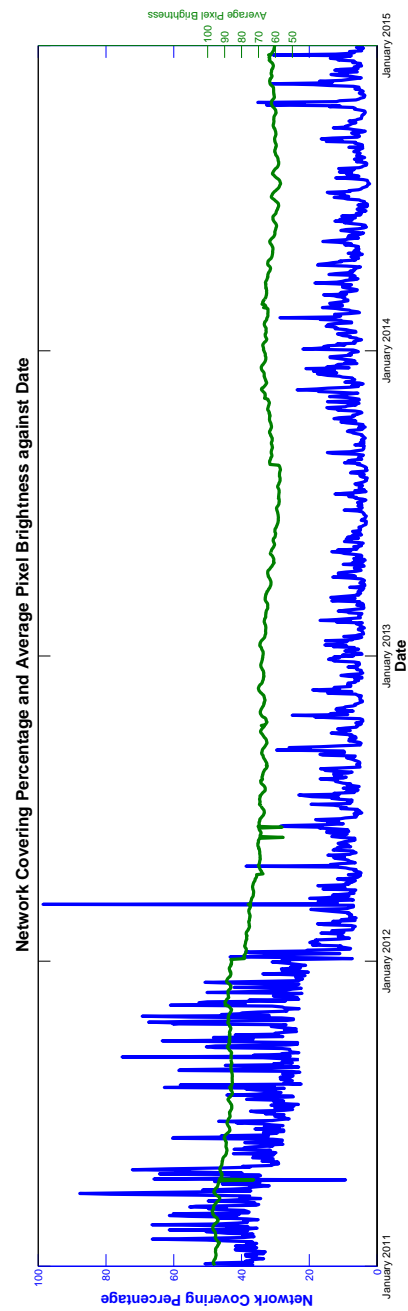


**Figure 5.4:** The covering percentage of the UV network and the average brightness of each image from January 2011 to January 2015

darker images.

The plus side to this is that the issue is seen to be a problem with the data rather than our detection algorithm. Since we know that the detection algorithm works well for the brighter images, and that the drop in brightness is very similar to the drop in the network detected, we can simply apply an appropriate correction to all the calculated network coverage values that are affected by this issue.

### 5.2.1.2 Correction of Network Covering Percentage

An appropriate correction must be applied to the network covering percentage so that we can gain a true understanding of its temporal behaviour. We understand now that the problem encountered is a result of the application, or lack thereof, of flatfields. Given that flatfields result in a change in the response of each pixel the correction applied must be multiplicative in nature. Before January 2012 we observed network covering percentages in the range of 30% while after they fell to around 10%. As such an appropriate correction would be to increase the affected covering percentages by a factor of 3. Although this is an ad hoc correction it is motivated by a known change in the observing conditions so we expect that the results are still adequate for an examination in comparison to other features.

The results of this correction can be seen in Figure 5.5.

The network covering percentage is now much more consistent over the 4 year period. A further comparison between this now corrected network covering percentage and the average image brightness (5.6) clarifies the correlation between the two. There is the same roughly downward trend apparent throughout 2012 and much of 2013 with an increase seen in both brightness and network covering fraction towards the end of 2013 and in the beginning of 2014.

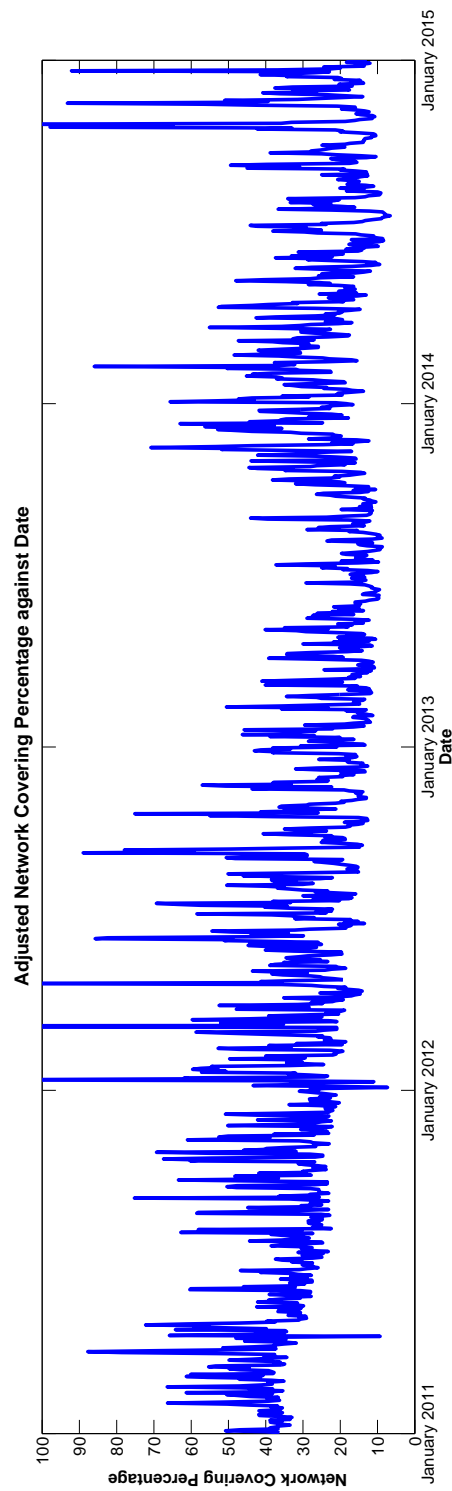


**Figure 5.5:** The covering percentage of the UV network from January 2011 to January 2015 with a correction applied.

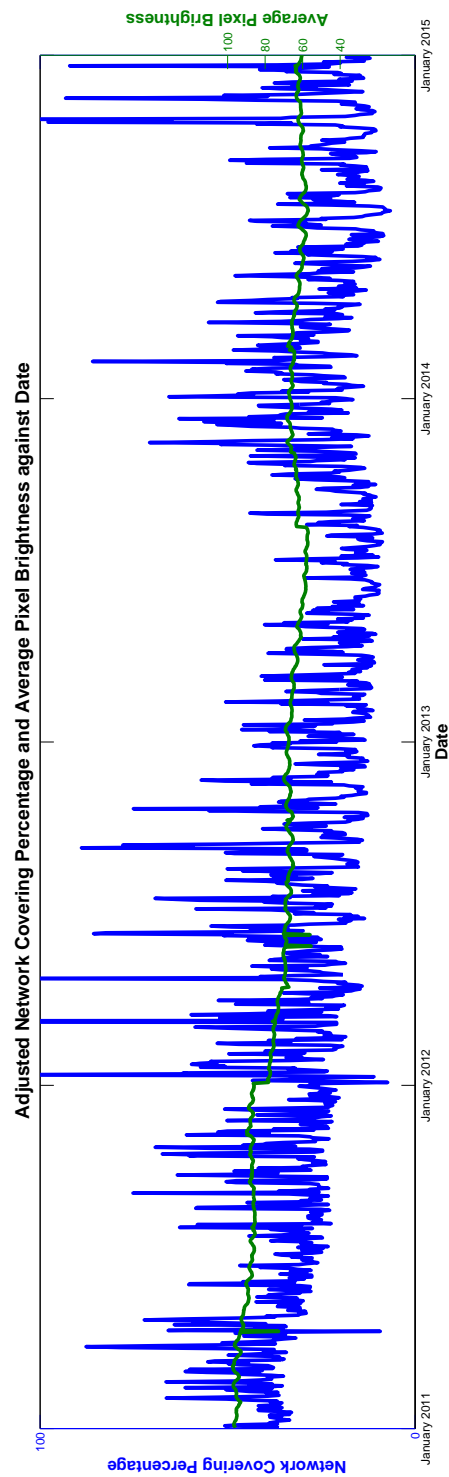


**Figure 5.6:** The corrected covering percentage of the UV network and the average image brightness from January 2011 to January 2015.

### 5.2.2 F10.7 Flux

The F10.7 Flux is, as it sounds, simply a measure of the radio flux emitted by the Sun at a wavelength of 10.7cm (or 2800MHz). It generally ranges from 50 solar flux units (s.f.u) to as high as 500 s.f.u and above, where 1 s.f.u is equal to  $10^4$ Jy. The F10.7 flux arises high in the chromosphere and into the corona, with coronal contributions through bremsstrahlung and gyroresonance mechanisms [32]. It is one of the longest records of solar variability, and one of the most easily recorded, with daily records dating back to 1947 [33].

It is frequently used in the reconstructions of solar EUV flux and is known to correlate well with TSI and sunspots [34] [35] and as such we would expect at least a small level of correlation between the F10.7 flux and our detected network.

Using the F10.7 measurements provided by Leif Svalgaard [36] we plot the F10.7 flux and corrected network covering percentage over the January 2011 to January 2015 period. What we observe is that there is indeed a correlation between the two. The large scale trends over the 4 year period line up very well and even the shorter scale fluctuations on the periods of months appear to correlate. This correlation lends a certain amount of credence to our detection algorithm in that it shows that the relative behaviour of our detected network is as expected.

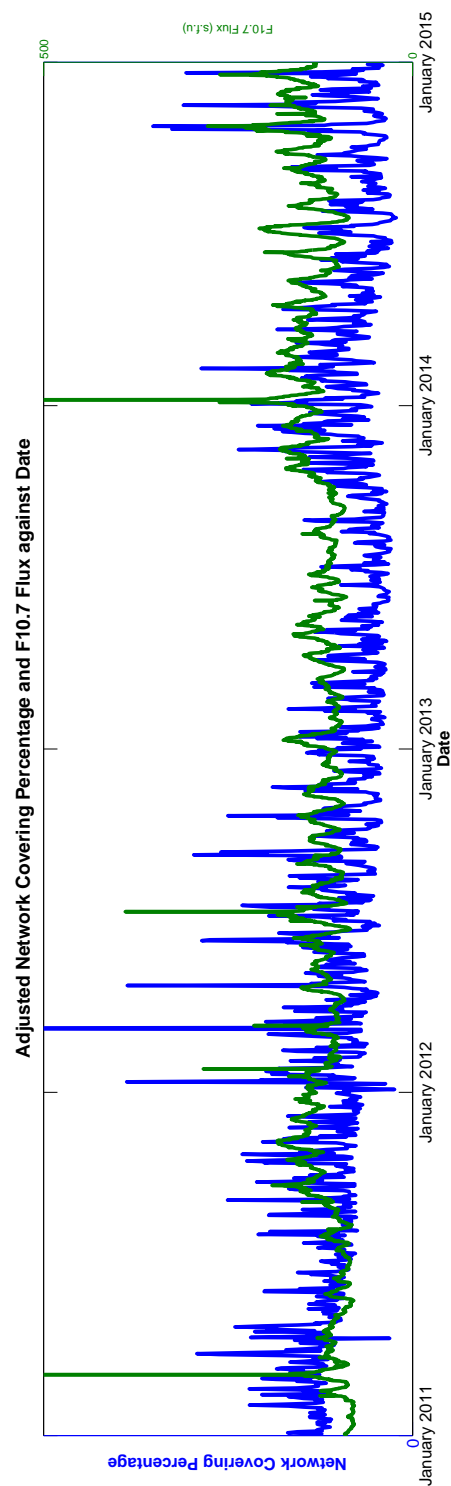


**Figure 5.7:** The corrected covering percentage of the UV network and the F10.7 flux from January 2011 to January 2015.

## 5.3 Behaviour of the Quiet Sun

While the previous sections deal with the behaviour of the network and its relations with other measures of solar variability they do highlight a small issue. Some of the behaviours observed, such as the monthly fluctuation, and even the correlations with the F10.7 flux could be wholly attributed to active regions. That is, they may not be down to the more distributed network that we find between granulation cells but instead the large active regions often present in bands north and south of the equator of the Sun.

This section deals with the attempt to either remove these large active regions from our detection algorithm or otherwise account for them. This way it is hoped we could get a *truer* representation of the quiet Sun's network behaviour.

### 5.3.1 Removal of Active Regions

The ideal approach here would be to remove the active regions completely from our detection methods so that the covering percentage we calculate only corresponds to the 'true' quiet Sun network. We describe below the two methods used to try and remove the large active regions from our detections. It should be noted that for these two methods a different test image was used, seen in Figure 5.8.

This image was specifically chosen as it has large distinct active regions and (highlighted by the two red boxes) clear areas of quiet Sun should the removal of said active regions be unsuccessful.

#### 5.3.1.1 Singular Spectrum Analysis

Singular Spectrum Analysis (SSA hereafter) is a nonparametric spectral estimation method that was originally developed for use with time series data. Its aim within time series analysis was the decomposition of a time series into several meaningful components [37]. It is important to note here that the use of the word 'spectrum' relates to the 'spectrum' of eigenvalues used in the decomposition method.

Since its original inception the applications of the basic SSA methodology have been extended into many areas and it is now possible to use a more advanced version of it

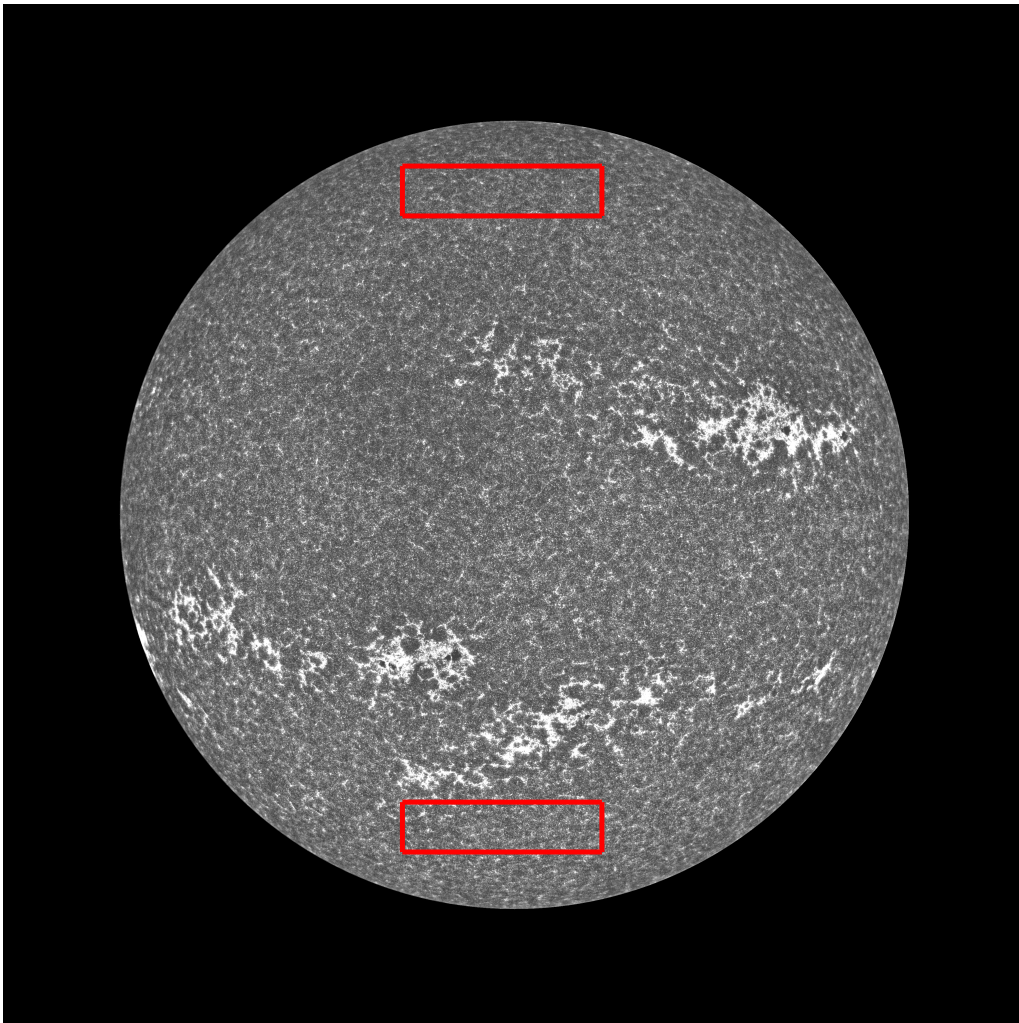


**Figure 5.8:** The test image used for active region removal with two quiet areas shown in red.

for large scale feature extraction, hence the motivation for its use here [38].

The SSA methodology is perhaps best explained using the most basic example, a simple time series  $T_A$ . If  $T_A = (t_1, \dots, t_A)$  this can be decomposed into several components, where each component represents either a trend, periodic component or noise. The technique itself has two stages, a decomposition followed by a reconstruction, each of which consists of two further steps themselves. The steps are as follows: for decomposition; ‘Embedding’ and ‘Singular value decomposition’, and for reconstruction; ‘Grouping’ and ‘Diagonal averaging’.

The embedding stage transfers the one dimensional time series  $T_A$  into the multi-

dimensional series  $B_1, \dots, B_X$  with the vectors  $B_i = (t_i, \dots, t_{i+L-1})$ . Here  $X = T - L + 1$ . The parameter  $L$  introduced here is the only parameter throughout the entire SSA process that needs to be predetermined. It is called the ‘window length’ and is simply the scale limit at which the periodicity in the components is searched. This step creates a ‘trajectory matrix’  $B = [B_1, \dots, B_X] = (b_{ij})_{i,j=1}^{L,X}$  which is operated upon throughout the subsequent steps.

The next step, singular value decomposition (SVD), takes the trajectory matrix created earlier and first computes a new matrix  $S$  such that  $S = BB^T$ . From this we take the eigenvalues,  $\lambda_1, \dots, \lambda_L$ , in decreasing order of magnitude so that  $(\lambda_1 \geq \dots \geq \lambda_L \geq 0)$ , and the eigenvectors corresponding to these eigenvalues are denoted by  $U_1, \dots, U_L$ . We then set  $d = \text{rank}B = \max i$ , such that  $\lambda_i > 0$ . If we then denote  $V_i = B^T U_i / \sqrt{\lambda_i}$  the SVD of the trajectory matrix  $B$  can be written as  $B = B_1 + \dots + B_d$  with  $B_i = \sqrt{\lambda_i} U_i V_i^T$ . With the decomposition now completed we move on to the complementary SSA stage - reconstruction. We begin this by creating a series of subsets  $I_1, \dots, I_m$  where  $m$  is the number of subsets created, which in this case corresponds to the number of components we wish to decompose the original time series to. If we set  $I = i_1, \dots, i_n$  then the matrix  $B_I$  corresponding to the group  $I$  is  $B_I = B_{i_1} + \dots + B_{i_n}$ . The final stage of the SSA process now follows. Each of these matrices  $I$  is diagonally averaged and the result of this averaging is an additive component of the original time series. Each of these components can either then be viewed individually to analyse any periodic behaviour or reconstructed into the original series.

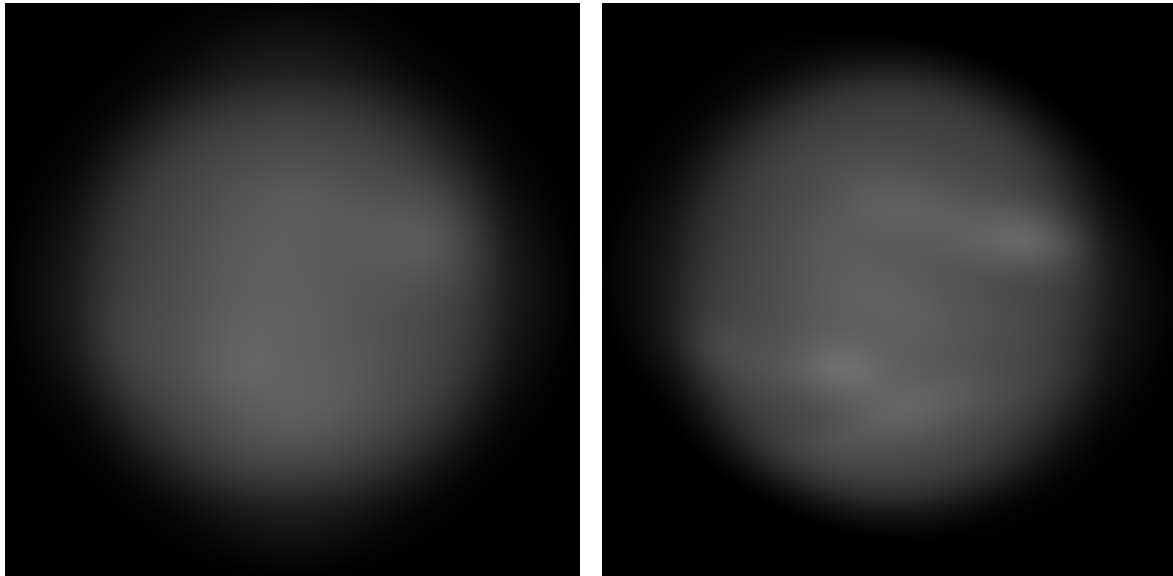
The SSA technique is far from trivial but can be easily adapted from its use in time series to be used in images. The only change between the two methods is that the window length  $L$  explained earlier now becomes a box with a width and height. The resultant individual components from using the SSA technique on an image are thus images of the same size of the original but, rather than each representing periodic patterns in a time series, they now show features present in the original image over a span of scales.

We (with the assistance of Dr. Jaime Zabalza from the University of Strathclyde) similarly extended the basic SSA procedure to a 2D version to be used here.

The effects of using SSA on the active Sun test image, with a window size of 500 by

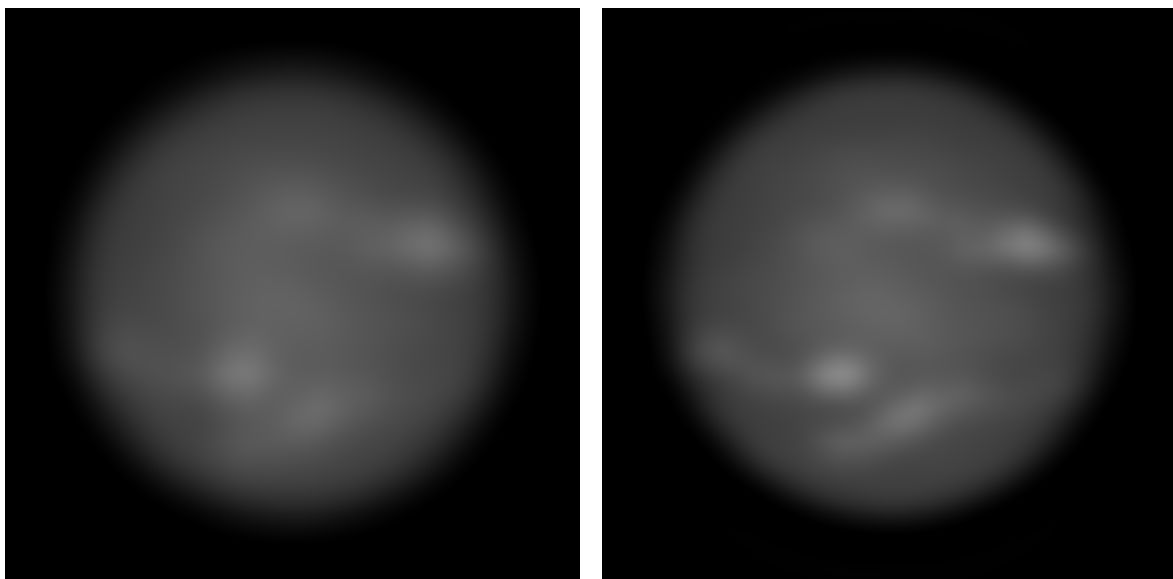
500 pixels and decomposing into 4 components is shown in Figure 5.9.

In general the use of SSA results in simply very blurred versions of the original image,



(a) The first SSA component.

(b) The second SSA component.



(c) The third SSA component.

(d) The fourth SSA component.

**Figure 5.9:** The resultant components from using SSA on the active Sun test image.

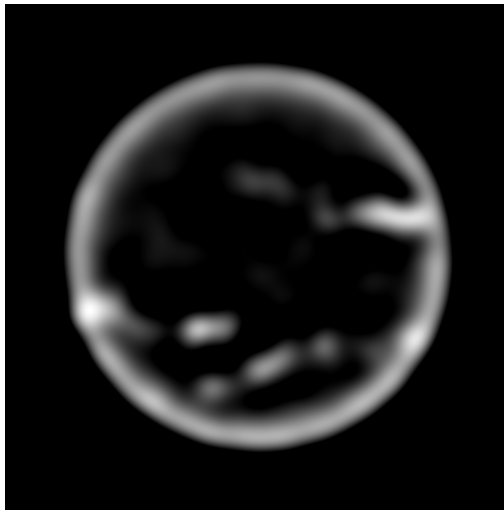
but hopefully with different features appearing in the different components. Figure

5.9 shows that the first SSA component approximates the average brightness of the full disc with no clearly visible features. This of course is not particularly helpful here. When we look at the second through fourth components however (Figure 5.9) brighter features begin to stand out from the background, though they are clearest in the fourth component. If we compare these to the test image used (5.8) it is clear that these brighter blurred sections represent the large active regions present as was hoped. While the large active regions found in this particular image are visible in the SSA components they are not clearly defined and distinct from the background. The lack of a clear edge on the detected active regions in Figure 5.9 means that they cannot adequately be removed from a full disc image to leave the quiet Sun network. This failing may be due to both the arbitrary shape and size of the solar features. This shortcoming would be by itself enough to mark this method unsuitable for the hoped purpose but it is also extremely computationally intensive. Attempting the SSA procedure on the full resolution 4096 by 4096 pixel image takes several days for each individual image, clearly a prohibitive amount of time. Given that we are trying to isolate large features here we can reduce the resolution of the images without worrying about the fine scale network but even with the images reduced to 10% of their original size the process takes at least an hour.

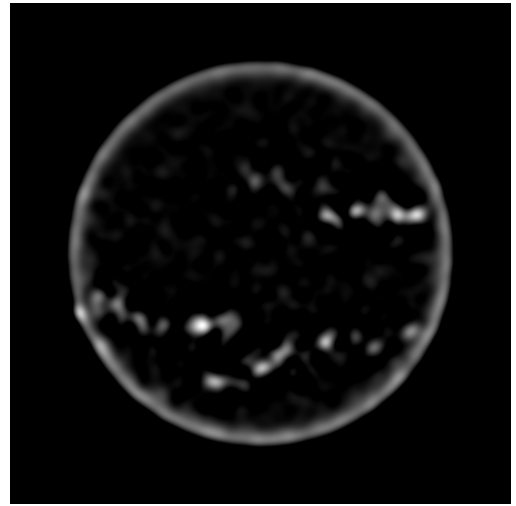
### 5.3.1.2 Increasing Gaussian Filters

The use of gaussian filters is significantly simpler than the SSA method described in the previous section, but the output is very similar. We use the same process we used earlier in Section 3.2.2 to create a background though with a few changes here.

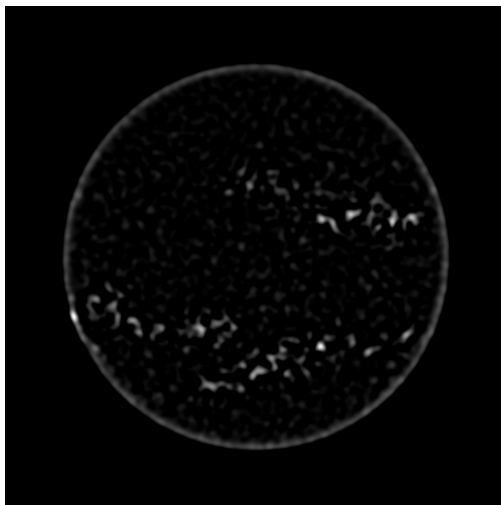
As we already know convolving an image with a gaussian filter blurs the image, and the amount by which it is blurred is determined by the size of the filter used in the convolution. The theory here is that we could use ever-increasing filter sizes to blur the image to greater and greater extents and subtracting these blurrings from one another would leave behind the features present at the scale of those blurrings. For example, if we performed a series of 10 convolutions with 10 differently sized filters, resulting in ten different images blurred by different amounts, and then subtracted the 9th image from the tenth we should be left with an image that has only the features present at the tenth scale. We use that concept here to try and isolate the large active regions, using 4 filters of increasing size. Figure 5.10 shows the resultant images after subtracting the first filtered image from the second; the second from the third and so forth. The resultant images shown in Figure 5.10 are very similar to those created by the SSA and would lead to similar problems when trying to remove them. The active regions have indeed been highlighted but once again their boundaries are not sharp and clear; we have obtained an approximate indication of the active regions locations rather than strict boundaries which can be used to remove them. The bonus to this method, compared to the use of SSA at least, though is that it is a relatively quick process, taking no more than a minute per image.



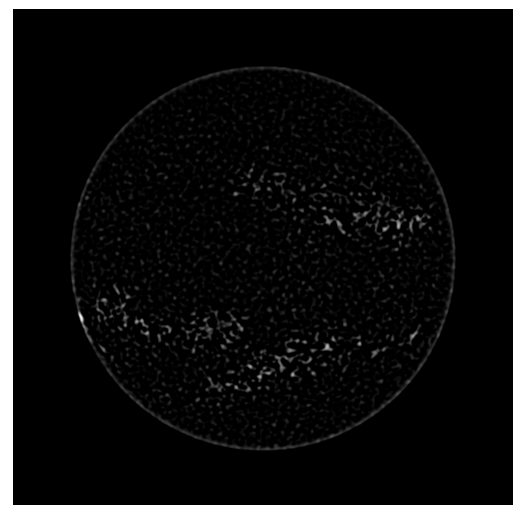
(a) Active regions detected at a scale of 100 pixels.



(b) Active regions detected at a scale of 70 pixels.



(c) Active regions detected at a scale of 40 pixels.



(d) Active regions detected at a scale of 10 pixels.

**Figure 5.10:** The resultant images from using a series of increasing gaussian filters to detect active regions.

### 5.3.2 Behaviour of ‘Quiet’ Areas

Given that the complex method of removing the active regions detailed in the previous section was rather unsuccessful a much simpler, though less comprehensive method, is developed here.

Rather than try to remove the active regions what we do is simply examine sections of the Sun that will never have active regions present. The active regions only ever form in a band across the center of the Sun, meaning that the regions around the poles are always free of active regions. Thus it can be assumed that a region taken here is representative of the entire Sun without active regions.

To examine this we take two regions measuring 800 by 200 pixels from the top and bottom of the Sun. The locations of these sections can be seen in Figure 5.8, and are highlighted by two red boxes.

The same detection algorithm using a series of concentric thresholds is used as earlier but once the network is detected the quiet areas shown above are simply cut out. A new value is then calculated for the covering percentage of the network within these smaller regions, with the same multiplicative correction applied that was used earlier on the full disc images. We then plot this over the same time period as we did earlier to see how the quiet Sun network varies. What we find is shown in Figure 5.11. While there are still monthly fluctuations present they are now less pronounced than they were for the full disc images, their peaks now several percent lower. Due to this it would appear that the covering fraction of the quiet Sun network does vary slightly on short monthly scales but is overall more consistent than the whole, active, Sun.

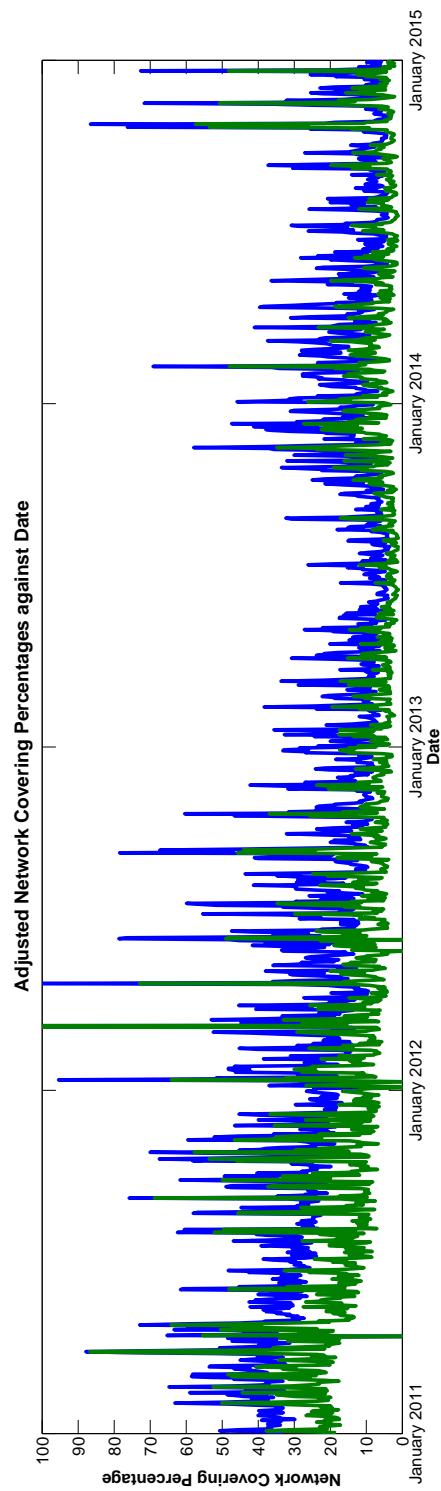


**Figure 5.11:** The covering percentage of the network within the two active region free areas of the Sun from January 2011 to January 2015.

# Chapter 6

## Discussion and Conclusions

### 6.1 Accomplishment of the Initial Aim

The initial aim of this thesis work was to develop an automated method of accurately measuring both the absolute value of the solar UV network covering fraction and its behaviour and correlation with other measures of solar variability.

This was to be done through the development of an automated algorithm to detect the network and thus quantify its covering percentage.

Chapter 4 describes this process and here we demonstrated a certain level of success in our primary aim. Through the use of a series of concentric thresholds we were able to estimate the covering fraction of the solar UV network on three test images. We found that the covering percentages were, for a quiet, mid activity and active Sun; 32.29%, 35.59% and 44.73% respectively. We cannot however confidently state that these are the correct *absolute* values. They more correctly represent the relative covering of the UV network. Attempts were made to justify these covering fraction values in terms of the ‘baseline’ provided by a human observer but it remains the case that these are still somewhat subjective.

In Chapter 5 we explored the behaviour of the UV network and its correlation with other methods of solar variability.

We were able to effectively use the detection algorithm developed in Chapter 4 on large data SDO sets to observe the temporal behaviour of the network. We discovered that there was a long term variability in the covering percentage of the network with it

falling significantly and then slightly rising over the 4 years analysed. Further, a clear monthly variation perhaps related to the rotation of the Sun was present.

Comparing our detected network to the F10.7 radio flux and finding a strong correlation on both long and short timescales helped to indicate the effectiveness of the algorithm for network behaviour monitoring.

We did not manage to remove the active regions from our detection algorithm to fully investigate the behaviour of the quiet Sun network compared to the active. We were however, through the use of two ‘always-quiet’ sections of the solar images, able to successfully demonstrate that there is less variation in the quiet Sun network when compared to the active Sun.

We were not able to demonstrate full automation as corrections to the covering percentage were required. Though this is partly the fault of the data and not wholly down to our algorithm and it is thought full automation could be demonstrated in the future.

## 6.2 Problems Encountered

The first problem faced in this thesis work was the initial presentation of the data. It was inevitable that a large part of this work would rely on the visualisation of the data and a human observer been able to easily identify features. The original data range of the images made this difficult though within Chapter 2 we were able to account for this. Also in Chapter 2 we dealt with the *size* of the images. Using such high resolution data was always going to be necessary for this work but was also not without problems, namely the acquisition, storage and most importantly, the use of this data. A strict time constraint for the work was in place and so it was not possible to test our algorithms on many images. This we accounted for by carefully choosing three test images to represent all the properties needed to develop our algorithms.

The lack of flatfielding first mentioned in Chapter 2 presented issues in our later work. The detection algorithm was affected by this lack of flatfielding but a solution was found. The solution took the form of a retroactive correction applied to the calculated network covering percentages.

Such a correction should not diminish our results too much as though it was slightly ad hoc it was well justified.

The most prevalent problem encountered throughout the entirety of this work was the definition of the network itself. It is known that the network should be brighter than the surrounding material and should form a web-like structure. However, what this looks like on a pixel scale is not quite so easily defined. At this level it is all but impossible to definitively draw the boundaries of the network and as such there is no avoiding a certain level of subjectivity.

### 6.3 Future Work and Improvements

As detailed above, many of the issues present are down to the nature of the network itself. As such, until more is known about the nature of said network the improvements that can be made to this detection method are a little limited. A more thorough knowledge of the causes of the photospheric network would hopefully lead to a better understanding of its boundaries and so aid in the future improvement of the algorithms presented here.

Given a less restrictive timescale there are aspects of the work presented that could be improved upon. The most obvious of these is in the cadence at which we sampled images when we observed the networks behaviour. With more time to analyse the data, and more space to store it, more comprehensive measurements of the network's covering percentage over time could be gained. Further, we could improve on the subjectivity of the detection algorithm slightly given more time, and volunteers. Where we took small sections of the image and marked some of the pixels that we determined to be network we could instead mark *all* the pixels we felt were network. This could be done by many people also giving a more accurate representation of the network to measure the detection algorithms against.

It would also be desirable to apply the morphological dilation detection algorithm to the full four years of data. Here there was only time to fully explore the most promising method but comparisons of two methods that gave quite similar results could offer useful insights.

It is hoped that in the future such an algorithm as presented here could continue to be used on recent SDO data and even further developed for use on older data. The ability to measure decades worth of the UV network's behaviour as opposed to only four years could potentially aid in the future understanding of its nature.

# Bibliography

- [1] M. Littman, F. Willcox, and F. Espenak, *Totality: Eclipses of the Sun (2nd Edition)*. Oxford University Press, 2000.
- [2] F. R. Stephenson, “Historical evidence concerning the sun: Interpretation of sunspot records during the telescopic and pretelescopic eras,” *Philosophical Transactions of the Royal Society of London A: Mathematical, Physical and Engineering Sciences*, vol. 330, no. 1615, pp. 499–512, 1990.
- [3] Office of the Federal Coordinator for Meteorology, *National Space Weather Program Implementation Plan (2nd Edition)*. 2000.
- [4] F. Jansen and R. Pirjola, “Space weather research elucidates risks to technological infrastructure,” *Eos, Transactions American Geophysical Union*, vol. 85, no. 25, pp. 241–246, 2004.
- [5] G. Kopp and J. L. Lean, “A new, lower value of total solar irradiance: Evidence and climate significance,” *Geophysics Research Letters*, vol. 38, p. 1706, Jan. 2011.
- [6] B. Carroll and D. Ostlie, *An Introduction to Modern Astrophysics (Second Edition)*. Pearson, 2007.
- [7] M. Asplund, N. Grevesse, A. J. Sauval, and P. Scott, “The Chemical Composition of the Sun,” *Annual Review of Astronomy and Astrophysics*, vol. 47, pp. 481–522, Sept. 2009.
- [8] J. H. Piddington, “On the origin and structure of stellar magnetic fields,” *Astrophysics and Space Science*, vol. 90, pp. 217–230, Feb. 1983.

- [9] T. Roudier and R. Muller, “Structure of the solar granulation,” *Solar Physics*, vol. 107, no. 1, pp. 11–26, 1986.
- [10] J. Klimchuk, “On solving the coronal heating problem,” *Solar Physics*, vol. 234, no. 1, pp. 41–77, 2006.
- [11] H. Ito, S. Tsuneta, D. Shiota, M. Tokumaru, and K. Fujiki, “Is the Polar Region Different from the Quiet Region of the Sun?,” *Astrophysical Journal*, vol. 719, pp. 131–142, Aug. 2010.
- [12] “Sdo - data.” <http://sdo.gsfc.nasa.gov/data/>. Accessed: 20/10/2015.
- [13] A. Hanslmeier, *The sun and space weather*. Springer, 2010.
- [14] P. Foukal, C. Fröhlich, H. Spruit, and T. Wigley, “Variations in solar luminosity and their effect on the earth’s climate,” *Nature*, vol. 443, no. 7108, pp. 161–166, 2006.
- [15] “Sdo - mission.” <http://sdo.gsfc.nasa.gov/mission/>. Accessed: 5/10/14.
- [16] P. Chamberlin, W. Pesnell, and B. Thompson, *The Solar Dynamics Observatory*. SpringerLink : Bücher, Springer New York, 2012.
- [17] S. B. Howell, *Handbook of CCD astronomy*, vol. 5. Cambridge University Press, 2006.
- [18] J. R. Lemen, A. M. Title, D. J. Akin, P. F. Boerner, C. Chou, J. F. Drake, D. W. Duncan, C. G. Edwards, F. M. Friedlaender, G. F. Heyman, N. E. Hurlburt, N. L. Katz, G. D. Kushner, M. Levay, R. W. Lindgren, D. P. Mathur, E. L. McFeaters, S. Mitchell, R. A. Rehse, C. J. Schrijver, L. A. Springer, R. A. Stern, T. D. Tarbell, J.-P. Wuelser, C. J. Wolfson, C. Yanari, J. A. Bookbinder, P. N. Cheimets, D. Caldwell, E. E. Deluca, R. Gates, L. Golub, S. Park, W. A. Podgorski, R. I. Bush, P. H. Scherrer, M. A. Gummin, P. Smith, G. Aufer, P. Jerram, P. Pool, R. Soufli, D. L. Windt, S. Beardsley, M. Clapp, J. Lang, and N. Waltham, “The Atmospheric Imaging Assembly (AIA) on the Solar Dynamics Observatory (SDO),” *Solar Physics*, vol. 275, pp. 17–40, Jan. 2012.

- [19] J. R. Kuhn, H. Lin, and D. Lorz, “Gain calibrating nonuniform image-array data using only the image data,” *Publications of the ASP*, vol. 103, pp. 1097–1108, Oct. 1991.
- [20] C. Denker, A. Johannesson, W. Marquette, P. R. Goode, H. Wang, and H. Zirin, “Synoptic H $\alpha$  Full-Disk Observations of the Sun from BigBear Solar Observatory - I. Instrumentation, Image Processing, Data Products, and First Results,” *Solar Physics*, vol. 184, pp. 87–102, Jan. 1999.
- [21] J. Singh, R. Belur, S. Raju, K. Pichaimani, M. Priyal, T. Gopalan Priya, and A. Kotikalapudi, “Determination of the chromospheric quiet network element area index and its variation between 2008 and 2011” (RAA, Vol. 12, p.201 [2012]),” *Research in Astronomy and Astrophysics*, vol. 12, p. 472, Apr. 2012.
- [22] S. Chib and E. Greenberg, “Understanding the metropolis-hastings algorithm,” *The american statistician*, vol. 49, no. 4, pp. 327–335, 1995.
- [23] M. Richey, “The evolution of markov chain monte carlo methods,” *The American Mathematical Monthly*, vol. 117, no. 5, pp. 383–413, 2010.
- [24] J. S. Walker, *Fast fourier transforms*, vol. 24. CRC press, 1996.
- [25] J. C. Russ and R. P. Woods, “The image processing handbook,” *Journal of Computer Assisted Tomography*, vol. 19, no. 6, pp. 979–981, 1995.
- [26] R. Gonzalez and R. Woods, *Digital Image Processing*. Prentice Hall, 2001.
- [27] E. R. Dougherty, R. A. Lotufo, and T. I. S. for Optical Engineering SPIE, *Handson morphological image processing*, vol. 71. SPIE press Bellingham, 2003.
- [28] R. M. Haralick, S. R. Sternberg, and X. Zhuang, “Image analysis using mathematical morphology,” *Pattern Analysis and Machine Intelligence, IEEE Transactions on*, no. 4, pp. 532–550, 1987.
- [29] L. Vincent, “Morphological area openings and closings for grey-scale images,” in *Shape in Picture*, pp. 197–208, Springer, 1994.

- [30] C. Mora, A. Kwan, and H. Chan, "Particle size distribution analysis of coarse aggregate using digital image processing," *Cement and Concrete Research*, vol. 28, no. 6, pp. 921–932, 1998.
- [31] J. O. Stenflo, "Time invariance of the sun's rotation rate," *Astronomy and Astrophysics*, vol. 233, pp. 220–228, July 1990.
- [32] S. Schonfeld, S. White, C. Henney, N. Arge, and J. McAteer, "The Sources of  $F_{10.7}$  Emission," in *AAS/AGU Triennial Earth-Sun Summit*, vol. 1 of *AAS/AGU Triennial Earth-Sun Summit*, p. 31105, Apr. 2015.
- [33] K. Tapping, "The 10.7 cm solar radio flux (f10.7)," *Space Weather*, vol. 11, no. 7, pp. 394–406, 2013.
- [34] L. Svalgaard, "Reconstruction of Solar EUV flux 1781-2015," *IAU General Assembly*, vol. 22, p. 53999, Aug. 2015.
- [35] S. K. Solanki, N. A. Krivova, and J. D. Haigh, "Solar Irradiance Variability and Climate," *Annual Review of Astronomy and Astrophysics*, vol. 51, pp. 311–351, Aug. 2013.
- [36] "Leif svalgaard - research." <http://www.leif.org/research/>. Accessed: 15/03/15.
- [37] J. Elsner and A. Tsonis, *Singular Spectrum Analysis: A New Tool in Time Series Analysis*. Springer US, 2013.
- [38] N. Golyandina and K. Usevich, "2d-extension of singular spectrum analysis: algorithm and elements of theory," *Matrix Methods: Theory, Algorithms, Applications*. Singapore: World Scientific Publishing, pp. 450–474, 2010.